The dynamics of chiral domain walls in multilayer films with perpendicular magnetic anisotropy

Dayane de Souza Chaves

Communauté
UNIVERSITÉ Grenoble Alpes

THÈSE

Pour obtenir le grade de

DOCTEUR DE LA COMMUNAUTE UNIVERSITE GRENOBLE ALPES

Spécialité : **Physique de la Matière Condensée et du Rayonnement**

Arrêté ministériel : 25 mai 2016

Présentée par

Dayane DE SOUZA CHAVES

Thèse dirigée par **Stefania PIZZINI** et
codirigée par **Jan VOGEL**
préparée au sein d'**Institut Néel/CNRS**
dans **l'École Doctorale de Physique de Grenoble**

Dynamique de parois chirales dans les multicouches magnétiques avec anisotropie perpendiculaire

The dynamics of chiral domain walls in multilayer films with perpendicular magnetic anisotropy

Thèse soutenue publiquement le **25 juin 2018**,
devant le jury composé de :

Dr. Vincent, Cros, Directeur de Recherche,
Unité Mixte de Physique CNRS/ Thales, Rapporteur

Dr. Julio Camarero, Professeur,
Universidad Autónoma de Madrid, Rapporteur

Dr. Hélène Béa, Maître de Conférences,
Spintec, Examinateur

Dr. Jean-Philippe Attané, Maître de Conférences,
Spintec, Examinateur

Dr. Vitória Maria Tupinambá de Souza Barthem, Professeur,
Universidade Federal do Rio de Janeiro, Président du jury

To my husband Vinícius that is my love

my father Ribamar that is my inspiration

and my mother Socorro that is my safe harbor.

Acknowledgement

I am very grateful for everything that involves this work, but first I would like to thank CNPq (Conselho Nacional de Desenvolvimento Científico e Tecnológico) for the opportunity to study abroad by to the financial support granted by Ciência Sem Fronteira. I feel very honored to have this privilege which brought me many professional and personal gains.

Then, I would like to say thank Vinícius, you were essential in this achievement, supporting me in my decisions and believing in me. Thank you so much for helping me always to try a better human being. You make my life happier. I love you.

I like to show the sincere gratitude to my supervisor Stefania Pizzini for the opportunity to perform this work, by the guidance, by the numerous scientific discussions, and by her availability and I would like to extend my gratitude to Jan Vogel that who besides being my co-supervisor and always helped a lot in the scientific discussions, helped me see life differently and was always a good company in our trips to the synchrotron.

I would like to thank Olivier Boulle for the opportunity to work together and to know almost all PEEMs in Europe. Thank you for trusting in my work and for the company always enjoyable during all beamtimes.

I could not leave out of my thanks Philipe David and Eric Mossang who from the beginning of my Ph.D. have helped me so much, from training and scientific discussions to advice that was very important for me always to stay motivated and focused on research.

I would also like to thank Marlio Bonfim, who very kindly taught me to solve problems and to manufacture an essential part of this work.

I would like to say thank you: Nora Dempsey, Thibaut Devillers, Gabriel Gomez-Eslava, Doan Nguyen Ba for the good times that I have been with you and for all that I could learn from you.

This lab brought me many gains, and one of them was André Dias, I would like to thank you for so much laughter, conversation, your friendship, you left everything more fun. Another gain was Anja Baken, with all my communication problems and you with all your patience, all our comings and goings to the ice cream shop were very special to me. Thanks.

I would like the say thanks to the Micro et NanoMagnétisme - MNM group, to the Nanofab group for all contributions to this work.

I also wish to express my gratitude to the officials and other staff members of CNRS who rendered their help during the period of my work. I am grateful to all my colleagues and friends, who were more than a family to me during my stay at the team. Without your help, this work would not be possible.

I would like thanks to the reporters Vincent Cros and Julio Camarero, the members of the jury Hélène Béa, Jean-Philippe Attané and Vitória Maria T. de Souza Barthem who accepted the invitation to evaluate my work and scheduled their time for my Ph.D. defense.

I would like to thank Julio Criginski, Yves Petroff, Simone Betim, and Janaina Oliveira. Also, say that everything you have done and has done for me I will never forget.

I would like to thank the little family that I built here, Estephanie, Henrique, Aline, Debora, and Lucas. Without you, the walk would be challenging and cumbersome.

I would like to say thank Clara and Ana Lucia for friendship for so many years, and yet so far you are always present at significant times. Love you.

And of course my family, my father Ribamar, my mother Socorro, my brother Junior, my sister Hellen, my niece Helena and nephew Dudu. You have always been the reason why I always try to go further. Thank you for merely existing you. I love you so much.

Thank you all, this time here was precious in my life, and I will remember that forever.

Contents

1 Introduction

Men have been increasingly demanding, and when it comes to technology, this requirement could not be different. In recent decades, the use and consequently the advancement of technology has progressed as never seen before. The search for high-performance has gained space, and what before seemed only movie scene, today is part of life with the different tools, that help us to access different information such as online libraries of songs, movies, Internet search engines, books that were unavailable just a few years ago.

With all this technology, the development of a quick access of all this information with a high-speed communication, and data processing as well as new ways to store such digital data becomes more and more necessary.

For more than half a century the magnetic hard disk drives (HDDs) have been the prime repository of the digital data offering their particular advantages. In HDDs, digital data are stored as the magnetization direction of the tiny nanometer sized magnetic domains. Each magnetic domain i.e. each region on the magnetic thin film with specific magnetization direction, defines a bit. In these drives, the magnetization direction i.e. the 0 or 1, are read and written relying on mechanical movement, which make the HDDs slow and the energy consumption high. These drawbacks have encouraged the search for another technology.

That is why appeared the solid-state memory, a device that reads and writes data with great speed, using the electronic state of transistors and capacitors to store data bits. Enabling high-performance, such static and dynamic random-access memory (SRAM and DRAM, respectively) does not seem however an ideal solution for digital storage, as the data are lost when the computer powers down or crashes also needs refreshment.

Another alternative that retains data when the power is switched off, is the flash memory. In this device, we have a compensation between cost and performance. Flash memory is low cost, however, is slow and unreliable in comparison with other memory chips.

From this evolution of devices, groups of researchers are looking for solutions for a data storage with high data density, fast, cheap, reliable and nonvolatile.

Ten years ago, an alternative memory called racetrack memory had been proposed by Parkin *et al.* [Par+08] at IBM offering the potential for this desire: a device with the high performance of Magnetoresistive random-access memory (MRAMs) but the low cost of HDDs without any moving parts, so it will be more reliable, will use less energy and will be much faster.

A racetrack memory (RM) uses magnetic domains in nanowires to store information as shown in Figure 1.1. Two sequential opposite magnetic domains have a boundary called magnetic domain wall (DW). The bit length is defined as the spacing between two DWs, which is controlled by pinning sites created along the wire.

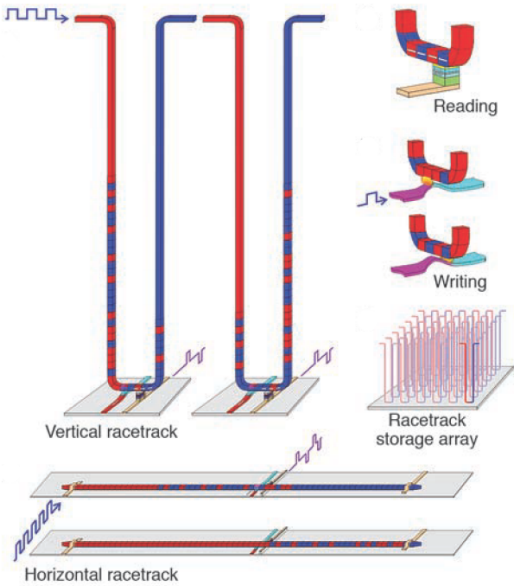

Fig. 1.1: Sketch of a racetrack memory by Parkin *et al.* [Par+08].

Fundamentally, the RM works by shift registers in which bits are moved by nanosecond current pulses and individual reading and writing elements are integrated within each racetrack (Fig. 1.1).

This principle was first applied to permalloy nanowires, which is magnetically soft (Racetrack memory 1.0). In this case, the DWs can reach speeds around 100m/s for current densities in the region of $10^8 A/cm^2$. However, the DW width in the soft material is influenced by the shape anisotropy, so domain walls are rather large. Also, the DWs are very flexible and can expand their equilibrium size under applied current, so it is not ideal to use the soft magnetic materials.

In Racetrack memory 2.0 [PY15] much narrower and more robust DWs were injected in materials (in this case, Co/Ni) with significant magnetic anisotropy oriented perpendicular to the plane of the nanowire.

In such devices, the DWs move much faster than those found in permalloy. Very large DW velocities ($\sim$ 400m/s) were first observed in ultrathin layers of cobalt deposited on a platinum layer and covered by an oxide by Miron *et al.* [Mir+11] .

There are many mechanisms that contributed to this result which include i) the perpendicular magnetic anisotropy (PMA) resulting from the deposition of the magnetic layer on a heavy metal with large spin-orbit coupling; ii) the presence of interfacial Dzyaloshinskii-Moriya interaction (DMI) that is an exchange interaction that favors chiral Néel walls; iii) the spin current of conduction electrons through the spin Hall effect, which generates a transverse spin current in the Pt, that is absorbed by Co and exerts a torque on the DW magnetization.

These phenomena together allow the DWs to move much faster. Speeds around 350m/s for current densities in the region of 10^8A/cm^2 have been observed in Pt/Co/Ni/Ta layers also by [Ryu+13].

The key concept and one of the most challenging aspects of racetracks is the controlled and reproducible movement of DWs along the nanowires by means of current pulses.

The DW motion may be controlled by tuning some parameters such as the thickness of the heavy metal layers and the composition of the magnetic layer, since the DMI and spin Hall effect depend on these parameters.

The aim of this thesis is: i) to better understand the dynamics of domain walls under field and current in systems with PMA and DMI; ii) to investigate and propose suitable systems that may be used in racetrack memories.

In order to help the comprehension, this thesis was divided in seven chapters. The specific contents of the chapters are:

Chapter 2 gives a short overview of the main theoretical concepts necessary to follow the arguments discussed in this thesis. The chapter is divided in four sections. The first introduces systems with perpendicular magnetic anisotropy (PMA), then discusses the DW internal structure and field and current driven dynamics of DWs in thin films with PMA and with Dzyaloshinskii-Moriya interaction (DMI).

Chapter 3 concerns the experimental techniques that we used to fabricate the samples and characterize them. The chapter is divided in three sections. First we describe the methods with which the samples were prepared, then the structural characterization and finally the techniques used for the magnetic characterizations.

Chapter 4 reports the results and discussion about the DW velocities in Pt/Co/Gd and Pt/Co/GdOx trilayers with DMI. We will compare the DW speed in a symmetric and asymmetric stacks with PMA at the Walker field, we will address the DMI strength in asymmetric stacks with the measurements of the DW speed driven by an out-of-plane field in the presence of an in-plane field. Finally we introduce a new method to address the DMI strength based on the measurement of the DW speed after the Walker field.

Chapter 5 is dedicated to the study of the dependence of DMI on the oxygen coverage in Pt/Co/MOx (M= Al, Gd) trilayers. We will access the values the DMI strength, and these will be compared for different degrees of oxidation of the Co/MOx interface. Finally we will study how the DMI values can be related to the magnetic anisotropy energy.

Chapter 6 reports the preliminary study of the domain wall motion in Pt/GdCo/Ta thin films which is grown in such a way that we have a composition gradient along the sample with a compensation composition at room temperature. Field and current-driven dynamics is studied for various alloy compositions. We demonstrate that spin-orbit torque is very efficient in samples with reduced magnetization.

Chapter 7 Finally, the main conclusions, the most relevant results and suggestions for future work are summarized.

2 Background

In this chapter we will introduce the relevant concepts that are present in this thesis. They are a brief overview of significant concepts of the recent literature that provide theoretical foundations for the experimental results obtained in this work. First, we talk about the systems with perpendicular magnetic anisotropy (PMA) in section 2.1. The behavior of domain walls in systems with PMA is described in section 2.2. In section 2.3.1 we will discuss non-centrosymmetric magnetic multilayers that present the interfacial Dzyaloshinskii-Moriya interaction. Finally, we will discuss the dynamics under spin polarized current in section 2.4.

2.1 Systems with Perpendicular Magnetic Anisotropy

The study of magnetic films with perpendicular magnetic anisotropy (PMA) is an important topic today because of their applications in ultra-high density storage devices and in spintronics magnetic random access memories [Par+99; Par+03]. In this section we will present the main concepts about the PMA and how to determine experimentally the PMA in thin films.

2.1.1 Introduction to perpendicular magnetic anisotropy (PMA)

In magnetic materials the magnetization can lie at in some preferred directions with respect to the crystallographic axes or/and to the external shape of the sample. This property is called magnetic anisotropy.

The energy involved in rotating the magnetization from the direction of low energy (easy-axis) to one of larger energy (hard axis) is called anisotropy energy that is very small compared to the total magnetic energy of the system. This is why it has been difficult to calculate. It derives from relativistic corrections of the system hamiltonian: either the dipole-dipole interaction or the spin-orbit coupling (SOC).

The anisotropy term leading to the dependence of energy on the crystallographic axes is called magnetocrystalline anisotropy (MCA). The anisotropy that leads to the magnetization alignment parallel to the plane in a thin plate is called shape anisotropy. The first is an intrinsic contribution depending on the magnetic material; the second is extrinsic and depends on the geometry of the sample. The MCA arises essentially from spin-orbit coupling while the shape anisotropy arises from the dipole-dipole interaction. In a film the magnetic anisotropy energy has a volume component K_v and an interface component K_s expressed as:

$$K_{eff} = K_v + \frac{2K_s}{t} \tag{2.1}$$

where the factor 2 accounts for the two interfaces and $K_v = K_{Vdip} + K_{Vmc}$, where K_{Vmc} in thin film systems can be neglected.

The interface component comes from the fact that, as pointed out first by Néel , the atoms located near the interface have a different environment as compared to bulk atoms.

In general, in thin films the main contribution to the volume anisotropy K_v is the shape contribution, of dipolar origin. This favors an in-plane magnetization (minimization of magnetic charges). This is simply related to the saturation magnetization by $K(\text{shape}) = -\mu_0 M_s^2/2$. The MCA contribution to the volume anisotropy is much smaller and can be neglected.

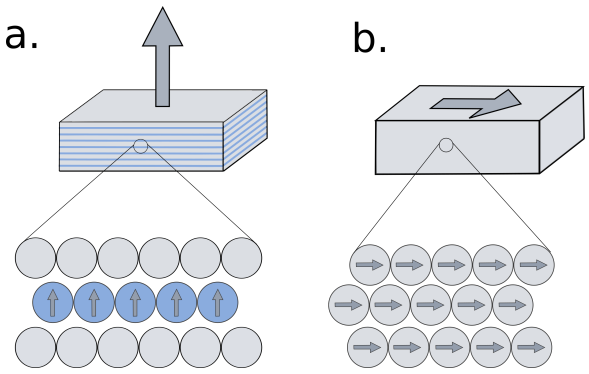

Fig. 2.1: Illustration of magnetic anisotropies in two often found cases. **a.** In multilayer systems consisting of alternating magnetic and non-magnetic-layers, the magnetization may be out-of-plane. **b.** In magnetic films with the thickness exceeding about 2nm the easy magnetization direction is typically found to be in-plane.(Figure adapted from [Stö99]).

In general, for thick films, the shape anisotropy dominates and the magnetization lies in the plane of the layer. For thin films, the interface contribution increases and can lead to perpendicular magnetic anisotropy (PMA). The PMA is of magnetocrystalline

origin, and its origin is the spin-orbit coupling H_{so}. This is a relativistic correction to the total energy of the electrons. It can be interpreted as the coupling between the spin of the electron and the magnetic field created by its orbital moment around the nucleus. As the orbital motion is itself coupled to the lattice via the crystal field (the electric potential of the ions) this term provides a contribution to the MCA.

The spin-orbit coupling can be expressed as $H_{so} = \xi \mathbf{l.s}$ where ξ is the spin-orbit constant and **l** and **s** are the orbital and spin moment of the electrons (3d, 4d or 5d in transition metals).

Using a perturbation theory P. Bruno [Bru93] showed that the interfacial anisotropy energy caused by the SOC is directly linked to the anisotropy of the orbital moment:

$$\Delta E_{so} = -\frac{G}{H}\frac{\xi}{4\mu_B}(m_{orb^{\perp}} - m_{orb^{\parallel}}) \tag{2.2}$$

where the factor G/H depends on the details of the band structure.

This was proved experimentally by Weller *et al.* [Wel+95] for a Au/Co/Au trilayer sample with PMA, using X-ray magnetic circular dichroism (XMCD) measurements.

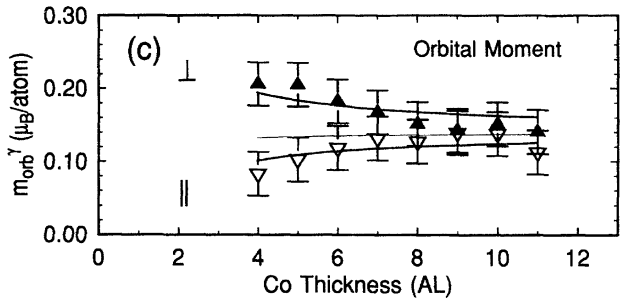

Fig. 2.2: Orbital moment $m_{orb^{\perp}}$ and $m_{orb^{\parallel}}$ as a function of Co thickness in Au/Co/Au trilayers. Image from [Wel+95].

Note that in 3d transition ions the electric field of the neighboring atoms (crystal field) breaks the spherical symmetry of the free atom. Because of the crystal field the energy levels (xy, yx, xz, $x^2 - y^2$ or $3z^2 - r^2$) become combinations of opposite orbital moments (m_l and $-m_l$), so that the total orbital moment quenched. In the absence of SOC the magnetic moment of 3d ions would be a pure spin moment. The effect of the SOC is to split the energy levels, and to partially remove the quenching of the orbital moment. In the case of 3d metals the role of the crystal field is played by the band dispersion of the electronic levels [Bru93].

The anisotropy of the orbital moment can be visualized in terms of the anisotropy of the bonding environment. Let's take the case of an atom bonded to 4 atoms with a negative charge, in a planar geometry. The orbiting electron will experience a Coulomb repulsion by the neighbor ions and the electron will form a standing wave by superposition of two oppositely traveling waves with opposite orbital moment (fig.2.3). Said differently, the orbital motion will be broken up through the formation of molecular orbitals. The corresponding orbital moment, perpendicular to the electron orbit will be quenched. The orbital moment perpendicular to the bonding plane will be less disturbed owing to the lack of neighboring ions and the corresponding in-plane orbital moment will remain largely unquenched. This picture relates the anisotropy of the orbital moment to the anisotropy of the bonding environment. This simple model predicts that for a free monolayer the orbital moment will be larger in the plane than in the plane perpendicular to it. However for the case of a stronger bond in the out-of-plane direction e.g. for a multilayer, the orbital moment would be larger in the perpendicular direction favoring perpendicular magnetic anisotropy.

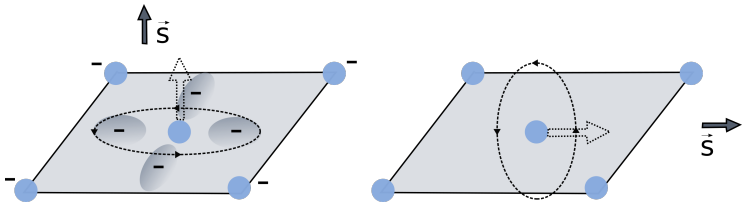

Fig. 2.3: Anisotropy orbital moment in a thin layer. For a free monolayer the orbital momentum (or moment) is predicted to be larger in the bonding plane than perpendicular to it, and for the case of stronger out-of-plane bonding, e.g. for a multilayer, the orbital moment would be larger in the out-of- plane direction. Image adapted from [Stö99].

J. Stohr [Stö99] following the work of Bruno [Bru93] showed that this simple model is also valid in a metal film. In this case, Bruno showed that the spin-orbit energy is related to $\xi 2/W$ where W is the electronic bandwidth. In the case of a free monolayer, $W^{\parallel}_{\parallel}$ will be larger than $W^{\perp}_{\perp}$ so that $m^{\parallel}_{orb} > m^{\perp}_{orb}$. Let us take instead the case of a 3d transition metal, Co, in contact with a 5d metal, Pt. The strength of the Co-Pt bond (through 3d – 5d hybridization) in the perpendicular direction is much stronger (about 1.6 times more) than the Co-Co bond in the plane. This means that the out-of-plane bandwidth will be larger than the in-plane bandwidth. Within a certain approximation concerning the band filling, it can be shown that this gives rise to a larger orbital moment in the perpendicular direction and explains why multilayers comprising Pt/Co interfaces can present PMA.

Trilayers comprising a Pt/Co interface are studied in this thesis.

2.1.2 Experimental determination of perpendicular magnetic anisotropy

The concept of the effective anisotropy energy K_{eff} is the energy required to align the magnetization along the hard magnetization axis [Joh+96]. It can be calculated by the difference of the area of the hysteresis loop measured along the hard axis and easy axis directions. In this way, the expression for K_{eff} can be:

$$K_{eff} = \int_{hard_{axis}} M.dH - \int_{easy_{axis}} M.dH \tag{2.3}$$

Usually K_{eff} assumes positive values for out-of-plane magnetization and can be obtained using $K_{eff} = \mu_0 H_a M_s/2$ determined from VSM/SQUID measurements, where M_s is the saturation magnetization and H_a the in-plane saturation field.

In practice the anisotropy field measured along the easy axis is much smaller than that measured along the hard easy, so can be neglected, except near the transition from perpendicular to in-plane magnetization, when occurring in cases with very narrow thickness range (Fig. 2.4).

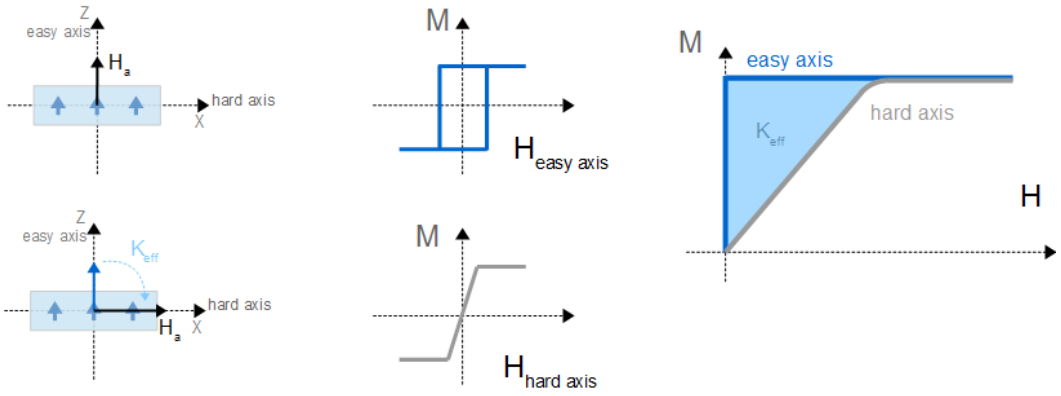

Fig. 2.4: Magnetization measurements at easy and hard axis, showing K_{eff} as the difference between areas of the curves of the magnetization measurements in case of a sample with out of plane magnetization. Image adapted from [Nis11].

Figure 2.5 shows an example for a Co/Pd multilayer. Based an the equation 2.1, the figure shows a plot of $K_{eff}t$ versus t, where t is the thickness of the magnetic layer.

The interfaces contribution, $2K_s$, is obtained from the vertical axis intercept, while the slope of the linear part of this curve gives the effective bulk anisotropy. The effective anisotropy can be:

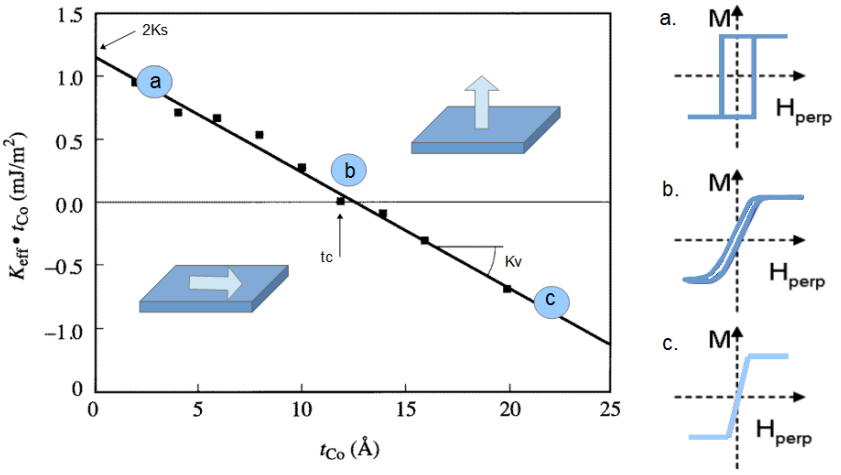

Fig. 2.5: Magnetic anisotropic energy times Co layer thickness *versus* Co layer thickness of Co/Pd multilayer. Image adapted from [DB+91]

a. Positive ($K_{eff} > 0$): The contribution of interface anisotropy $2K_s$ overcomes the contribution of bulk anisotropy $K_u = K_{Vmc} - \mu_0 M_s^2/2$, the strong demagnetizing fields which are created when tilting the magnetization out of the film plane is not sufficient, resulting in a perpendicular magnetized system.

b. Zero ($K_{eff} = 0$): This gives the magnetic thickness, called critical thickness, that marks the transition of the magnetization from out-of the film plane to in-plane.

c. Negative ($K_{eff} < 0$): The bulk anisotropy outweighs the interface contribution and the magnetization becomes in-plane.

2.2 Domain walls in thin films with PMA

Magnetic domains in thin films can display various morphologies. These are determined by different parameters such as the film thickness, the direction of the applied field, the competition of different energies and interactions. In this section we will present the study of the domain structure and the dynamics of the domain walls.

2.2.1 Magnetic domains

With the purpose of explaining why a ferromagnetic material can exist in the demagnetized state Pierre Weiss in 1907 [Wei07] gave the first concepts about magnetic domains, and his theory was later confirmed in 1931 by Bitter with a visualization technique.

In magnetic materials, a magnetic domain is the region where the atomic magnetic moments are oriented approximately in the same direction. The magnetic domains arise from the need to balance the contribution of the different energy terms. The energetic cost is related with the magnetostatic energy, exchange energy and magnetocrystalline anisotropy. When the number of domains increases, the magnetostatic energy is reduced but other energy terms increase.

Two magnetic domains are separated by a region called a domain wall (DW). This region brings an increase in exchange and anisotropy energy.

2.2.2 Domain wall internal structure

The interface which separates regions with constant spontaneous magnetization, is called a domain wall.

The theoretical model proposed by F. Bloch in 1932 [BB32] for bulk systems suggested that the exchange energy would be minimized if the transition from a magnetic domain to the other occurred in a smooth way (Figure 2.7)

The DW has a finite width that results from the competition between the exchange and the anisotropy energies.

The domain walls can be classified as 90° or 180° depending on the axis of magnetization. In this work, we are discussing the domain walls of 180° whose formation occurs between domains having magnetization with opposite direction (Figure 2.6).

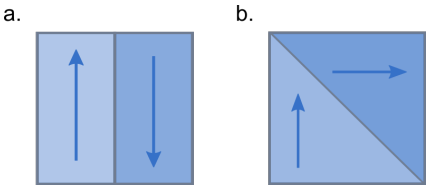

Fig. 2.6: Diagram showing the rotation of magnetic moments through **a.** 180° domain wall **b.** 90° domain wall.

In thin films with perpendicular magnetic anisotropy (PMA) two types of DW can be found, that can be distinguished from one another in the way the atomic magnetic moments turn in the wall. There are:

Bloch and Néel Walls in systems with PMA

In a Bloch wall the rotation of the magnetization vector occurs in the plane parallel to the plane of the domain wall (Fig. 2.7). The magnetization remains in the plane

of the DW and the film plane is ∞. In this case, the contribution associated to the magnetostatic energy vanishes as the magnetic charges are repelled towards the infinity. No magnetic charges are present in the volume or in the DW plane.

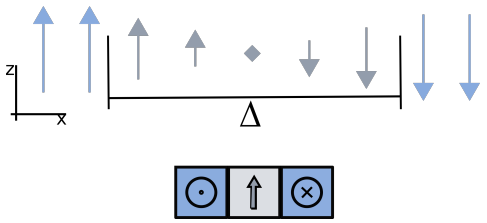

Fig. 2.7: Bloch domain wall, with rotation of the magnetization in the plane parallel to the plane of DW: side view (top) and top view (bottom) with Δ the DW width parameter.

In Néel walls the magnetization rotates in a plane perpendicular to the plane of the DW (Fig. 2.8). In this case, magnetic charges are accumulated in the x direction, so that a magnetostatic energy is associated to this domain wall.

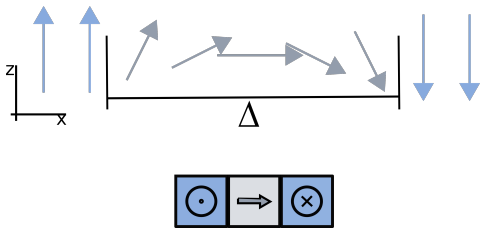

Fig. 2.8: Néel domain wall, with rotation of the magnetization in the plane perpendicular to the plane of DW: side view (top) and top view (bottom) with Δ the DW width parameter.

The Bloch walls are generally the most stable in thin films with perpendicular anisotropy. Up to very recently, they have been assumed to be always present in thin films within PMA.

2.2.3 Defining the domain wall width

To estimate the domain wall width considering the energy associated with the formation of the domain wall, we will use the method described below [Gui09]:

Let's consider two adjacent domains with opposite magnetization direction separated by a DW of 180°. The configuration of the DW results from the equilibrium between the exchange energy and the total anisotropy energy.

The exchange energy of the two adjacent moments of spin $\vec{S_1}$ and $\vec{S_2}$ within the domains is:

$$E_{ex} = -2JS^2 \tag{2.4}$$

When the moments $\vec{S_1}$ and $\vec{S_2}$ are not parallel and are tilted by an angle φ, the energy will be:

$$E_{ex} = -2J\vec{S_1}.\vec{S_2} = -2JS^2\cos\varphi \tag{2.5}$$

for small values of φ, we can write $\cos\varphi = 1 - \varphi^2/2$, then:

$$E_{ex} = -2JS^2 + JS^2\varphi^2 \tag{2.6}$$

The first term is independent of the angle and can therefore be dropped. In the Bloch wall the rotation of 180° happens on the N moments that compounds the wall. The angle of rotation between two adjacent moments is $\varphi = \pi/N$, where N is the number of moments that compounds the wall. This way, the exchange energy existing within the wall given by the second term is:

$$E_{ex} = NJS^2\varphi^2 = \pi^2 JS^2/N \tag{2.7}$$

Since a is a lattice parameter, the energy per unit of area on the Bloch wall can be written as:

$$E_{ex}^{Bl} = JS^2 \cdot \frac{\pi^2}{Na^2} \tag{2.8}$$

With this expression, it is clear that N should be infinite in order to minimize the exchange energy. However the anisotropy energy also has to be taken into account to minimize the DW energy. This contribution leads to a decrease for a finite size of the DW width.

The anisotropy energy per unit volume in the case of uniaxial anisotropy is defined as:

$$E_{a_v} = K_{eff}\sin^2\theta \tag{2.9}$$

with θ defined from the easy magnetization axis and $K > 0$ favoring the alignment of the moments in the domain wall parallel or antiparallel to the out-of-plane direction.

The sum of all the contributions of the N moments to the energy per unit area (Na) of the wall , can be written as:

$$\sum_{i=1}^{N} K\sin^2\theta_i \approx \frac{1}{2}NaK \tag{2.10}$$

rewriting,

$$E_{a_v}^{Bl} = \frac{1}{2}NaK \tag{2.11}$$

The first term maximizes the number of moments inside the DW, increasing the DW width, whereas the second minimizes the number of moments, narrowing the DW. The minimum energy is obtained when we equal the derivative of the energy function with respect to N to zero.

$$\frac{dE^{Bl}}{dN} = 0 = \frac{1}{2}aK - JS^2\frac{\pi^2}{a^2}\cdot\frac{1}{N^2} \tag{2.12}$$

Resulting in,

$$N = \frac{\pi}{a}\sqrt{\frac{2JS^2}{Ka}} \tag{2.13}$$

We define the exchange stiffness as:

$$A = \frac{nJS^2}{a} \tag{2.14}$$

where *n* corresponds to the number of atoms per unit cell that in this case is n = 2. This leads to the following expression for domain wall width $W = Na = \pi\sqrt{A/K}$.

$$\Delta = \sqrt{\frac{A}{K}} \tag{2.15}$$

is defined as the domain wall parameter (Bloch parameter).

This shows that the domain wall width depends on the parameters A and K. It is seen directly that a high value of the exchange stiffness A favors a large width of the domain wall, whereas a large magnitude of anisotropy constant K tends to reduce the width Δ.

2.2.4 Dynamics of domain walls

The field-driven motion of DWs has been studied extensively in thin films [Slo72; HS08]. In the context of the device application, the first proposition for using domain walls was in magnetic memories by motion of bubble domains. Nowadays, we know that DW can be driven to motion with magnetic field or electrical current. In this section will consider the case of field driven DW motion.

Mechanism of domain wall motion in systems with PMA

Consider a Bloch wall with the width parameter as defined in the equation 2.15.

Usually, when studying the dynamics of the DW, we suppose that the applied field is sufficient to overcome the pinning forces due to defects, thus, the velocity v is linearly dependent on the applied field H.

In this situation, the dynamics is guided by two regimes characterized by different mobilities that are defined by m = dv/dH as shown in the Figure 2.9.

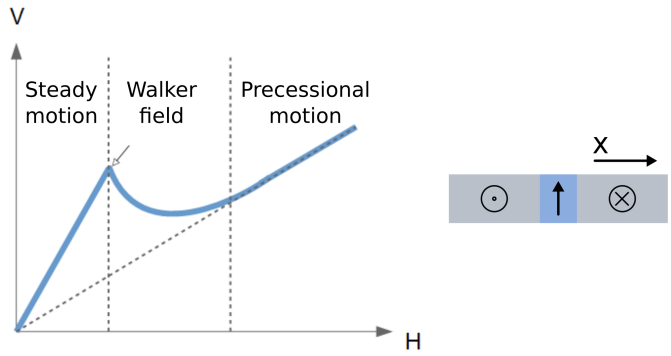

Fig. 2.9: Predicted domain wall velocity versus magnetic field of a Bloch wall showing steady and precessional flow regime in thin films without pinning (1D model).

In the first regime, called steady regime, a torque from the external field H_z tilts the magnetization away from the original position, and the component along the x axis takes non-zero values. This component induces a rising of the magnetostatic field perpendicular to the DW (x – direction) which allows the wall to move with a

constant velocity, which scales linearly with the external field with the mobility given by:

$$m = \frac{\gamma_0 \Delta}{\alpha} \tag{2.16}$$

where γ is the gyromagnetic ratio and α is the Gilbert damping parameter. From the value of the mobility can be obtained the velocity, which is expressed by:

$$v_{st} = \frac{\gamma_0 \Delta}{\alpha} H \tag{2.17}$$

This first regime is called "steady flow" as the DW internal structure is not modified during the motion (Figure 2.9).

As shown in Figure 2.9 the velocity does not increase infinitely, but it reaches a maximum value at some field called the Walker field, defined by [Mou+07]:

$$H_w = \frac{\alpha M_s N}{2} \tag{2.18}$$

Where N is the demagnetizing factor across the wall, given in the simple approximation by $t/(t + \Delta)$, where t is the ferromagnetic layer thickness.

Beyond this field a transient regime is observed, where the velocity may fluctuate or even oscillate, as the spins inside the Bloch wall start precessing and the velocity drops, before reaching a second regime.

Called precessional flow regime, in the second linear regime the mobility is expected to be lower than the first regime, since the structure of the DW changes continuously. The mobility is defined by [Met+07]:

$$m_{pr} = \frac{\gamma_0 \Delta}{(\alpha + \alpha^{-1})} \tag{2.19}$$

The velocity in the precessional regime is then defined as:

$$v_{pr} = \frac{\gamma_0 \Delta}{(\alpha + \alpha^{-1})} H \tag{2.20}$$

In real systems, the presence of the pinning forces slows down the DW motion and the theory predicts three regimes of DW motion, as shown in the Figure 2.10.

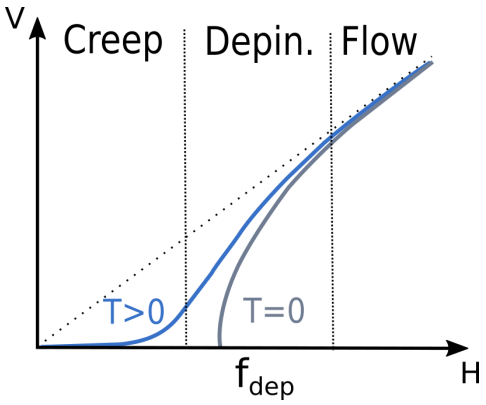

Fig. 2.10: Theoretical velocity-field curves for real systems showing depinning , creep and flow regime.

In real samples defects of different origin are always present. For example, the structural disorder caused by crystallites or steps at the frontiers of flat atomic terraces. These defects can locally change sample parameters such as the exchange stiffness (A), the magnetic anisotropy (K), the thickness of the film or even the roughness, giving rise to potential energy variations within the film.

We call *pinned* a state of the DW for which the local energy is a minimum. Here the DW motion is governed by the competition between the elastic energy and the disorder.

At zero temperature the DWs are pinned up to a field called the depinning field (H_{dep}). Thermally activated fluctuations happen at a finite temperature, thus the DW exhibits a slow motion the so-called creep regime where the DW velocity changes exponentially with the field (Fig 2.10).

Figure 2.10 shows at zero temperature the DWs do not move up to H_{dep}. Above the depinning field H_{dep} the DWs are able to overcome all local energy barriers, going to the next regime.

The last regime (Fig. 2.10), is the flow regime, where the velocity is proportional to the applied field and approaches that expected for an interface moving in systems without disorder, as described before.

2.3 Systems with Dzyaloshinskii-Moriya interaction (DMI)

The dynamics of DWs in multilayer films with PMA is much studied nowadays. In non-centrosymmetric multilayers with ultrathin magnetic films, DWs can acquire a Néel internal structure with a fixed chirality, stabilized by the interfacial Dzyaloshinskii-Moriya interaction (DMI). This interaction modifies the internal structure of the DW and its dynamics. In this section we will discuss the type of system where DMI can be found, its origin and the consequences that the contribution of the DMI can bring to DW structures and dynamics.

2.3.1 Non-centrosymmetric systems

In the last few years, studies of thin magnetic films have known big advances, due to the discovery of new effects that occur at the interface between a heavy metal (HM) and a ferromagnet (FM). These systems can acquire interesting properties such as a defined chirality of the magnetic texture imposed by the Dzyaloshinskii-Moriya interaction (DMI), if grown in a non-centrosymmetric stack.

Origin of DMI

The chirality is a fascinating property in nature. Pasteur in 1848 [Mis99] related chirality to the molecular dissymmetry which may arise from a tetrahedral or a helical arrangement of the atoms. In physics, chiral textures usually appear as the result of symmetry breaking, either spontaneously, as in the case of macroscopic quantum system [VK12], or it can be stabilized by a chiral interaction like it is the case of magnetism.

Chiral magnetic structures are playing an essential role in modern physics, since the discovery of magnetic skyrmions [Fer+13; Hei+11; Bou+16], and fast-moving chiral DWs [Thi+12].

Dzyaloshinskii in 1960 [Dzy60] pointed out a model to understand the formation of magnetic states with a certain chirality while describing weak ferromagnetism. Using symmetry arguments, he introduced an anti-symmetric term in the exchange interaction. Moriya, contributed to this work when he found the mechanism that connected this term with spin-orbit coupling [Mor60] from which the name of Dzyaloshinskii-Moriya interaction (DMI).

Spin chiral textures originating from DMI [Mor60; Dzy57] can occur only in structures that lack or break inversion symmetry in non symmetric crystal or at interfaces.

The energy contribution from the DMI can be written as:

$$E_{DMI} = \mathbf{D_{1,2}} \cdot (\mathbf{S_1} \times \mathbf{S_2}) \tag{2.21}$$

where in this expression ($\mathbf{S_1}$, $\mathbf{S_2}$) are the magnetic spin moments on neighboring atomic sites i and j and $\mathbf{D_{1,2}}$ is a vector parameter of the interatomic Dzyaloshinskii-Moriya interaction that depends on the material properties.

While the Heisenberg exchange interaction (Eq. 2.4) favors the parallel or anti-parallel alignment of neighboring spins, in its turn the DMI expressed by equation 2.21 favors the orthogonal orientation of spins. The competition between the two terms gives rise to non collinear textures with a fixed sense of rotation of magnetic moments (chirality) defined by the direction of the DMI vector $\vec{D}$.

For ultrathin magnetic films, which are the main focus here, Levy and Fert [FL80] proposed a mechanism called 3-site indirect exchange which allows obtaining the direction of the vector $\vec{D}$. At an interface between a ferromagnetic thin layer with PMA and a metallic layer with large SOC, the mechanism generated between two atomic spins $\mathbf{S_1}$ and $\mathbf{S_2}$ with a neighboring atom having a large SOC gives rise to a DMI vector $\vec{D}_{12}$ perpendicular to the plane of the triangle formed by two neighboring $\mathbf{S_1}$ and $\mathbf{S_2}$ and the atom with large SOC (Fig. 2.11). $\vec{D}_{12}$ is therefore parallel to the plane of the layers.

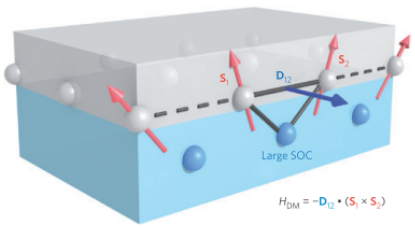

Fig. 2.11: Schematic of a DMI between the neighboring spins that results from indirect exchange mechanism for the triangle composed of two atomic spins and an atom with a strong SOC. Image from [Fer+13].

From equation 2.21 and Figure 2.11 DMI favors non-collinear structures, with the canting of neighboring spins rotating in the plane normal to $\mathbf{D}$. For ferromagnetic films with PMA, the DMI therefore favors Néel walls.

The *ab initio* techniques for quantitative calculations of this interaction [Hei+11] confirmed its importance for ultrathin films, and it was shown experimentally that the DMI modifies the nature of the magnetic DWs, forcing the Néel-type DW instead of the Bloch-type DW in perpendicularly magnetized thin films [Hei+08].

2.3.2 Domain wall dynamics in the presence of DMI

In films in non centrosymmetric stacks where DMI stabilizes chiral Néel walls, the domain wall dynamics changes with respect to the behavior that has been shown in Section 2.2.4.

In symmetric systems the domain walls reach the maximum velocity at the Walker field, thereafter the velocity drops because of the precession of the magnetization within Bloch walls. However, in systems with sufficiently strong DMI, domain walls in ultrathin films are expected to have Néel form with fixed chirality.

The DMI can be seen as an effective field (H_{DMI}) (Eq. 2.22) perpendicular to the DW direction, stabilizing the Néel form against precession (Fig 2.12).

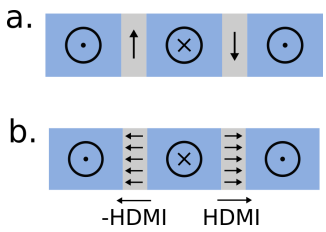

Fig. 2.12: Sketch of **a.** a Bloch wall and **b.** a chiral Néel domain wall, stabilized by DMI (top view).

This field has been shown to be expressed by [Thi+12]:

$$H_{DMI} = D/(\mu_0 M_s \Delta) \tag{2.22}$$

where D is the DMI energy density, M_s is the saturation magnetization and Δ is the DW parameter.

As a consequence in systems with DMI it is observed that the DW mobility in the stationary regime does not change with respect to symmetric stacks, but the Walker field is pushed towards larger fields proportional to the strength of the DMI (D). Therefore the maximum DW velocity increases with D as shown in the Figure 2.13.

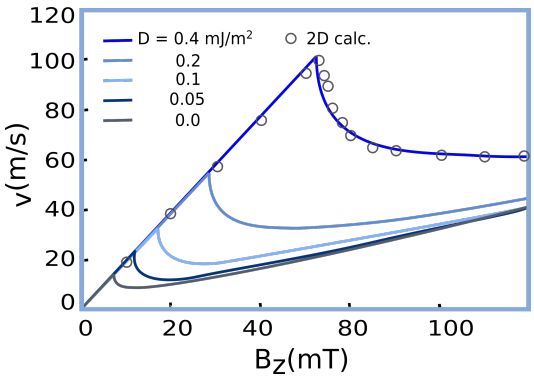

Fig. 2.13: 1D calculations of velocity *vs.* out-of-plane field for Pt/Co/AlOx with different values of D. Image adapted from [Thi+12].

Thiaville *et al.* [Thi+12] predicted that in the presence of sufficiently large DMI, the Walker field is given by expression:

$$H_w = \frac{\pi \alpha H_{DMI}}{2} \tag{2.23}$$

Using the mobility of the flow regime (eq. 2.16) and with $H_z = H_w$ we have:

$$v_w = \gamma_0 \frac{\Delta}{\alpha} H_w \tag{2.24}$$

making the necessary substitution for H_w using equations 2.22 and 2.23, the speed at the Walker field is:

$$v_w = \frac{\pi}{2} \gamma \frac{D}{M_s} \tag{2.25}$$

This expression shows that in systems with DMI the maximum DW velocity at the Walker field is expected to be proportional to the strength of the DMI and inversely proportional to the saturation magnetization.

2.4 Dynamics under spin polarized current

The fundamental concepts of spintronics are based on the generation, detection, and manipulation of spin polarized currents. A lot of studies were performed in recent years aiming at the development of a new generation of the magnetic memories based on the movement of domain walls by spin currents (racetrack memories).

In this section we will discuss some concepts of spin transfer torques (STT) and spin-orbit torques (SOT).

2.4.1 Spin-transfer torque (STT)

When a spin polarized current passes through a ferromagnetic layer its spin polarization changes (alignment with the magnetization) due to exchange interaction between conduction electrons and electrons in 3d bands. Since the total angular moment is conserved, the conduction electrons transfer their angular momentum to the magnetization of the ferromagnetic layer. This results in a torque applied on the magnetization.

For this reason the spin transfer torque is an effective way of changing the magnetization, which is used as a new writing scheme in memory and logic devices [Riz+13].

This torque can induce different physical effects and in particular magnetization reversal in spins valves or magnetic tunnel junctions as well as motion of the DWs in magnetic nanostripes.

L. Berger made the first studies of the interaction between electrical current and a DW. He proposed that electrons passing through the domain wall induce a torque which can drag the DW along the electron flow direction [Ber74].

This concept was demonstrated by Parkin *et al.* [Par+08] for Permalloy ($Ni_{81}Fe_{19}$). Figure 2.14 shows the position of a DW in a nanowire, measured with magnetic force microscopy (MFM). The DW was created and displaced by single current pulses. It was observed that depending on the current direction, the DW moved in either direction along the nanowire, but the DW motion is always in the direction of the electron flow (opposite to the current direction). These measurements carried out for a system with in plane magnetization (in this case, Permalloy) highlighted the fact that the domain walls can be easily pinned by defects, so that this effect is still not exploited in real devices like racetrack memories.

2.4.2 Spin-orbit torque (SOT)

The dynamics of the domains walls in systems with large PMA has been intensely studied and the DMI does play an important role as it imposes the nature of the DW internal structure and therefore modifies its field and current-driven dynamics.

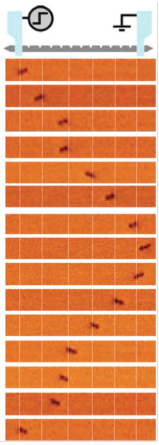

Fig. 2.14: MFM was used to image the motion of vortex DW. A nanowire comprising a series of notches was connected to electrical contacts at each end to allow for injection of current pulses. For the first eight images, pulses with negative polarities were applied. For the last seven images, pulses with positive polarities were applied. Image adapted [Par+08].

In centrosymmetric systems such as Pt/Co/Pt, DWs move slowly and only with the support of an out-of-plane field, when driven by spin-polarized current. On the other hand, in non-centrosymmetric systems, the DWs move all in the same direction and large speeds can be reached (some 100m/s) [Emo+14; Mir+11; Ryu+13].

Figure 2.15a. shows an example of measurements made by M. Miron et. al. [Mir+11] on 500nm wide strips of Pt/Co/AlOx. In the initial state, two domain walls are introduced into each of the strips by perpendicular magnetic field pulses; the current pulses applied via two Ti/Au electrodes connected to the strips then move each domain wall in the direction of the current. In the differential Kerr images, the displacement of each domain wall ↑↓ or ↓↑ appears as a black or white contrast. The domain wall velocities as a function of current density are shown in Figure 2.15b. We distinguish the thermally activated regime (creep) followed by the linear regime (flow), analogous to the case of measurements made with a magnetic field.

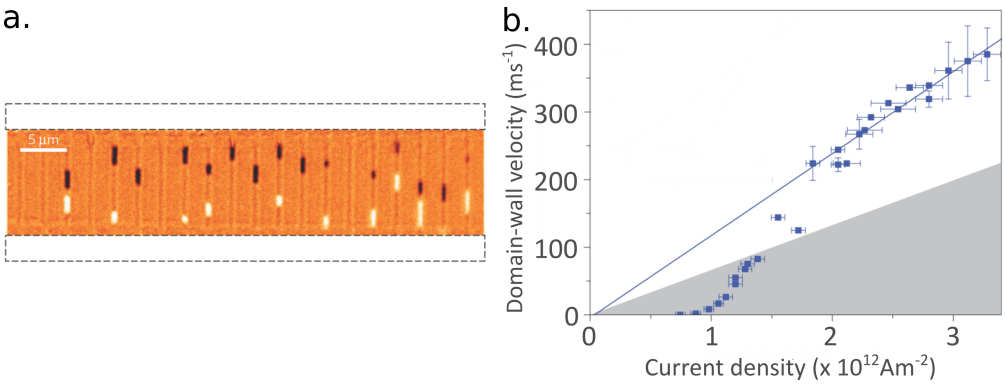

Fig. 2.15: **a.** Kerr image showing the domain wall displacements induced by 15×0.64 ns current pulses of density $2.6 \times 10^{12}\text{Am}^{-2}$ in Pt/Co/AlOx. **b.** Domain-wall velocity as a function of the current density. Image from [Mir+11].

The large mobility of DWs in Pt/Co/AlOx was first interpreted in terms of STT and the presence of a Rashba effect at the Co/AlOx interface. However today we know that this concept fails, one of the reasons being that DWs in Pt/Co/AlOx move in direction opposite to the electron flow. Nowadays, the dynamics of the DWs in systems with DMI is attributed to the so called spin-orbit torque (SOT) that can have two origins, the Rashba Effect (RE) and the Spin-Hall Effect (SHE).

When a current flows in a heavy metal with large SOC, such as Pt, spin up and spin down electrons are deviated in different directions due the Spin Hall Effect [VT06]. This generates a pure spin current transverse to the charge current. If the translation symmetry is broken by the presence of the interface, this will create a spin accumulation at the interface. The direction of the spins is perpendicular to the current direction and parallel to the interface. (Fig. 2.16)

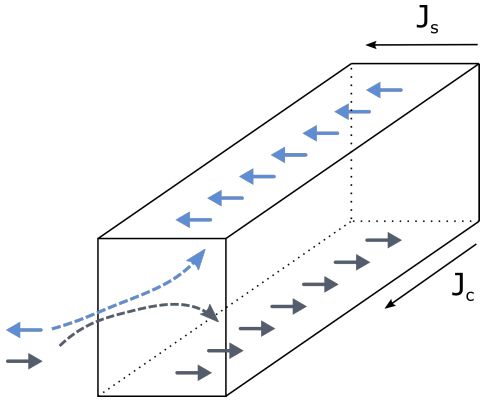

Fig. 2.16: The schematic diagram of the formation of transverse spin accumulation in heavy metal due to the Spin-Hall Effect.

The torque $\overrightarrow{\tau_1}$ acting on the DW magnetization has the form:

$$\overrightarrow{\tau_1} = -\gamma\tau_1(\hat{m} \times \hat{\sigma} \times \hat{m}) \tag{2.26}$$

where $\hat{\sigma} = \hat{j} \times \hat{z}$ is the direction of the spin accumulation, and $\hat{m}, \hat{j}$ and $\hat{z}$ are the unit vectors in the direction of the DW magnetization, of the current and of the out-of-plane direction and γ is the gyromagnetic ratio.

On the other hand , the torque $\overrightarrow{\tau_2}$ associated with the Rashba effect (RE) can be written as:

$$\overrightarrow{\tau_2} = -\gamma\tau_2(\hat{m} \times \hat{\sigma}) \tag{2.27}$$

The torque $\overrightarrow{\tau_1}$ (Eq.2.26) has the same geometry as the Slonczewski torque (SLT), whereas $\overrightarrow{\tau_2}$ (Eq. 2.27) presents the same geometry as the field like torque (FLT). Considering a system with PMA, with DWs either Bloch or Néel, the Rashba torque does not have the right symmetry to move the DWs. The torque associated with the SHE is associated with an effective field having symmetry ($\hat{\sigma} \times \hat{m}$). This field is perpendicular to the plane, and could therefore induce a displacement of the DW, if the DW has the Néel form, being zero for Bloch walls.

Therefore, the high DW mobility in the studied Pt/Co/AlOx strips can be explained by SHE-SOT, if the DWs had a Néel structure. The SHE generates a pure spin-current in Pt and this diffuses across the Pt/Co interface. Since such a spin-current has an in-plane spin polarization transverse to the strip it is able to exert a torque on the magnetization of the Néel wall (which is oriented normal to DW direction). Thiaville *et al.* [Thi+12], using the Thiele force equation approach, found that the SHE-SOT is equivalent to an effective field:

$$H_{eff} = \frac{\pi}{2}\chi M_s \cos\Phi \tag{2.28}$$

with $\chi = \hbar\theta_H J/(2e\mu_0 M_s^2 t)$ representing the SHE-induced STT [SM06] and J the current density. This model indicates that the DW velocity under SHE increases with DMI parameter (Fig 2.17). Here Φ is the angle of the magnetization within the DW directive; $\Phi = \pi/2$ for Néel wall at rest and Φ deviates from $\pi/2$ as the current increases. The larger speeds for large D are related to the stronger stability of Néel walls as DMI increases.

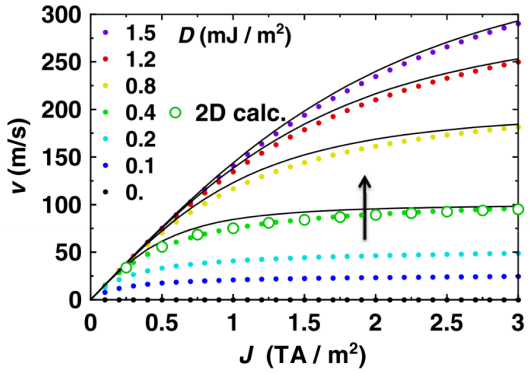

Fig. 2.17: Current-induced motion due to the spin Hall effect in the underlayer of several values of D, with results of 2D calculations superposed for one case (arrow depicts D increase). The magnetic parameters are those of Pt/Co(0.6nm)/AlOx from [Mir+11]. Image from [Thi+12].

The presence of the chiral Néel walls helps to explain the direction of the wall displacement induced by current via SHE-SOT in HM/FM/MOx systems (heavy metal/ ferromagnet/ oxide) (Fig. 2.18). The direction of the movement depends

indeed on the sign of the spin Hall angle (which depends on the heavy metal), on the DMI sign (which depends on the nature of the metal interface heavy/ferromagnetic), and on the direction of electrons or current. So DW can move in the direction of current or in the direction of electrons depending on the pair substrate /FM.

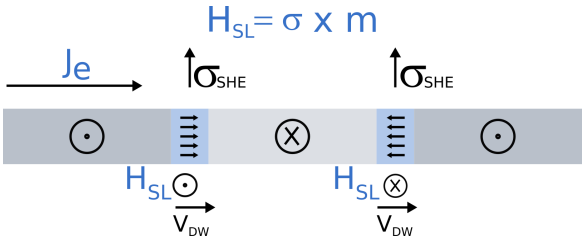

Fig. 2.18: Diagram of the magnetic configuration in a system with DMI: m opposite for two adjacent walls. The direction of the spin current is fixed by the material. The torque exerted on the two walls is opposite.

This effect also allows explaining why ↑↓ and ↓↑ chiral Néel DWs move in the same direction. Since the direction of the magnetization is pointing in opposite direction in two adjacent walls (see Fig. 2.18), the effective out-of-plane magnetic field H_{SL}. $(\hat{\sigma} \times \hat{m})$ have also opposite direction and therefore move the DW in the same direction.

3 Methods

This chapter describes the experimental methods used during this thesis for the preparation of the samples and the characterization of the structural and magnetic properties of the films. Samples were prepared by the magnetron sputtering method and in particular situations, they were nanostructured using photolithography (Section 3.1). X-Ray Reflectivity (XRR) technique was important for the analysis of structural properties of our samples and it is described in the section 3.2. For the analysis of magnetic properties, this thesis is relying on measurements with Kerr microscopy, vibrating sample magnetometry (VSM) and X-ray Magnetic Circular Dichroism (XMCD). We will discuss these in section 3.3.

3.1 Sample preparation

The method used to produce thin films is of importance when we intend to study the magnetism of our samples. It is important to have control of the layers which form the sample, knowing the thickness and having a reproducible process. The processes used for depositing and for patterning are briefly discussed in this section.

3.1.1 Sputtering method

While when it was first discovered it was regarded as an undesired phenomenon, today, the sputtering method is widely used for thin-film deposition, cleaning surfaces and etching, among other applications in the industry and research. Grove in 1852 was the first to observe that the energetic ions in the gas discharge sputtered the cathode surface inside the discharge tube and the cathode material was deposited on the inner wall of the discharge tube [Was+04].

The basic process for the sputtering method is given by the interaction of incident particles with the target surface atoms, or the source of the material desired to be deposited. These incident particles are energetic ions, typically inert such as Argon (Ar^+) since the other rare gases as Xenon and Krypton are quite expensive with respect to Argon.

There are different ways to sputter metallic samples, but the most important for this thesis was the magnetron sputtering method, since all our samples were made by this process.

Magnetron sputtering

This method follows the basic process, where the target is bombarded by the accelerated ions then the extracted material is deposited on the substrate.

In the first step, Argon atoms are introduced into a vacuum chamber at the pressure of $\approx 5 \times 10^{-7}$mbar. The Argon plasma is obtained by an electrical discharge that will ionize the argon atoms by collisions with the electrons. The minimum necessary pressure to light the plasma is $\approx 10^{-3}$mbar.

These Argon ions are now charged positively and are attracted by the target and when colliding with it eject the target atoms, which are then condensed onto a substrate to form a film as shown in the Figure 3.1.

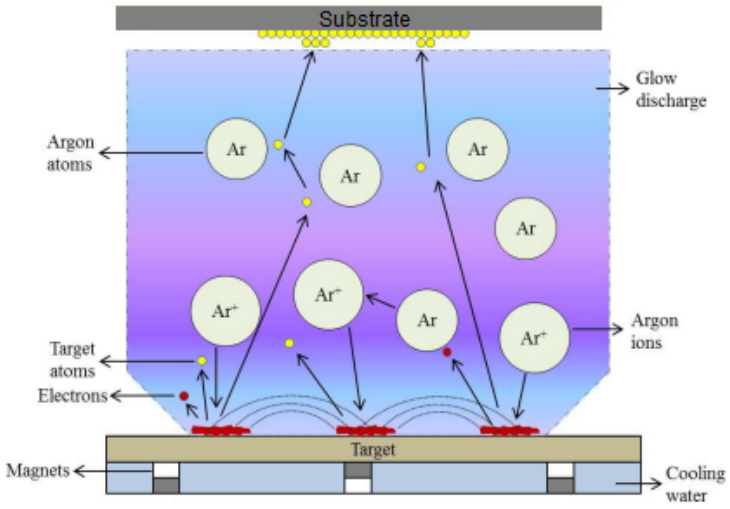

Fig. 3.1: Schematic of magnetron sputtering system where the argon plasma confined into the region between the target and substrate bombards the target that forms a thin layer on the substrate [Mau+14].

The main difference between the basic method and the one we used is the addition of a strong magnetic field near the target area and this modifies how the electrons travel towards the substrate.

If the target is conducting, a DC power supply is generally required, but if there is an impedance between the power supply and sputtering gun, an RF power supply

is used. In the case for RF, positive charge accumulation is reduced, eliminating the problem of low deposition rate and plasma ignition.

In general, this method has the following advantages [Swa88]:

- High deposition rates;
- High adhesion of films;
- High-purity films;
- Excellent uniformity on large-area substrates.

Details about samples preparation

The equipment used at Institut Néel is an Alliance Concept multi-cathode sputtering system, which allows one to prepare multilayer samples with up to 8 materials.

In the geometry presented in Figure 3.2a. (target in front of the substrate) the film thickness is homogeneous over a circular region of radius around 3cm.

By shifting the substrate with respect to the center of the target, as we show in Figure 3.2b., samples with a thickness gradient can be prepared. This produces a gradient of magnetic properties (e.g. magnetic anisotropy), controlled by the thickness of the elements deposited on the wedge.

Usually, the distance *h* between the target and the substrate (Fig 3.2) was set to 100 mm, but this was sometimes changed because by tuning this distance it was possible to obtain different thickness gradients (the larger the distance the smaller the gradient).

All multilayer samples were grown on commercial Si/SiO_2 substrates at room temperature. The typical layers studied in this thesis were Si/SiO_2 – Ta/Pt/Co/M or Ta/Pt/Co/MOx with M = Al, Gd or Tb. The thickness of the Ta, Pt and Co was kept constant , while the top metal was deposited in the form of a wedge with variable thickness. The oxidation of M layer was obtained with an oxygen plasma. The thickness gradient of M or MOx gives rise to a gradient of PMA, as we show in Chapter 5. The deposition was carried out in Argon atmosphere. Before the process of deposition, the targets need to be cleaned in order to remove the oxide surface on top of the target.

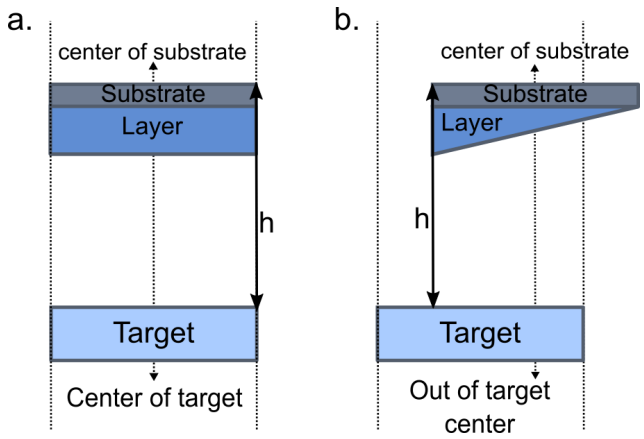

Fig. 3.2: **a**. In usual case of the depositions, the center of the sample holder and the target are in the same vertical axis. **b**. In order to get a thickness gradient on the substrate, we shift the sample holder off the center of the target.

3.1.2 Patterning of magnetic nanostripes

Some of the samples were prepared in the form of narrow strips for current induced domain wall dynamics. The narrow strips ($\leq 1\mu$m) were prepared by electron beam lithography and ion beam etching while the electrical contacts (typically Ti/Au) were prepared by UV lithography and lift-off.

UV and deep-UV Lithography

This is a technique that uses a UV lamp to insolate a photoresist through a mask partially transparent to the light. The resist which is a polymer sensitive to the UV light is spread on a substrate by spin-coating technique. This resist can be positive or negative if the solvability of the exposed areas increase or decrease under light exposure, respectively.

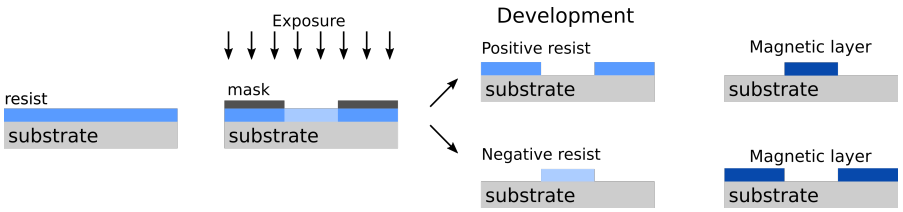

Fig. 3.3: Insolating of a resist using a mask. Development in case of a positive resist and negative resist.

The type of resist, the UV lamp, the time of exposure, as well as the material of the mask and the wavelength and power of the used UV light are the important parameters for the quality of the pattern and the number of defects and resolution.

This technique is usually used for structures of size down to approximately 500nm using a chromium mask.

Lift-off Technique

The concept of this technique is to deposit the material by evaporating or by sputtering techniques on the developed resist pattern. The resist is then dissolved by a solvent that depends on the type of resist. The material deposited on top of the resist is removed and only the material deposited on the substrate will remain.

Electron Beam Lithography and Ion-Beam Etching Technique

This technique consists of exposing a resist by a focused electron beam. It is commonly used to fabricate structures of the order of tens to hundreds of nanometers.

Ion beam etching (IBE) is used to remove material from the etch target by bombardment with directed and precisely controlled ion energy. The IBE source generates a plasma from a noble gas, typically Argon.

The principle of the process is to first deposit the multilayer stack on the Si substrate. A resist is used to create the wanted pattern on the top of magnetic layer by e-beam lithography.

The resist can act as a hard mask during the etching of the sample by a broad ion beam. In this way, the pattern is transferred to the magnetic layer.

The disadvantage of this method is that the resist is difficult to remove from the top of the pattern after the etching, preventing the observation of magnetic contrast by Kerr microscopy. The resist may be burned away with oxygen plasma, but this process is not suitable for structures which are sensitive to oxidation, which is our case in magnetic trilayers.

Another way, which proved to be more suitable for our study, consists of using a hard metallic mask (e.g Ti or Al) on top of the magnetic layer, rather than a negative resist as mask (Fig 3.4).

This metallic mask is prepared by evaporation and lift-off process of the metallic layer following the e-beam lithography.

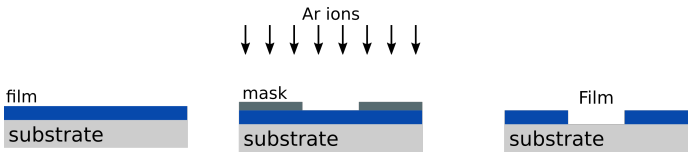

Fig. 3.4: Ion Beam Etching technique using a metallic mask which is prepared by lift-off technique.

The ion beam strikes the substrate, removing material by physical sputtering. To control the endpoint of the etching we used SIMS (secondary ion mass spectroscopy) that monitors the sputtered material species, allowing etching to be stopped at a specific layer.

Details about patterning at Institut Néel

All the patterning were performed at Nanofab - Institut Néel.

For UV lithography the S1805 photoresist was spin coated with a rotation speed of 4000 rpm/s which gives us ~500 nm of thickness. The resist was then annealed at 115°C during 1 min.

For the UV exposure process, we used a UV KUB 2, that is a compact exposure-masking system equipped with a LED based optical head, collimated and homogeneous and the time for exposure was 30 s. For the lift-off technique, we used acetone like solvent.

The e-beam lithography was carried out using a Zeiss LEO scanning electron microscope.

For the narrower strips needing electron beam lithography, we used PMMA (polymethyl methacrylate) 4% resist. Titanium deposited by evaporation was used as a hard mask.

3.2 Structure properties

After the process of thin multilayer film production, it is important to obtain structural information about these films, like the thickness that is necessary for quantitative evaluation of magnetic properties, the layer roughness in order to verify the existence of inter-diffusion or roughness of some layers. In this section, we discuss briefly the method that we used to do this characterization.

3.2.1 X-Ray Reflectivity - XRR

X-ray reflectivity (XRR) is a useful technique to evaluate quantitatively thickness, roughness, and density of thin layers allowing the characterization of thin films in nanometric range. Among its advantages appear the capacity to analyze multiple-layer systems, with a non-destructive and non-contacting method. Figure 3.5 shows the sketch of the experimental setup used at the Institut Néel.

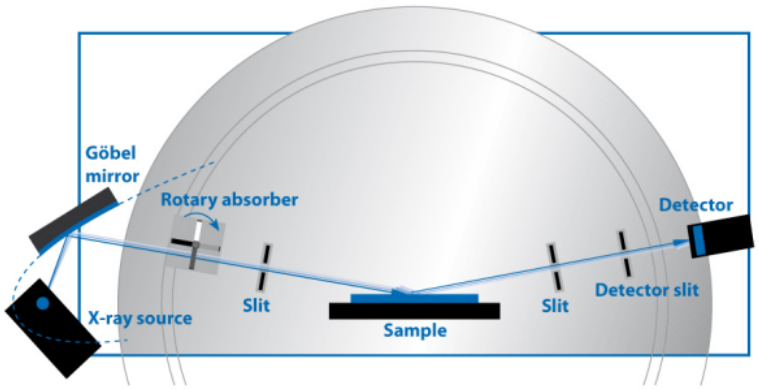

Fig. 3.5: Schematic representation of Bruker's XRR experimental setup (adapted from [BRU10]).

XRR involves monitoring the intensity of the X-ray beam reflected by a sample at grazing angles so that a monochromatic X-ray beam of wavelength λ irradiates at grazing angle θ and is reflected at 2θ and recorded by a detector.

The measurement is operated in a mode where the incident angle is always half of the angle of diffraction. Different reflections occur due to different electron densities in the different layers. The total external reflection occurs when the incident angle θ is below a critical angle θ_c (Fig 3.6a). With this angle we can determine the density of the top material.

When the incident angle θ is above θ_c the x-rays start penetrating in the material and the reflection from the different interfaces interfere and give rise to interference fringes (Fig 3.6b).

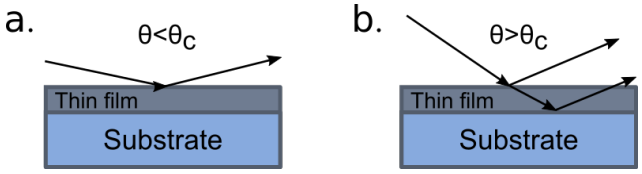

Fig. 3.6: **a.** Schematic view of X-ray reflection when the incident angle is lower and **b.** higher than the critical angle θ_c (adapted from [Col+08]).

The reflectivity curve presents therefore a series of oscillations called Kiessig fringes [Kie31], where the period of the interference fringes and the fall in the intensity are related with the thickness and the roughness of the different layers in the case of multilayers.

Figure 3.7 shows the typical reflectivity curve and sketches the information that can be extracted from the curve: thickness, roughness and density of the material. The shape of the curve before θ_c depends on the size of the sample, the roughness and the other instrumentation parameters. This region is typically flat. The point where appears the first drop of the intensity corresponds to the critical angle.

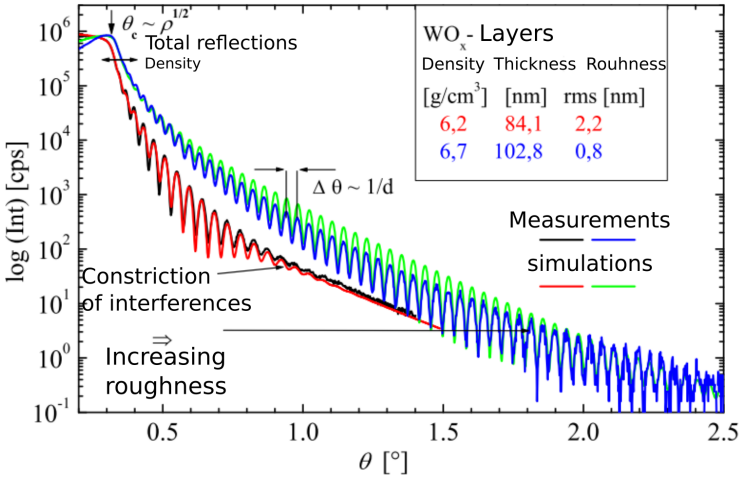

Fig. 3.7: Typical curve of reflectivity with indication about the information extracted from the oscillations.

The measured curves are fitted with the theoretical curve, using the standard Parrat algorithm, until the best agreement between measured curves and theoretical curve is obtained [Par54; Gar+11].

Details about the system at Institut Néel

All the XRR measurements were performed at Institut Néel using a $\theta - 2\theta$ Bruker D8 Discover diffractometer with Cu K-alpha radiation. The focused beam on the sample is 0.5 mm^2 in the incidence plane. The data were collected using a scintillation detector for incident angles up to around 8° for 2θ reflection angles. The acquisition time was 5 sec/step and the increment between two consequents points was of 0.01°.

The quantitative analysis of the XRR measurements was carried out using the Bruker LEPTOS software.

3.3 Analysis of magnetic properties

The main aim of this work was to understand domain wall dynamics in magnetic multilayers. The technique used to observe the magnetic domain structure, combined with other macroscopic magnetic characterizations and local measurements of magnetic properties will be discussed in this section.

3.3.1 Kerr Microscopy

Among the many methods to observe magnetic domains, a classical technique is Magneto-optical Kerr effect (MOKE). MOKE is the effect by which the light reflected from the magnetic surface can change its polarization.

John Kerr discovered in 1877 and 1878 that the polarization state of plane-polarized light is rotated when reflected from a magnetic surface [Wei08], but a similar effect was first discovered by Faraday in 1846, who started the history of magneto-optics with the discovery of the rotation of the polarization plane when linearly polarized light propagates through a flint glass under an applied magnetic field [Far46].

August Köhler from Carl Zeiss corporation in 1893 has contributed with the illumination technique called wide-field microscopy, which helped to obtain homogeneously illuminated images with maximum resolution. With this concepts, the Kerr microscopy is explained by the ray diagram in the Figure 3.8.

The figure shows separately the illumination and the image-formation light path. The light emitted from the lamp passes with oblique angle the collector lens and is focused onto the plane of the aperture diaphragm, then passes through the opening and variable field iris diaphragm, is then polarized and deflected downwards into the objective lens by a partially reflecting plane glass mirror. After being reflected from the sample, the light passes through a half-mirror, before the image is focused by the tube lens onto the CCD camera (Fig. 3.8b.).

Depending on the relative orientation of the magnetization $\vec{M}$ of the surface of the sample with respect to the plane of the light incidence, there are three possible configurations for the Kerr effect [Kuc+15] shown in the Figure 3.9.

These different cases show different modes of rotation effect of MOKE that can be described by the dielectric tensor. The dielectric law is written as:

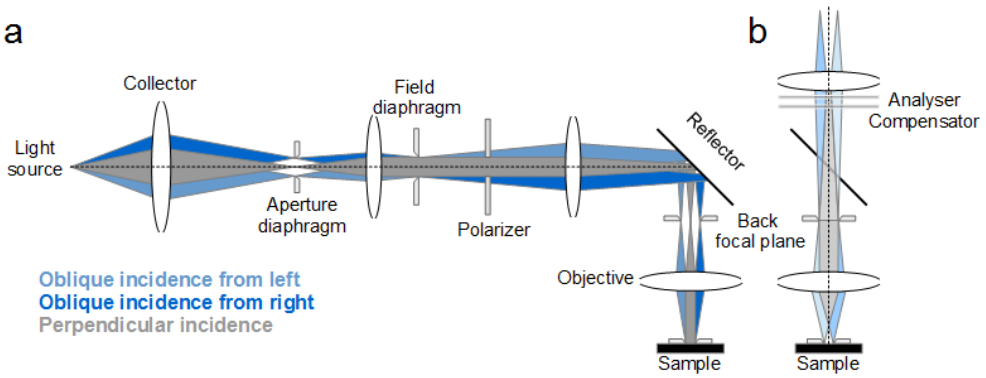

Fig. 3.8: **a.** Illumination light path for perpendicular incidence. **b.** Image-forming path. (adapted from [SS16]).

$$\mathbf{D} = \varepsilon \mathbf{E} \tag{3.1}$$

where **D** is called the induced electrical displacement vector, whereas ε is the dielectric permittivity tensor and **E** the electrical field vector. Using the term in the equation 3.1, the dielectric law can be generalized with concepts of dielectric permittivity tensor [HS08] as:

$$\mathbf{D} = \varepsilon(\mathbf{E} + iQ_v \mathbf{m} \times \mathbf{E}) \tag{3.2}$$

Here **D** is the displacement vector that represents the secondary light amplitude that is produced by magneto-optical interaction between **E** and **m** , where **E** is the electrical vector of incident light and **m** the magnetization vector in the sample. However, ε is the dielectric permittivity antisymmetric tensor including the components of the magnetization vector and Q_v a constant correlated to the material parameters that is roughly proportional to the saturation magnetization.

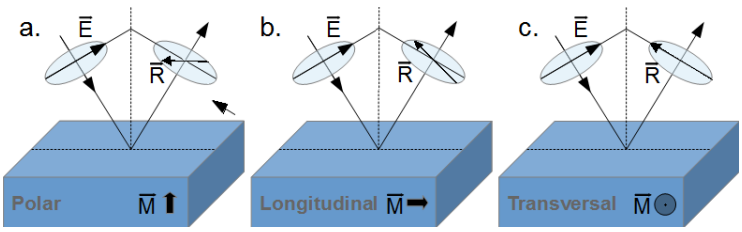

Fig. 3.9: Schematic showing three different MOKE geometries: **a.** Polar, **b.** longitudinal and **c.** transversal.

The three different geometries of MOKE are shown in the Figure 3.9. The first case is the polar Kerr effect (Fig 3.9 a.), where the magnetization vector is perpendicular (out-of-plane) to the reflection surface and parallel to the plane of incidence. The

polar signal will be maximum when the angle between the surface normal and the direction of the light is zero.

For the longitudinal case (Fig 3.9 b.), the magnetization vector is in the sample plane and in the incident plane. In this geometry, the Kerr amplitude vanishes if the angle between the surface normal and the direction of the light is zero. The longitudinal MOKE is sensitive for samples with in-plane magnetization lying in the incident plane.

For the last case, the transversal MOKE (Fig 3.9 c.), the magnetization is in-plane but transverse to the incidence plane. The light arrives with an angle and the magnetization is measured by the variations of reflectivity.

Microcoils: structure and fabrication

One way to promote the DW displacement that we studied by a wide-field Magneto-Optical Kerr microscope is with a magnetic field parallel to the easy axis, H_z (out-of-plane). In order to reach high DW speeds, it is important to reach high Hz magnetic fields. These high fields with amplitude up to 600 mT were obtained with microcoils fabricated at Institut Néel.

The concept of the microcoil is schematically shown in the Figure 3.10 [Bon01]. The inside diameter was 200 μm, the external dimension was approximately 5 mm.

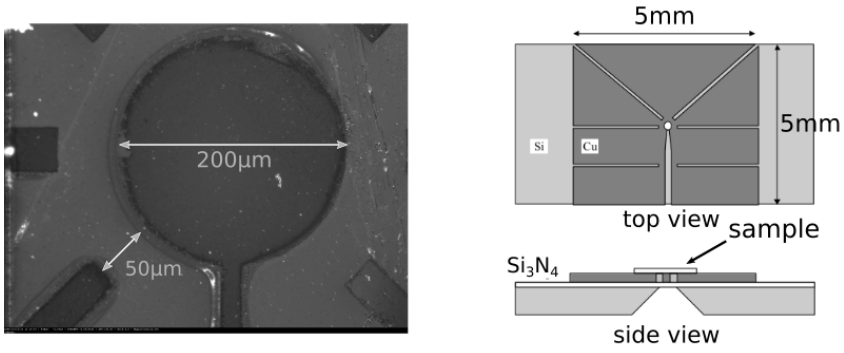

Fig. 3.10: Copper microcoil used for the domain wall dynamics experiment.

Microcoils were obtained starting from a substrate SiO_2 with a layer of Si nitrate Si_3N_4 on both faces. A photolithography process on the substrate back side is carried out, defining a pyramidal opening with a window $200\mu m \times 200\mu m$ on the front face of the SiO_2. A thick layer of photosensitive resist with the coil pattern is lithographied on the other side.

This is then filled by an electrolytic deposition of Cu.Thereafter the resist is removed and the Si_3N_4 window left on the back side is removed with HF.

The coils have a copper thickness of ≈ 3 μm and act to increase mechanical inertia and also help dissipating heat between pulses. In addition, it improves the adhesion of the coil to the substrate and silicon is an ideal substrate because most micro-machining techniques have been developed around this material, a relatively good heat sink for copper.

The sample is glued on the microcoil, so that the magnetic film lies as close as possible to the coil surface, this distance being usually around 20 μm and the microcoils was connected with flat cable.

Figure 3.11 shows the calculated distribution of the field amplitude for coil diameter 100 μm and 200 μm along the diameter of the coil and along the z-axis (courtesy of M. Bonfim).

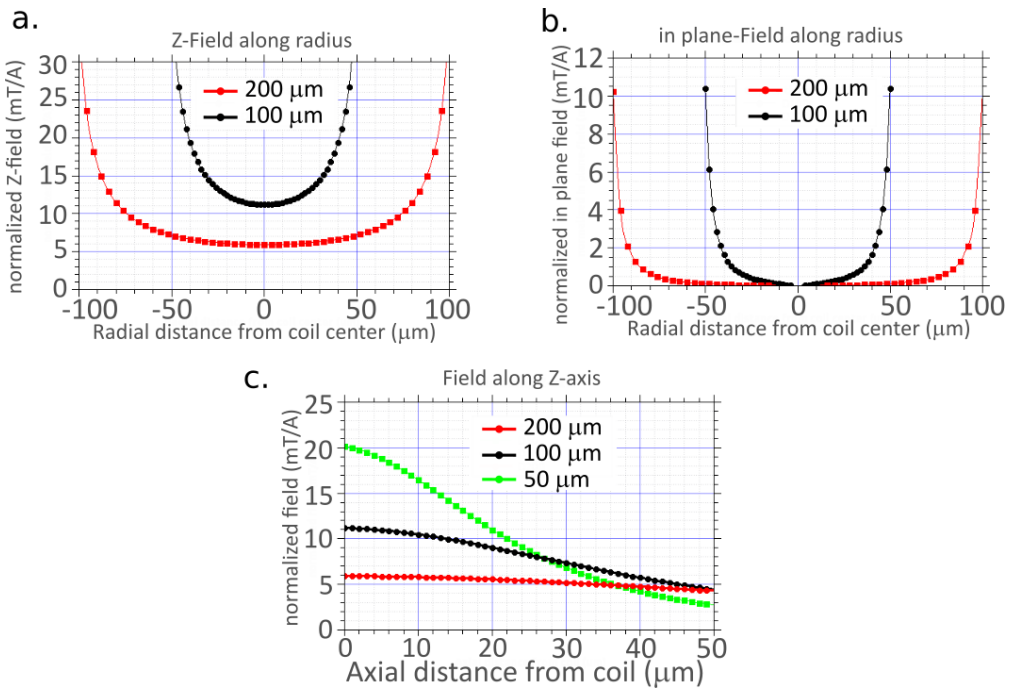

Fig. 3.11: Calculated distribution of the magnetic field for a coil of diameter 200μm and 100μm, **a.** out of plane magnetic field along the diameter of the coil. **b.** In plane field along the diameter of the coil. **c.** H_z as a function of the distance from the plane of the coil.

It is possible to notice that using 200 μm coil the H_z field is very homogeneous along the coil radius except very close to the edges. This is not the case for the 100 μm coils. In order to have a large region where domain walls can be moved with constant field, 200 μm coils have been chosen. Note also that close to the edges the in plane component of the field starts being not negligible. Another advantage

of the 200 μm coil is that the field changes less rapidly as a function of sample distance (z-direction).

Note for example that while for 50 μm coil the field is reduced to 50% of its value for 30μm distance, the change is less than 10% for the 200 μm coil.

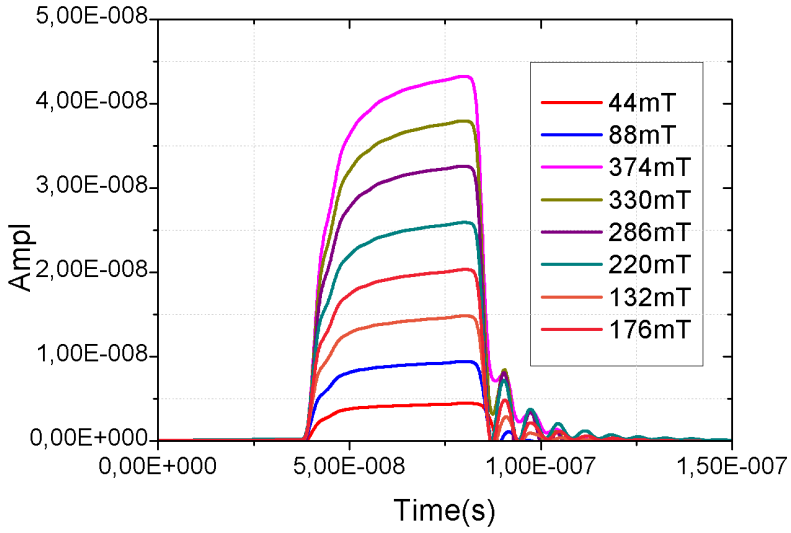

Fig. 3.12: Shape of pulse on microcoil applying different fields.

Power supplies for pulsed currents to be injected into these coils were fabricated at Institut Néel using the design provided by Marlio Bonfim from Federal University of Paraná -Brazil (UFPR).

To produce very high magnetic field the microcoil is the placed in a RLC (resistor - inductor - capacitor) circuit and the pulse was produced by a capacitor discharge.

The shape of the pulse was measured as the integral of the flux through an induction coil. The measurement is shown in Figure 3.12, for different values of the high voltage used to charge the capacitor. The oscillations is due to connections.

Details about the Kerr set-up at Institut Néel

The Kerr microscope at Institut Néel was used to carry out many types of measurements necessary for the magnetic characterization of our samples. In this thesis we will show hysteresis curves measured using classical electromagnets for perpendicular field, and images of magnetic domains where DW are moved either with fields produced using microcoils or with currents pulses.

A commercial wide-field Zeiss microscope, modified to allow Kerr microscopy has been used. The optical components are shown in the Figure 3.8.

To collect the magnetic images and to measure hysteresis loops, a LabView based software developed by the Evico company was used. A 630 nm diode is used as light source.

Some extra instrumentation was necessary to carry out the measurements:

- Power Supply
  A Kepco BOP 100-4M was used as source of voltage for the electromagnets (out-of-plane and in-plane). This is a ±100 Voltage ±4 Ampere Bi-polar power supply controlled by a BIT-232 serial interface card integrated into LabView. Because of bi-polarity, we can easily obtain positive and negative fields and measure hysteresis loops.

- Pulse /Pattern Generator
  When it was necessary to trigger the applied field, we used an Agilent 81110A Pulse Pattern Generator, 165/330 MHz, with BNC outputs connections, Single-/dual-channel pulse pattern generator and integrated into LabView.

- DC Power Supply
  To power the capacitor of the current generator associated to microcoils, we used the equipment from Delta Eletronika - ES0300 - 0.45. The range voltage it is 0 – 300V and also integrated into LabVIEW by RS323 connection.

3.3.2 Vibrating Sample Magnetometry and Superconducting Quantum Interference Device (VSM SQUID)

The quantitative magnetic characterizations of the films presented in this thesis were carried out with a VSM-SQUID.

Created by S. Foner [Fon96], the VSM is a technique widely used in laboratories for having a good performance and a simple mode of operation.

The concept is based on the flux change detected by a pair of pick-up coils when the sample is vibrated perpendicularly, to the field to which it is submitted. Due to the relative motion between the sample and the pick-up coils, a voltage is induced in the pick-up coil, which is proportional to the magnetic moment of the sample.

The sample is attached to the end of a nonmagnetic rod, the other end of which is fixed to some kind of mechanical vibrator.

A SQUID magnetometer is more sensitive than a regular VSMs. Besides the high sensibility (10^{-9}emu), this equipment has an excellent system control of temperature with the possibility to change from 1.8 to 400 Kelvin using liquid helium.

The principle of the operation of SQUID is based on the Josephson effect. This effect was predicted in 1962 by Brian Josephson [Jos62], so that since then, two superconductors separated by the insulating layer has been called a "Josephson junction". The SQUID consists of a loop with one or two Josephson junctions (SQUID RF or DC) interrupting the loop (see Figure 3.13). This is a device that can measure magnetic flux quanta passing through its loop.

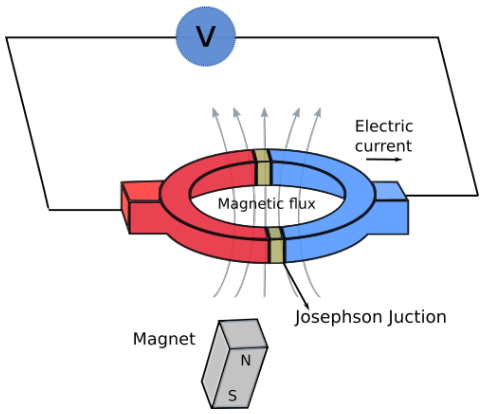

Fig. 3.13: DC SQUID, a superconducting loop contains two Josephson junctions (the insulator part in yellow) sandwiched between two superconductors (blue and red).(Image adapted from [Sim12]).

Details about the system at Institut Néel

The measurements were carried out at Institut Néel using a commercial instrument manufactured by Quantum Design model MPMS-XL.

The main elements of the magnetometer are:

- a superconducting magnet to produce the high magnetic fields
- two detection rings and two compensation rings
- a SQUID connected by superconducting wires to the detection coils

This instrument offers a sensitivity (with less than 10 seconds of average) of 5×10^{-8}emu at the full field of 7 Tesla.

For the temperature control the design allows the cooling rate of 300 K to 10 K stable in 15 minutes and between 10 K to 1.8 K this happens in 5 minutes.

3.3.3 X-Ray Magnetic Circular Dichroism - XMCD

Pioneered by Gisela Schütz in 1987 [Sch+87] XMCD has developed as an important method to investigate microscopic magnetic properties of magnetic systems, having large sensitivity and atomic selectivity using a synchrotron source.

XMCD is the difference of two X-ray absorption spectra (Fig. 3.14 b.), one taken with might right circularly polarized light and one with left circularly polarized light, carried out with polarized synchrotron radiation as shown in the Figure 3.14a.

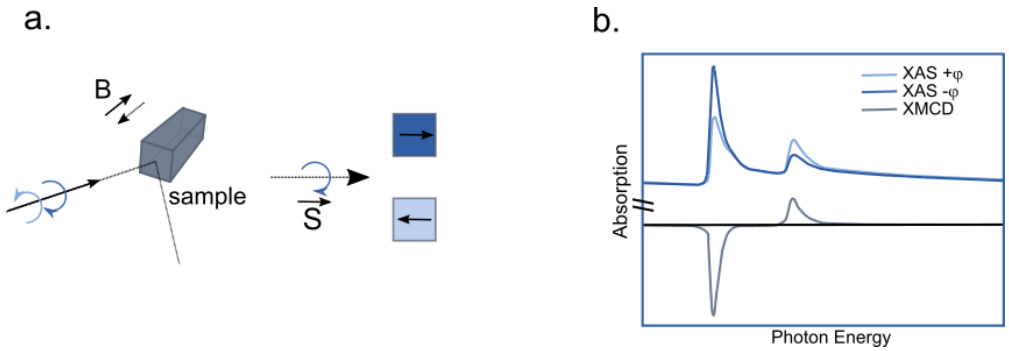

Fig. 3.14: **a.** Experimental set up for XMCD measurements **b.** Illustration the size of magnetic dichroism effects.

The XMCD is proportional to the magnetization that is observed if the photon spin direction and the magnetization directions are parallel or anti parallel [SA00] in the Figure 3.14 a. Sum rules allow relating the XMCD intensities at the $L_{2,3}$ absorption edges to the spin and orbital moments of the absorbing atom [Tho+92].

Information about the magnetic moments of some samples was important in this work.

Details about measurements

XMCD measurements on samples described in chapter 4 were carried out at the DEIMOS beamline of the Soleil synchrotron (Saint-Aubin, France).

For this experiment we used a Superconducting coil allowing a maximum field of ±1 Tesla along the beam direction and the spectra were measured at 300K and 4K.

4 Study of domain wall velocities in Pt/Co/Gd trilayers with Dzyaloshinskii-Moriya interaction

In this chapter, we propose to address the DMI strength in asymmetric stacks with measurements of the DW speed driven by the out-of-plane field (H_z) in the presence of an in-plane field (H_x). We compare the DW velocities in symmetric and asymmetric stacks with PMA at the Walker field and through VSM and XMCD measurements, we access the influence of the saturation magnetization on the maximum DW speed.

4.1 Introduction

Domain walls in non-centrosymmetric systems with ultrathin magnetic films can acquire a fixed chirality stabilized by interfacial Dzyaloshinskii-Moriya interaction (DMI) as seen in section 2.3. In particular, in systems with large DMI, DWs can be driven to very large velocities by current pulses via the spin-orbit torque effect [Man+18]. This is why chiral Néel walls are largely studied nowadays.

In this chapter, we address the study of the field-driven dynamics of the chiral Néel walls and show two methods to extract the DMI strength from such measurements.

As described in section 2.2.4, in symmetric ultrathin films with PMA domain walls show low velocities limited by the breakdown occurring at the Walker field (H_w). Studies were carried out to explore the effect of the DMI in asymmetric stacks. In this study, we chose asymmetric thin film systems containing a Pt/Co interface, as this is known to give rise to a strong DMI [Piz+14; Bel+15].

4.2 Methods

4.2.1 Sample preparation

In this chapter, three different magnetic thin stacks were considered. All the samples were grown on Si/SiO_2 substrates by magnetron sputtering at room temperature (see section 3.1.1).

- Pt/Co/Pt: (Fig 4.1 a) was grown in the form of a continuous film.
- Pt/Co/GdOx: (Fig 4.1 b) in this case, the Gd layer was grown in the form of a wedge of variable thickness, obtained by shifting the sample holder by 8° with respect to the target. The Gd layer was oxidized with O_2 plasma for 35 seconds. Because of the variation of Gd thickness along the sample, the degree of oxidation of the Gd layer is increasing going from the thick to the thin Gd side, giving rise to a different degree of oxygen concentration at the Gd/Co interface and within the Co layer. The Co oxidation gradient gives rise to a gradient of PMA along the sample (see Chapter 5) and in this study we considered the sample region close to the optimum oxidation (largest PMA). An Aluminium layer was then deposited on top of the Gd layer, to protect the sample from further oxidation.
- Pt/Co/Gd: (Fig 4.1 c) was grown in the same way as Pt/Co/GdOx sample (Gd wedge) but the Gd layer was not oxidized and was covered with a 6 nm thick Al layer to prevent its oxidation.

For all samples a 4 nm thick Ta buffer was deposited between the substrate and the first layer of Pt to improve the Pt adhesion.

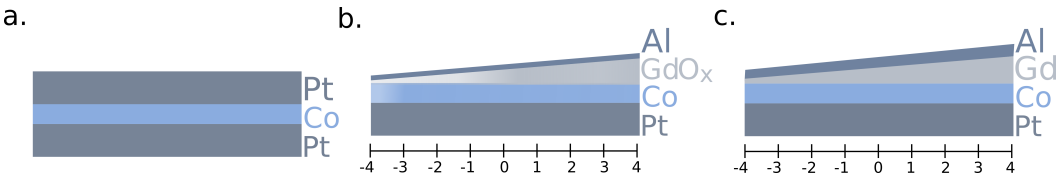

Fig. 4.1: Stacks of **a.**symmetric trilayer Pt/Co/Pt **b.**non-centrosymmetric trilayer Pt/Co/GdOx **c.**non-centrosymmetric trilayer Pt/Co/Gd. In (**b**,**c**) the numbers were marked in order to distinguish the different positions with different Gd thickness.

Samples were grown on 8 cm long substrates; numbers were marked along the stack in order to distinguish the different positions with different Gd thickness. In Figure 4.1, position 0 is the center of the stack; +4 corresponds to +4 cm with respect

to the center of the sample where we have the highest Gd thickness and -4 (-4 cm from the center) the lowest Gd thickness (see Fig. 4.1 b and c).

4.2.2 Structural Characterization

X-ray reflectivity measurements

In order to characterize these samples, X-ray reflectivity (XRR) measurements (section 3.2.1) were carried out to obtain the thicknesses, roughness and density values for each layer.

To facilitate the alignment of the x-ray beam in grazing incidence, the wedge sample was cut in pieces approximately 1 cm long, in different positions of the wedge corresponding to different Gd thickness. This way, we could characterize the approximate change of thickness of the Gd layer along the wedge, as well as the thickness and the roughness of each layer in the different stacks.

The XRR spectra were carried out with the D8 Discover diffractometer at Institut Néel and the fits were done using the Brucker's LEPTOS software. The results are expressed in [nm] for thickness and roughness, and [g/m^3] for the density.

In the first step, the reflectivity measurements and the results of the corresponding fits were used as a means to calibrate the deposition time vs layer thickness; in a second time, some of the layers were also measured in the complete samples to verify the final composition.

Figure 4.2 shows the XRR data with the fit of the Pt/Co/Pt sample. Using this calibration, the sample was prepared in these conditions:

- **Pt/Co/Pt** - Ta (4nm) Pt(4nm) Co(1nm) Pt(4nm)

a.

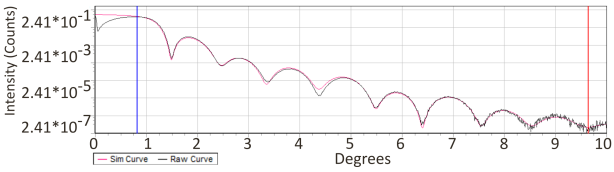

b.

Sample	Thickness	Roughness	Density	Bulk Density
	nm	*nm*	*g/m 3*	*g/m 3*
Pt	3.1	0.33	20.51	21.44
Co	0.7	0.45	8.17	8.9
Pt	4.4	0.44	20.44	21.44
SiO2		0.27		

Fig. 4.2: **a.** XRR data (black curve) and fit (red curve) for Pt/Co/Pt sample **b.** results of the fit the data.

Figure 4.3 shows the XRR data with the fit for Ta/Pt/Co/Gd/Al sample that we used in order to calibrate the deposition time of the different layers. Using this calibration we grew samples having with a good approximation the thicknesses indicated below:

- **Pt/Co/GdOx** - Ta (4nm) Pt(4nm) Co(1nm) GdOx(4nm) Al(2nm);
- **Pt/Co/Gd** - Ta (4nm) Pt(4nm) Co(1nm) Gd(5nm) Al(6nm)

The 6 nm of Al layer on top of the Pt/Co/Gd sample is to prevent the oxidation of the Gd layer.

a.

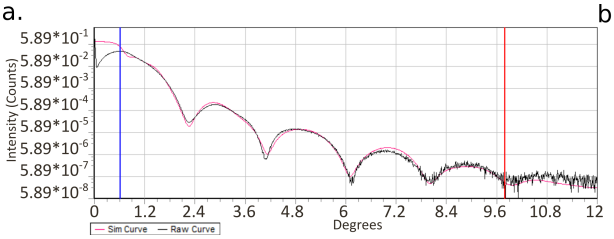

b.

Sample	Thickness	Roughness	Density	Bulk Density
	nm	*nm*	*g/m³*	*g/m³*
Al	6.2	1.69	2.53	2.7
Gd	5.7	0.64	6.04	7.9
Co	1.0	0.3	6.86	8.9
Pt	4.5	0.25	17.93	21.44
Ta	3.6	0.23	14.28	16.67
SiO2		0.13		

Fig. 4.3: **a.** XRR data (black curve) and fit (red curve) for Ta/Pt/Co/Gd/Al sample **b.** results of the fit of the data.

4.2.3 Magnetic Characterization

VSM-SQUID measurements

The magnetic properties of the samples were characterized with VSM-SQUID (section 3.3.2) measurements.

Pieces of $3 \times 3\text{mm}^2$ size were cut along the wedge of the samples in order to measure hysteresis loops and derive the magnetic moment per unit of volume (emu = 10^3A.m^2) as a function of the perpendicular applied field. From these then we can deduce M.t = moment(A/m^2)/surface(m^2) after measuring the exact sample surface.

Figure 4.4 illustrates the moment as a function of the applied perpendicular field observed for Pt/Co/Pt measured at 300K. The hysteresis loop is observed showing 100% remanence indicating the presence of perpendicular magnetic anisotropy.

On the other hand the samples of Pt/Co/GdOx and Pt/Co/Gd were also measured as a function of temperature between 10K and 300K. This allowed us to emphasize the different behavior expected in samples with oxidized and unoxidized Gd layers.

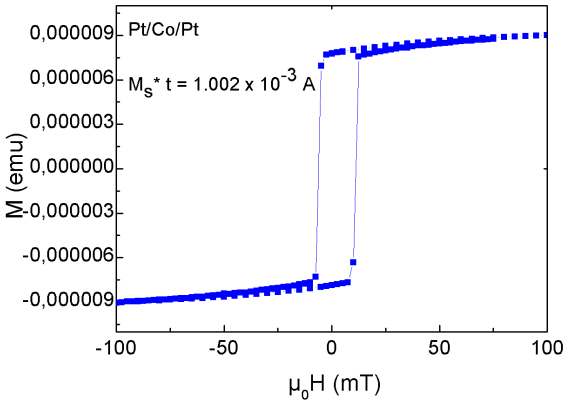

Fig. 4.4: Out-of-plane hysteresis loop measured for Pt/Co/Pt measured with VSM-SQUID.

We observed that for Pt/Co/GdOx (Fig. 4.5), the magnetization changes weakly when going from 300K to 10K. Since for pure Co the magnetization is not expected to decrease at low temperature, we attribute the slight decrease of the magnetization to a very small amount of non-oxidized Gd at the Co/Gd interface. Using the thickness of 1nm for Co, as obtained by XRR, the saturation magnetization at room temperature is $12.6 \times 10^5 \mathrm{A/m}$ which is close to that expected for bulk cobalt.

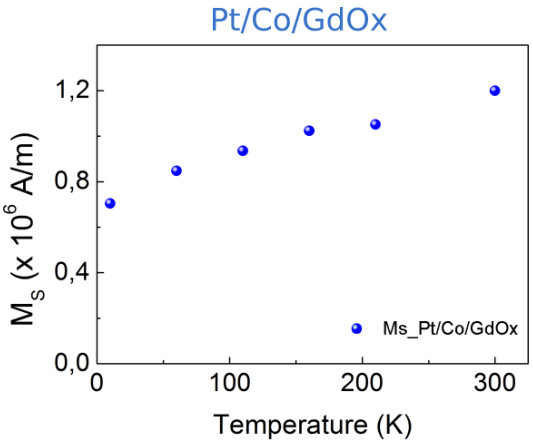

Fig. 4.5: Magnetization vs temperature normalized to a 1 nm thickness, measured by VSM-SQUID for Pt/Co/GdOx sample.

On the other hand, the saturation magnetization of Pt/Co/Gd (see Fig. 4.6a) is much lower at room temperature ($6.4 \times 10^5 \mathrm{A/m}$). This is already a strong indication of the fact that the unoxidized Gd layer contributes to the total magnetization.

For the Pt/Co/Gd (Fig. 4.6) the strong temperature dependence with an increase of the magnetization at low temperature shows the behavior expected for inter metallic systems at the beginning of the rare-earth (RE) series, where the RE and the transition metal (TM) magnetic moments align antiparallel to each other. Since the RE moment decreases with temperature more than the Co moment, this gives rise

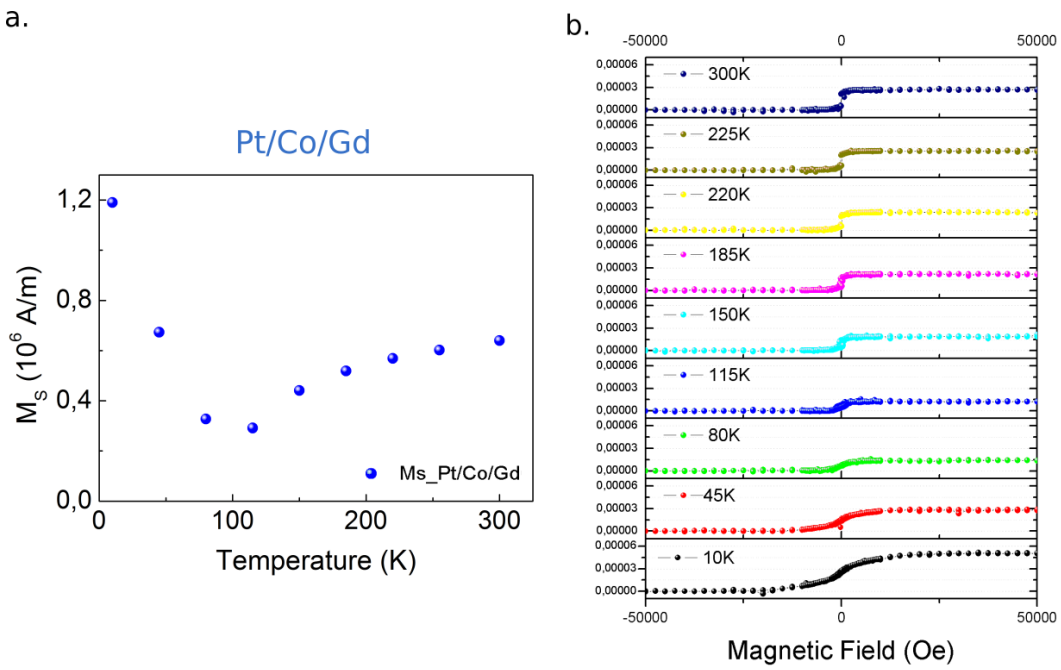

Fig. 4.6: Magnetization vs temperature normalized to a 1 nm thickness, measured by VSM-SQUID for Pt/Co/Gd sample.

to a minimum in the total magnetization (here a 80-100K), called the compensation temperature, where the total Gd and Co moments cancel each other. This behavior confirms that at least some of the Gd layer in contact with Co is unoxidized and carries a magnetic moment. The temperature evolution of the hysteresis loops is shown in the Figure 4.6b. We may notice the effective perpendicular anisotropy to be reduced when the temperature goes down.

The very different values of the magnetization at room temperature in Pt/Co/GdOx ($M_s = 12.6 \times 10^5 A/m$) and Pt/Co/Gd ($M_s = 6.4 \times 10^5 A/m$) is consistent with the fact that Gd layer contributes to the total magnetization when it is not oxidized, while its contribution is negligible in Pt/Co/GdOx, where the Gd has been oxidized.

XMCD measurement

In order to quantify the contribution of Gd to the total magnetization in the Pt/Co/Gd sample we carried out XMCD measurements (section 3.3.3) at Gd $M_{4,5}$ and Co $L_{2,3}$ edges at 300K and 4K under the application of a magnetic field of 1 Tesla.

The measurements were carried out at the DEIMOS beamline at Soleil Synchrotron, with a superconducting magnet and the sample cooling system adopting a liquid He flow cryostat.

The X-Ray Absorption(XAS) and XMCD spectra (see section 3.3.3) measured at Co $L_{2,3}$ and Gd $M_{4,5}$ edges are shown in the Figures 4.7 and 4.8. The XMCD spectra is the difference between the XAS spectra measured with right and left circular polarized light.

We observe that the XMCD signal at the Co L_3 and Gd $M_{4,5}$ edges have opposite sign, indicating opposite directions for the 3d and 4f magnetic moments, as expected. Note that the XMCD signal at the Gd $M_{4,5}$ edge is much larger at a temperature of 4K (Fig. 4.7). This result is coherent with the bigger contribution of Gd moments at low temperature, and also coherent with the results observed by VSM-SQUID.

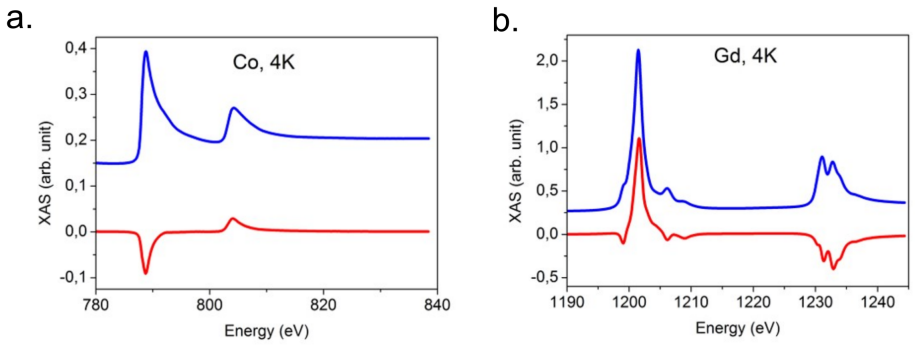

Fig. 4.7: XAS (blue line) and XMCD (red line) measurements of Pt/Co/Gd sample at 4K and in an applied magnetic field of 1T for **a.** Co $L_{2,3}$ edges and **b.** Gd $M_{4,5}$ edges.

It is interesting to note that the Co and Gd XMCD signals have opposite signs at 4K with respect to 300K. This is due to the fact that at RT, above the compensation temperature, the Co moment dominates and in the presence of the applied out-of-plane field the total magnetization is parallel to the Co moments. On the other hand, at 4K the moment of Gd is much stronger than that of Co and dominating at 4K (before the compensation temperature) so that the Gd moments are parallel to the magnetic field.

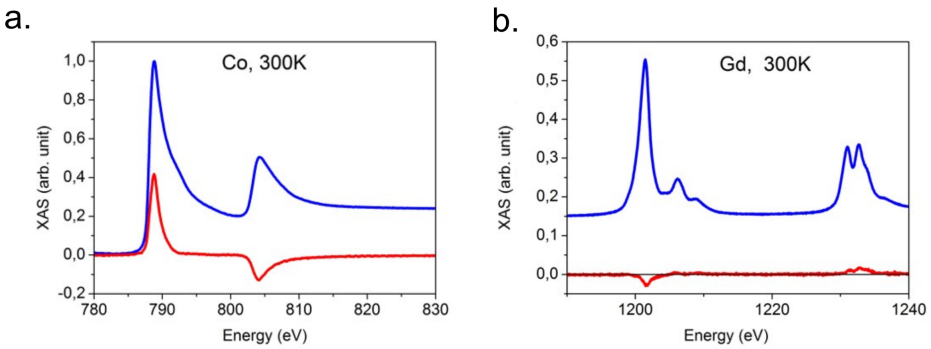

Fig. 4.8: XAS (blue line) and XMCD (red line) measurements of Pt/Co/Gd sample at 300K and in an applied magnetic field of 1T for **a.** Co $L_{2,3}$ edges and **b.** Gd $M_{4,5}$ edges.

If we suppose that the Gd intermixed with the Co at the interface has a moment similar to the one measured by López-Flores *et al.* [LF+13] at 290 K (4.5 μ_B) in

$Gd_{20}Co_{80}$, we can deduce that 10% (0.3 nm) of the Gd layer is magnetic at RT. This is the proportion of Gd atoms that is coupled to Co. In that case, we obtain that the contribution of Gd to the moment per unit surface found by VSM-SQUID (6.4×10^{-4}A) is -4.1×10^{-4}A, while the contribution of Co is 10.5×10^{-4}A. For a Co thickness of 1 nm, this corresponds to $M_{s,t_{Co}} = 10.5 \times 10^{-4}$A, in reasonable agreement with the one obtained from XMCD ($M_s = 14 \times 10^5$A/m) and that of Co found, e.g., in the Pt/Co/GdOx samples.

4.3 Results of domain wall motion

When a domain wall is driven by an easy axis field, it is expected to propagate with the same speed in all directions, if the sample is magnetically homogeneous. In the flow regime, the DW speed depends on the DW width with mobility $m = \gamma_0 \Delta / \alpha$ (Eq. 2.16 - section 2.2.4) and since this is expected to be the same whatever the position in the sample, the propagation will be isotropic.

If on the other hand we managed to modify the domain wall width so that the width of up/down and down/up DWs was different, then the displacement of the two domain walls would be different. In the case of chiral Néel walls (Fig. 4.9a), this can be obtained by applying a field in the direction of the DW magnetization (x-direction). Then the DW width will depend on the DW magnetization direction with respect to the H_x field direction. In systems with DMI which induces chiral Néel walls, an in plane field H_x will not drive the DW motion, but will break the symmetry of the system, modifying differently the DW energy and the internal structure depending if the DW magnetization is parallel (like for down/up DW in Fig. 4.9 b) or anti parallel (like the up/down DW) to the in plane field direction.

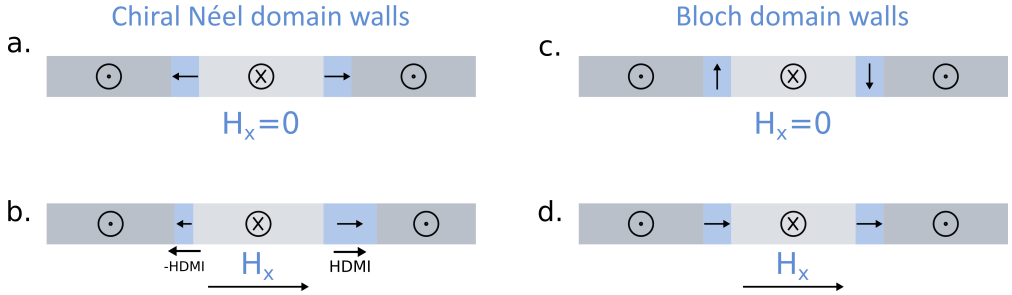

Fig. 4.9: Sketch of the DW magnetization direction (arrow) and width (blue area) for chiral Néel (**a**,**b**) and Bloch domain walls (**c**,**d**) respectively with $H_x = 0$ and an applied in-plane field. In **b** HDMI corresponds the DMI field and the arrow its direction.

This way up/down and down/up DW acquire different width and therefore different speeds: the domain wall expansion will then be anisotropic. On the other hand if the domain walls have Bloch internal structure (chiral or not) (Fig. 4.9b.) the H_x field will simply tilt the magnetization of both up/down and down/up DW towards

the H_x direction (Fig. 4.9d), and the DW width will increase the same way for the two DWs. This method then provides a way to address the presence (or not) of interfacial DMI.

Also, since the DW width will increase when the H_x field is parallel to the DW magnetization, it will allow to access to the chirality of the DW i.e. to the sign of the DMI.

4.3.1 DW speed vs H_x

The DW speeds were measured in the three samples, using wide field magneto-optical Kerr microscopy (section 3.3.1). The domain walls were driven by an out-of-plane field H_z in the presence of the in-plane field H_x in order to visualize the behavior of the DW propagation.

Je *et al.* [Je+13] and Hrabec *et al.* [Hra+14] were the first to extract the sign and the strength of the DMI in non symmetric samples from measurements of the DW motion in the creep regime driven by out-of-plane field in the presence of the in-plane field.

Following the creep law [Met+07; Cha+00], the DW displacement at low magnetic field can be expressed as:

$$v = v_0 \exp[-\alpha(H_z)^{-\mu}] \tag{4.1}$$

where v_0 is characteristic speed, $\mu = 1/4$ is the creep scaling exponent, α is a scaling coefficient which depends on many parameters including μ, k_BT, correlation length of the disorder potential,the saturation magnetization, roughness of the DW segment, the film thickness, the pinning strength of the disorder and the DW energy density per unit area σ_{DW} [Je+13; Hra+14]. Je *et al.* predicted that among these parameters, the sole dependence on the magnetic in-plane field (H_x) is attributed to σ_{DW}, thus the field dependence can be written as:

$$\alpha(H_x) \equiv \alpha(0)[\sigma_{DW}(H_x)/\sigma_{DW}(0)]^{1/4} \tag{4.2}$$

With this relation it is possible to conclude that the variation of the DW energy density plays an important role in the DW speed through the dependence of in-plane field (H_x) [Je+13]. However, Vaňatka *et al.* [Vaň+15] showed that the change of the DW

energy is not the only parameter that determines the speed of DW as a function of the in-plane field, thus the strength of DMI can not be extracted from these conventional measurements. The authors observed that the trend of the curves measured for the same sample in the creep regime and in the flow regime can have different behavior, with the speed curves in the creep regime not consistent with Je *et al.* model. To obtain reliable information about the DMI strength Vaňatka *et al.* [Vaň+15] proposed to bring the DW close to the flow regime propagation where the DW motion is much less influenced by the disorder. Lavrijsen et al. [Lav+15] also observed a discrepancy between the theory described in [Je+13] and the measurements carried out on Pt/Co/Pt trilayers, and called for further developments of the creep theory in the presence of an in-plane field.

For these reasons, we measured the DW speed vs H_x in the flow regime, reducing problems due to pinning by defects.

The procedure to carry out the measurement was the following: first, we saturated the film magnetization in an out-of-plane direction; an opposite magnetic field pulse was then applied to nucleate one or several domains, and finally the DW speed was deduced from the expansion of the initial bubble domain after the application of further magnetic field pulses. To determine the DW speed we divided the DW displacement by the total duration of the field pulses.

In a Kerr microscope, samples with different magnetization direction give rise to different Kerr rotation that are captured as different intensities by the CCD camera. This difference traduces into a magnetic contrast in the Kerr images. At the beginning, the sample is magnetically saturated in such a way, that the magnetization is pointing "up". This state corresponds for example to the dark contrast. In the next step, which is shown in Figure 4.10, using an opposite magnetic field pulse we nucleated domains which corresponds to the white contrast (magnetization pointing "down").

We denominate up/down DW, from the left to right, a DW separating a domain with up magnetization from a domain with down magnetization, and down/up DW the opposite (Fig. 4.10b).

For these measurements the H_z field was produced using a 200μm diameter microcoil associated to a fast current source (see section 3.3.1). The strength of the out-of-plane pulse was chosen to be H_z = 160mT for Pt/Co/Pt, H_z = 88mT for Pt/Co/GdOx and Pt/Co/Gd and the pulse duration was 20ns.

The in-plane field is produced by a water-cooled eletromagnet capable to reach ±300 mT.

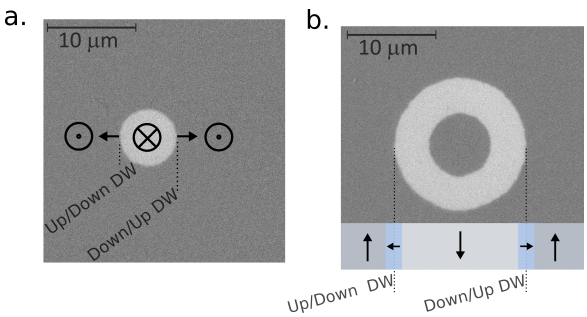

Fig. 4.10: After saturating the film magnetization with a positive out-of-plane field (black contrast) **a.** nucleation of a bubble with the opposite negative magnetic field pulse (white contrast) (sketch of the top view). **b.** Differential image illustrating the DW displacement after the application of positive magnetic field pulse. In the sketch of the side view, the vertical arrows represent the magnetization direction within the domains. The horizontal arrows the magnetization direction at the center of the chiral Néel walls.

Symmetric system

Pt/Co/Pt - Ta (4nm) Pt(4nm) Co(1nm) Pt(4nm)

Figure 4.11 shows the Kerr images corresponding to the expansion of a domain in Pt/Co/Pt without and with the presence of an in-plane magnetic field H_x.

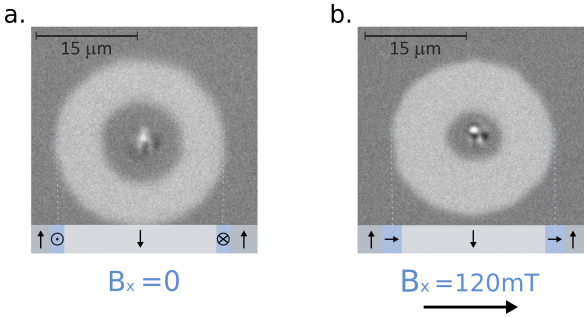

Fig. 4.11: Differential Kerr images showing the expansion of a domain during the application of an out-of-plane field B_z **a.** without and **b.** with the simultaneous application of an in-plane field for Pt/Co/Pt sample.

The images show that in both cases, the DW displacement is isotropic. The domain wall speed of up/down and down/up DW was measured as a function of the H_x field amplitude, for a field up to 200 mT.

As can be seen in Figure 4.12, within the error bars, the same displacement of up/down and down/up DW taken in the direction of the H_x field is observed for every value of H_x. The speed vs H_x field curve for the two DWs are then symmetric with respect to the $H_x = 0$ axis. This type of curve i.e. the isotropic expansion of domains reflects the dynamics of a system with Bloch walls. This is expected for this symmetric system in which the interfacial DMI contributions of Pt/Co and Co/Pt

interfaces have the same magnitude however with different sign, leading to the compensation of the DMI.

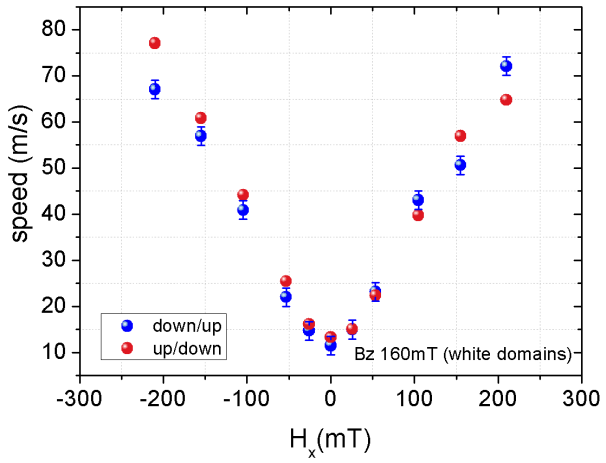

Fig. 4.12: DW speed vs in plane field H_x for the Pt/Co/Pt sample, measured for up/down and down/up DW propagation in ± direction.

Non-centrosymmetric system

Pt/Co/GdOx - Ta (4nm) Pt(4nm) Co(1nm) GdOx(4nm) Al(2nm)
Pt/Co/Gd - Ta (4nm) Pt(4nm) Co(1nm) Gd(5nm) Al(6nm)

Figure 4.13 shows differential Kerr images corresponding to the expansion of a domain wall without H_x and with H_x applied in opposite directions, for the Pt/Co/Gd sample. In the presence of the H_x field, the domain wall propagation is clearly anisotropic in the x direction and the asymmetry changes sign for opposite H_x field direction. This behavior is the fingerprint of the presence of chiral domain walls, as explained above. The sign of the asymmetry also allows us to deduce that the domain walls have left-handed chirality i.e. the magnetic moments turn anticlockwise. For convention, the DMI is negative but we will omit the sign in all the tables. A similar asymmetric expansion is observed for Pt/Co/GdOx.

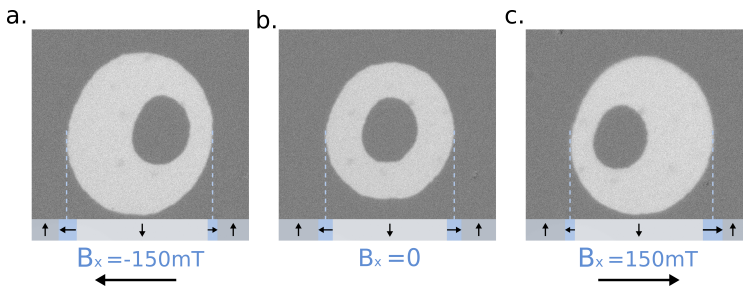

Fig. 4.13: The differential Kerr images represent larger expansion for up/down for B_z = 150mT, larger for down/up for B_z = +150mT. From this, one can deduce the magnetization direction within the two DWs, therefore the left handed chirality.

Figures 4.14 and 4.15 show the speed vs Hx curve measured for Pt/Co/GdOx and Pt/Co/Gd for up/down and down/up domain walls propagating in the x direction (parallel to the in-plane field). The two curves have opposite behavior with respect to $H_x = 0$, meaning that up/down and down/up domain walls have the same behavior with opposite H_x field, which is consistent with the chirality of the DWs.

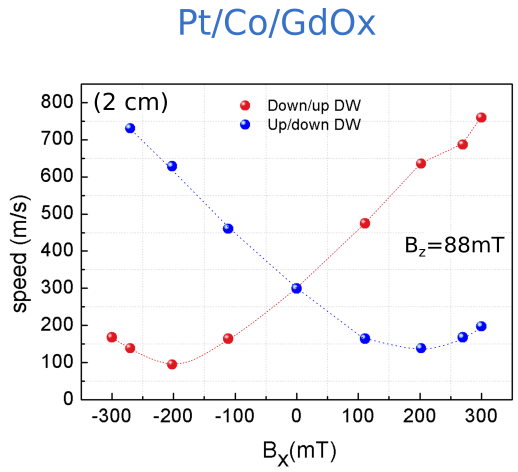

Fig. 4.14: DW speed vs in-plane magnetic field H_x, measured for up/down and down/up DW propagating in ± direction, driven by 20ns long B_z pulses of 88mT in 2cm position.

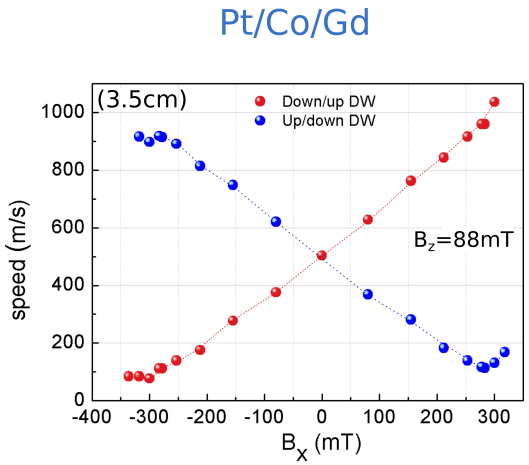

Fig. 4.15: DW speed vs in-plane magnetic field H_x, measured for up/down and down/up DW propagating in ± direction, driven by 20ns long B_z pulses of 88mT in 3.5cm position.

Let us take the down/up DW. For positive H_x fields, parallel to the DW magnetization direction, the DW velocity increases, as the DW width increases. For negative fields, opposite to the DW magnetization, the DW width decreases, so that the velocity decreases. When the negative field is equal and opposite to the DMI field that stabilizes the Néel internal structure, the DW acquires Bloch form and the velocity will reach a minimum. For larger negative fields the DW magnetization switches and aligns with the external field so that the velocity will again increase as the field increases. The field for which the DW velocity is minimum is therefore the field

compensating the H_{DMI} field (which of course is opposite for up/down and down/up DWs). It then provides a way to measure such field.

For Pt/Co/GdOx sample (Fig. 4.14), the minimum is around 200 mT that can be defined as the value for DMI field (H_{DMI}).

In turn, for the Pt/Co/Gd sample (Fig. 4.15), the value for H_{DMI} is around 300 mT, larger than sample Pt/Co/GdOx.

4.3.2 Method to address the DMI by DW speed vs H_x

From the measurement of the speed vs H_x, it is then possible to obtain the values of H_{DMI} for both samples (Pt/Co/Gd and Pt/Co/GdOx).

With these values we can extract the DMI strength from the expression (Eq. 2.22):

$$H_{DMI} = D/(\mu_0 M_s \Delta) \tag{4.3}$$

Using the material parameters obtained from VSM-SQUID (spontaneous magnetization and magnetic anisotropy).

Note however that the determination of the DMI strength is also dependent on the value of the exchange stiffness A, which is a parameter difficult to measure. Table 4.1 shows that using values between 16 pJ/m and 22 pJ/m which are expected for Co thicknesses around 1 nm [Met+07], the DMI value varies by around 20%. The DMI of the two samples were also measured by BLS [Pha+16; Vaň+15] and the values obtained with this method are also reported in Table 4.1. The best agreement with BLS measurements (which only require M_s as a material parameter) is obtained for A = 16 pJ/m, this is why we think that this value is probably closer to the stiffness of our samples.

Also, note that the DMI values obtained for Pt/Co/Gd and Pt/Co/GdOx ($D \sim 1.5$ mJ/m^2) are very similar. Since the two samples have identical bottom Pt/Co interface and varying top Co interface, this result probably indicates that the DMI in these stacks is mainly localized at the Pt/Co interface. More on this subject and on the possible presence of DMI at Gd oxide interfaces is reported in the next chapter.

Since the main drawback of this method is that the extracted DMI strengths depend on the exchange stiffness (A), a material parameter that we could not measure,

our aim was to find another method allowing to obtain the DMI strength using only measurable parameters. This is discussed in the next section.

4.3.3 DW speed vs H_z

One of the consequences of DMI on field driven DW dynamics predicted by theory [Thi+12] is that they become more stable against precession, i.e. the Walker field is pushed to larger out-of-plane fields with respect to the case of Bloch walls in symmetric films. Our first aim here is to verify experimentally the theoretical prediction. We will then show that the value of the velocity at the Walker field provides a way to obtain the value of the DMI strength.

As for the speed vs H_x measurement, the DW speeds were measured on continuous films, using wide field magneto-optical Kerr microscopy (Section 3.3.1). DW speeds were measured as a function of H_z in order to visualize the different regimes of DW propagation.

To carry out the measurement , the in-plane field H_x was set to zero, and the speed was measured from the domain wall propagation induced by out-of-plane magnetic pulses using 200 μm microcoils.

In most cases for these measurements, H_z was varied from zero to 300 mT with a pulse duration of 20 ns. For the small fields, corresponding to the creep regime (section 2.2.4), the number of pulses was adjusted so that the domain wall displacement was reliably measurable.

The DW speed was deduced from the expansion of the initial bubble domain and after the application of further magnetic field pulses. To determine the DW speed we divided the DW displacement during the total number of pulses, by the total duration of the field pulses.

Pt/Co/Pt - Ta (4nm) Pt(4nm) Co(1nm) Pt(4nm)

The DW speed vs H_z was obtained for the Pt/Co/Pt sample and is shown in Figure 4.16. For this centrosymmetric system, the speed changes exponentially with the field up to around to 130mT as expected for the thermally activated regime.

At higher field the velocity increases linearly with the applied field. Note that just one linear regime is observed instead of two regimes expected from the theory (Fig 2.9 - Steady motion and Precessional motion).

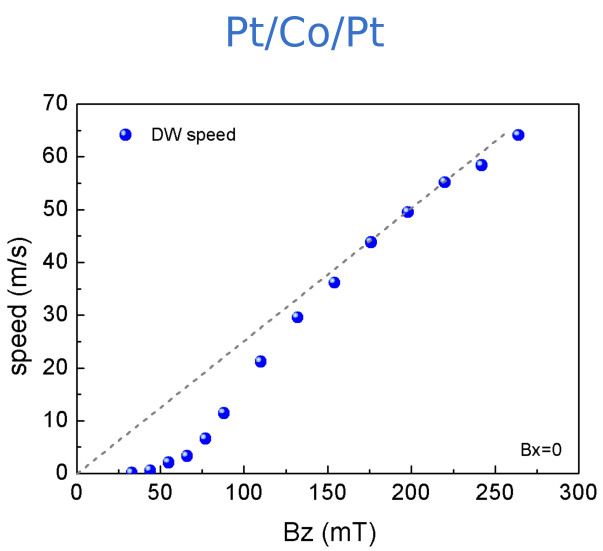

Fig. 4.16: DW speed vs applied magnetic field H_z. The line shows the linear fit to high field for Pt/Co/Pt sample.

To clarify which linear regime is observed, two assumptions were done. Assuming that the linear regime is associated with the steady flow, we used the mobility ($m = \gamma_0 \Delta/\alpha$) in order to fit and we found an irrealistic value of the damping parameter ($\alpha = 4$). On the other hand, if the Walker field is lower than the depinning field and the steady flow is hidden by the creep regime, then only the precessional regime is observed. According to the measured material parameter, the Walker field in this sample ($H_w = \alpha M_s N_{NDW}/2$ where N_{NDW} is the demagnetization factor of a Bloch wall) should be of the order of 12.5 mT and is therefore hidden by the creep regime. Thereby we expect that using the expression of the mobility in the precessional regime ($m = \gamma_0 \Delta/(\alpha + \alpha^{-1})$) gives us more reasonable values. From the fit we obtain a value of the damping parameter ($\alpha \approx 0.4$), that is in good agreement with the values and the behavior shown by Metaxas et.al [Met+07].

In this case, the maximum value for the DW speed is 65 m/s at 260 mT.

Pt/Co/GdOx - Ta (4nm) Pt(4nm) Co(1nm) GdOx(4nm) Al(2nm)

Figure 4.17 presents the result of DW speed vs H_z for the Pt/Co/GdOx sample. In this case, we observe three regimes for DW propagation: at low field, the creep regime is observed as for the Pt/Co/Pt sample. Between 55 mT and 75 mT we can "guess" a linear regime and above this the domain wall velocity saturates.

Note that the velocity above 75 mT is much larger than that observed for the Pt/Co/Pt, as it reaches 350 m/s. The linear regime (seen between 55 mT and 75 mT) points

out to a very large mobility of around 4 m/s/mT, that is about 5 times larger than that observed for the Pt/Co/Pt sample. We attribute therefore this regime to the stationary flow regime.

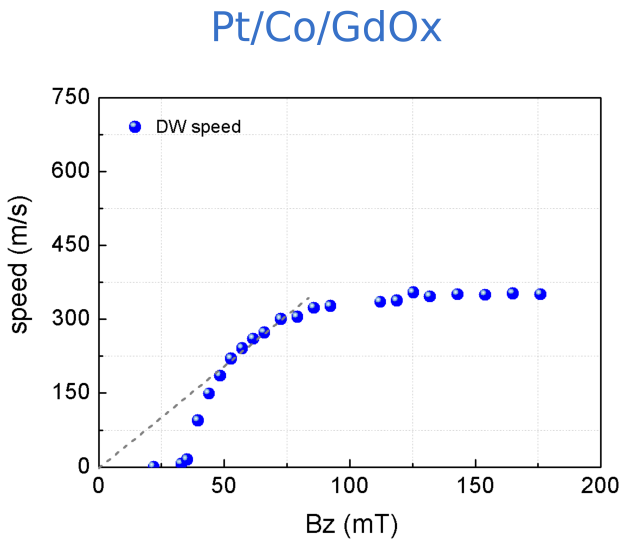

Fig. 4.17: Dw speed vs. H_z field measured for Pt/Co/GdOx sample.

In this regime the DW mobility can be written as $m = \gamma_0 \Delta/\alpha$ where α is the damping parameter, $\Delta = \sqrt{A/K_{eff}}$ with A the stiffness constant and K is the anisotropy energy.

Using the magnetic parameters obtained with VSM-SQUID and the expression above, we obtain a value $\alpha = 0.28$ that is comparable to that found by Miron *et al.* [Mir+11] for a Pt/Co/AlOx sample.

From Thiaville *et al.* [Thi+12] the expression for the Walker field in the presence of the DMI is:

$$H_w = \frac{\pi \alpha H_{DMI}}{2} \tag{4.4}$$

where $H_{DMI} = D/(\mu_0 M_s \Delta)$ (Eq. 2.22). Using the experimental K, A = 16 pJ/m and the α value obtained from the DW mobility, we obtain $H_w^{th} \sim 83$ mT for the theoretical value of the Walker field. This is in good agreement with the experimental value $H_w^{exp} \sim 79$ mT which corresponds to the end of the linear regime, where the speed starts saturating.

With the good agreement between the theoretical and experimental value for the Walker field, we become confident that: i) the DW propagates in the steady flow regime ii) the end of the flow regime is the Walker field and iii) the Walker field is

larger than in Pt/Co/Pt sample because of the presence of the DMI, and this explains the high velocities.

Pt/Co/Gd - Ta (4nm) Pt(4nm) Co(1nm) Gd(5nm) Al(6nm)

Figure 4.18 shows the speed vs H_z measured for the Pt/Co/Gd sample. Here we observe the same three regimes for DW propagation as the Pt/Co/Gd sample. At low field, we observe the creep regime, after that the linear flow regime clearer here than in Pt/Co/GdOx sample and above 116 mT, a saturation regime.

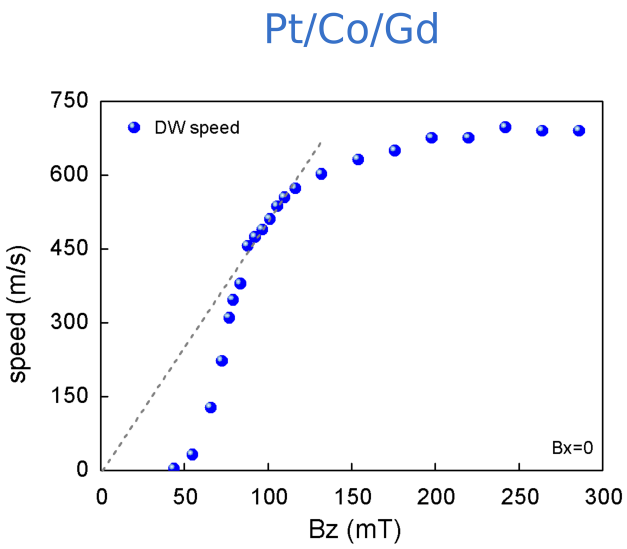

Fig. 4.18: Domain wall speed vs H_z field measured for Pt/Co/Gd sample.

In this sample, the maximum speed is around 690 m/s, much bigger than in the Pt/Co/GdOx sample. We will discuss this later.

In this case, we found $H_w^{th} = 133$ mT for the theoretical Walker field and $H_w^{exp} = 116$ mT for the experimental value for the Walker field.

This gives us again confidence in the fact that the end of the linear regime corresponds approximately to the Walker field. Note that the increase of the speed after H_w might be an artifact due to the presence of a slight H_x component acting on the DW.

DW speed with different values for in-plane field H_x

Figure 4.19 shows the speed vs H_z curves for down/up domain walls, measured for a Pt/Co/Gd sample having similar composition to the Pt/Co/GdOx sample, for different values of the in-plane field H_x.

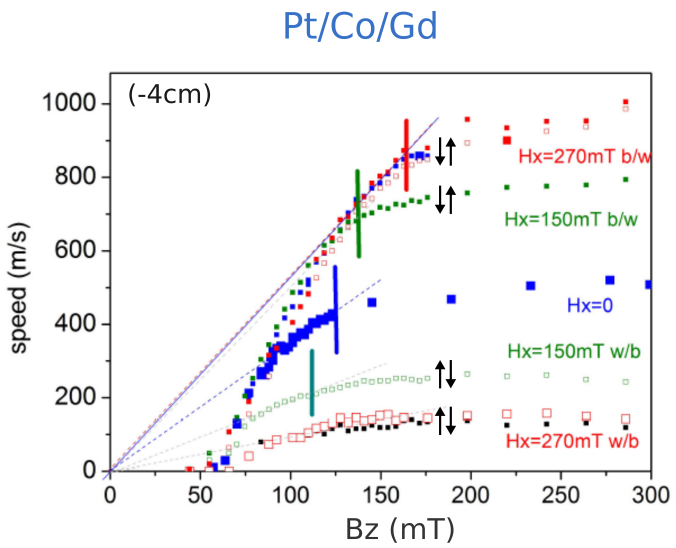

Fig. 4.19: Speed of down/up (↓↑) and up/down (↑↓) DW vs H_z in the Pt/Co/Gd sample in the presence of different fixed in-plane fields H_x.

Each of the curves has a trend similar to that observed for the Pt/Co/GdOx and Pt/Co/Gd samples. They show an exponential regime at low fields, followed by a linear regime and finally a saturation of the DW speed.

For ↓↑ DW the saturation speed increases and decreases for ↑↓ DW: this indicates that the magnetization within the down/up DW is parallel to the positive H_x field, in agreement with what we have already shown in section 4.3.1 where we concluded that the DW chirality is left handed in this sample. We can also observe that the end of the linear regime, corresponding to the Walker field, increases (decreases) as the H_x field increases (decreases). This is expected, as the in-plane field stabilizes (destabilizes) the DW against precession.

Note that the change in the slope of the linear (steady flow) regime is also in agreement with theory ($m = \gamma_0 \Delta / \alpha$). As $H_x > 0$ increases, the DW width increases and the mobility as well. For negative H_x fields, opposite to the DW magnetization, the DW width decreases and the mobility decreases. These curves have therefore all the features predicted by the theory developed by A. Thiaville [Thi+12]. The only remarkable difference with respect to the 1D model is the fact that the speed saturates after the Walker field.

4.3.4 Method to address the DMI by DW speed vs H_z

The main result of the speed vs H_z measurements is that the speed reached for large H_z (around 300 m/s in Pt/Co/GdOx and 600 m/s for Pt/Co/Gd sample) is much larger than for the Pt/Co/Pt sample. This can be explained by the presence of a large

DMI (shown by the speed vs H_x measurements (see section 4.3.1)) that stabilizes the chiral Néel DW magnetization against precession, and pushes the Walker field to larger fields. We have also verified that the end of the stationary flow regime corresponds with the expected Walker field. Another feature of these measurements is that the DW velocity does not drop after the Walker field, as expected from 1D micromagnetic simulations [Thi+12] but that the speed saturates. This is due to the 2D character of the DW and will be briefly discussed later.

We now want to explain why the velocity in Pt/Co/Gd sample is much larger than in Pt/Co/GdOx sample, with (300 m/s) in Pt/Co/GdOx vs (600 m/s) in Pt/Co/Gd.

From Thiaville *et al.* [Thi+12], Pham *et al.* [Pha+16] showed that the analytical expression of the DW velocity at the Walker field, is:

$$v_w = \gamma_0 \frac{\Delta}{\alpha} H_w \approx \frac{\pi}{2} \gamma_0 \Delta H_{DMI} = \frac{\pi}{2} \gamma \frac{D}{M_s} \tag{4.5}$$

In several of our experiments, the steady regime can be hidden by the creep regime. Since the simulations [Yos+16] predict saturation of the velocity after the Walker field, we have used the experimental saturation velocity as the Walker velocity. From this expression, the saturation velocity is expected to increase as M_s decreases. The values for D extracted from the DMI field were 1.58 mJ/m^2 for Pt/Co/GdOx sample and 1.51 mJ/m^2 for Pt/Co/Gd sample (see Table 4.1). Since the DMI strength in Pt/Co/GdOx and Pt/Co/Gd sample is approximately the same, the lower M_s in the Pt/Co/Gd sample can explain the strong increase of the domain wall velocity.

Equation 4.5 also provides a way to obtain the strength of the DMI from the saturation velocity that needs M_s as the only material parameter and is independent of exchange stiffness.

Table 4.1 reports the values of DMI strength using the three methods, i.e.; from the BLS measurements, DMI strength extracted from the DMI field (D_{HDMI}) together with the saturation velocity (D_{vmax}). These results show an excellent agreement (around 10%) between the values obtained with the two methods using DW dynamics. The latter method is interesting as it requires only the measurement of the saturation DW velocity and the saturation magnetization, that are easily measurable. It can also be an interesting method for samples with low magnetic anisotropy, where the application of in-plane fields may promote a large density of nucleation which makes the DW velocity measurement impossible.

We would like to stress here that this method to measure DMI through the saturation velocity has been introduced here for the first time.

Tab. 4.1: Values for Pt/Co/GdOx and Pt/Co/Gd samples of nominal Co thickness (t_{Co}), spontaneous magnetization (M_s), effective anisotropy field ($\mu_0 H_k$), exchange stiffness A (two values from the literature), DMI field ($\mu_0 H_{DMI}$), DMI strength extracted by BLS (*) on a similar sample [Vaň+15], DMI strength extracted from the DMI field (D_{HDMI}) and DMI strength extracted from DW speed at Walker field (D_{vmax}).

Sample	M_s	$\mu_0 H_k$	t_{Co}	A	$\mu_0 H_{DMI}$	v_{max}	D_{BLS}	D_{HDMI}	D_{vmax}
	MA/m	*mT*	*nm*	*pJ/m*	*mT*	*m/s*	*mJ/m²*	*mJ/m²*	*mJ/m²*
Pt/Co/GdOx	1.26	650	1	16	200	320	1.5*	1.58	1.46
				22				1.85	
Pt/Co/Gd	0.64	810	1	16	300	600	1.5*	1.51	1.39
				22				1.77	

4.3.5 Saturation of DW speed at large field

In contrast with the predictions of micromagnetic 1D models (Fig. 2.13), in Pt/Co/GdOx and Pt/Co/Gd the measured DW velocity (Figures 4.17 to 4.19) saturates for large B_z fields. In order to clarify this behavior, in the framework of a collaboration with LPS in Orsay large-scale 2D micromagnetic simulations were carried out using the MuMax3 code [Van+14] with the material parameters and DMI of Pt/Co/GdOx as reported in Table 4.1.

To avoid the effects of the borders and the associated DW tilting we simulated a propagating DW in a moving $1 \times 1 \mu m^2 \times 1$nm box with periodic boundary conditions linking the top and bottom edges. The lateral mesh size was 2nm. Different values of the damping α (0.15 to 0.35) were tested. In addition, perfect and disordered samples were considered (the latter realized with a spatial fluctuation of the uniaxial anisotropy value).

Figure 4.20a shows the results for the perfect system. The DW speed initially increases linearly with field, up to the Walker field, which is proportional to the damping parameter as seen in Equation 2.23. The Walker velocity is independent of damping, as expected from the 1D collective coordinates (q, ϕ) model (see Equation 2.25). Above the Walker field, the speed reaches a plateau with ≈ 300 m/s, in quantitative agreement with the experimental results (Fig. 4.20a). This plateau is a characteristic of the dissipation mechanisms in 2D chiral Néel domain walls in the presence of DMI above the Walker field [Yos+16; Pha+16].

A representative snapshot of the DW structure above the Walker field is shown in Fig. 4.21. The DW presents a complex meander shape and its magnetization rotates several times along the wall. As discussed by Yoshimura *et al.* [Yos+16], pairs

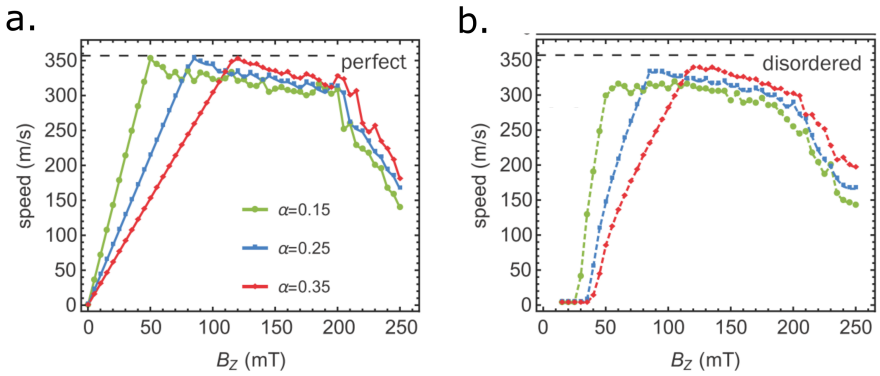

Fig. 4.20: Simulated DW dynamics with the Pt/Co/GdOx: A = 16 pJ/m, M_s = 1.26 MA/m, D = 1.5 mJ.m^{-2}, K_u = 1.44 MJ.m^{-3}. **a.** perfect sample **b.** disordered sample.

of Bloch lines (marked with large arrows in the magnified view) are continuously nucleated in the DW. These lines, with their Néel-like orientation, can have two very different widths, depending on whether they rotate in the sense favored by DMI or not.

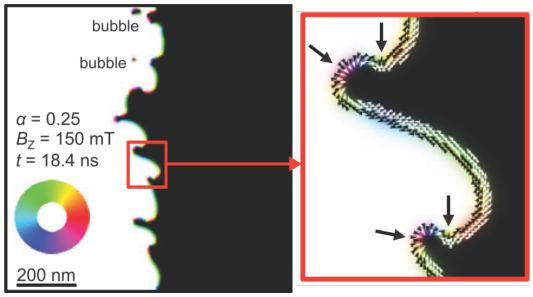

Fig. 4.21: In the magnetization snapshot white/ black corresponds to the perpendicular magnetization component and the colors to the in-plane component. Large arrows indicate the Bloch lines.

The DW sections containing such lines are slower, hence the meandering DW shape. The lines disappear either by collapse of winding pairs with emission of spin waves (like in Yoshimura), or by the creation of bubble domains (visible in the Figure 4.21) that detach by pinching off the wall meanders, and eventually collapse. When the bubbles contain Bloch lines, these annihilate and transform the bubbles into skyrmions with structure stabilized by DMI, before the skyrmions themselves collapse. The creation of bubbles is a second dissipation mechanism that was not seen in the calculations by Yoshimura *et al.* [Yos+16], as the DMI considered in that work was relatively small with respect to the value considered here. The reduced DW energy in the case considered here favors the meandering of the DW and the subsequent creation of bubbles. Altogether, the DW structure is on the average that of a chiral Bloch wall. Indeed, with dominant DMI, this is the DW structure just before the Walker breakdown [Thi+12].

In the case with disorder, the effects are qualitatively the same, as seen in fig 4.20b. As expected, the disorder induces a non-zero propagation field, but does not change the Walker field nor the maximum velocity. The shape of the DW and the energy dissipation mechanism (collapse of Bloch line pairs and creation of detached bubbles) are also not significantly affected. At fields beyond the experiment range (about 200 mT), the simulations reveal that the plateau ends and the DW velocity decreases. This indicates that the dissipation mechanisms can no longer sustain a constant velocity.

4.4 Summary

In this chapter, we have reported the study of domain wall dynamics of three samples. The symmetric sample Pt/Co/Pt shows the dynamics expected for samples with Bloch domain walls, and DWs exhibit relatively weak velocities at high fields. The dynamics of Pt/Co/GdOx and Pt/Co/Gd non symmetric samples is very different. The propagation of domain walls becomes asymmetric when DWs are driven by an H_z field in the presence of an in-plane field. Also, the DWs reach much larger velocities for high fields. This behavior is consistent with the presence in these samples of interfacial DMI that stabilizes chiral Néel walls. We have shown two methods to extract the DMI strength from domain wall dynamics. The first method has been first introduced by Je *et al.* [Je+13] and Hrabec [Hra+14] and applied to DW dynamics driven by weak field, in the creep. Our originality has been to apply this method for DW dynamics in the flow regime, that the Néel group has shown to be more reliable than the measurements in the creep regime [Vaň+15]. This has been possible thanks to use of microcoils and fast current pulse generators developed in collaboration with M. Bonfim from Federal University of Paraná -Brazil. The method based on the measurement of the saturation velocity has been introduced here for the first time. Besides being an interesting method based on the knowledge on measured parameters, it has allowed us to show that the DW velocity can be easily tuned by changing the magnetic moment of the FM layer.

The results presented in this chapter have been published in:

Thai Ha Pham, J. Vogel, J. Sampaio, M. Vaňatka, J.-C. Rojas-Sánchez, M. Bonfim, D. S. Chaves, F. Choueikani, P. Ohresser, E. Otero, A. Thiaville and S. Pizzini. “Very large domain wall velocities in Pt/Co/GdOx and Pt/Co/Gd trilayers with Dzyaloshinskii-Moriya interaction”. In: EPL (Europhysics Letters) 113.6 (2016), p. 67001.

5

Dependence of Dzyaloshinskii-Moriya interaction on the oxygen coverage in Pt/Co/MOx trilayers

In this chapter, we propose to study the interfacial DMI in a series of Pt/Co/MOx (M = Al, Gd) trilayers where the degree the oxidation of the cobalt (Co) layer is varied. We compare the effective DMI strength in Pt/Co/MOx with a different degree of oxidation of the Co/MOx interface, and we study which contribution the Co/MOx interface gives to the total DMI.

5.1 Introduction

As already seen in the previous chapters, the interfacial DMI at ultrathin ferromagnetic (FM) layers with PMA in contact with a heavy metal (HM) with large spin-orbit coupling (SOC) may lead to the stabilization of chiral magnetic textures such as chiral Néel walls. The DMI can stabilize the DW structure against precession, which allows the DW to be driven to large speed by magnetic field.

Among the many systems with DMI, Pt/Co interface is the most studied, following the work of Miron *et al.* [Mir+11] that found very large current-driven domain wall speed in Pt/Co/AlOx trilayers. Recent *ab initio* calculations have predicted that by varying the oxygen coverage of the Fe layer in Ir/Fe/O trilayers the sign and the strength of the DMI can be tuned [Bel+16]. Similar results were predicted for the Co/O interface, like Pt/Co/MgO [Yan+15] or Pt/Co/graphene trilayers [Yan+17] where a strong DMI contribution was predicted at the top Co interface.

Manchon *et al.* [Man+08] in turn investigated the role of Co oxidation in the PMA of Co/AlOx interface in a series of Pt/Co/AlOx trilayers. By controlling the oxidation playing on the different oxidation time of the oxygen plasma in several Pt/Co/AlOx samples, the authors noticed, using X-ray photoelectron spectroscopy (XPS) measurements (Fig. 5.1b) and by hysteresis loops obtained by extraordinary Hall effect (EHE) (Fig.5.1a) that varying the degree of oxidation modifies the magnetic prop-

erties of the Co layer, inducing a magnetic anisotropy crossover from in-plane to out-of-plane.

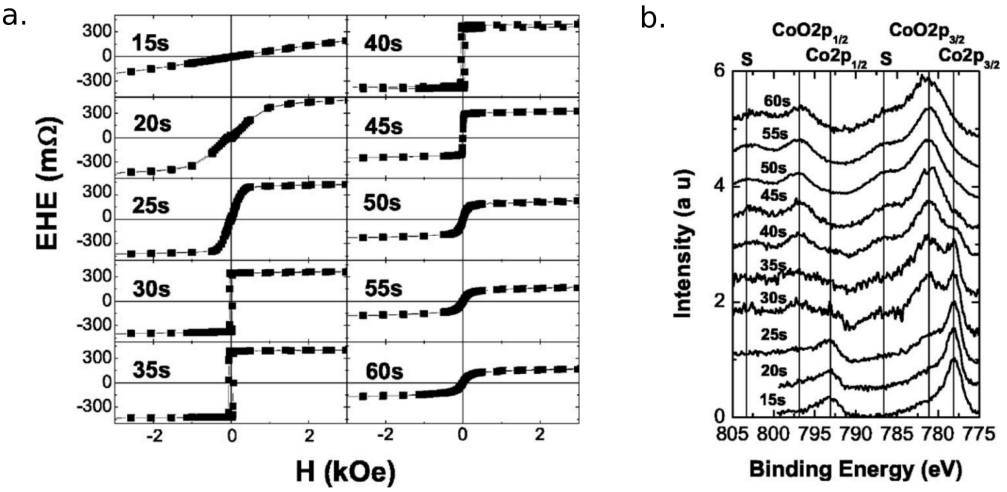

Fig. 5.1: **a.** Hall effect cycles (EHE) as a function of the applied field for Pt/Co(0.6nm)/AlOx after oxidation with different exposure times **b.** X-ray photoelectron spectroscopy (XPS) of Co 2p edges in Pt/Co/AlOx for various plasma oxidation times from 15 to 60s. Image from [Man+08].

For short oxidation times (up to 25sec, in the Fig.5.1), only part of the Al layer is oxidized and the magnetization of the sample is in-plane, and the XPS spectra show mainly pure Co peaks. For long oxidation times (larger than 50sec), the penetration of oxygen atoms into the Co layer induces a multi-domain structure with perpendicular magnetization in good agreement with the XPS measurement. These show that the pure Co peaks completely vanish, indicating that (at least) the first Co monolayer is totally oxidized, since the XPS measurement are surface sensitive with a penetration depth of the order of 5 – 6 Å in Co. Finally, for intermediate oxidation times (30sec to 45sec), an important amount of oxygen atoms have reached the Co/Al interface, a strong PMA is observed with hysteresis loops with full remanence and the XPS spectra show both Co and CoO features. From this, it was concluded that there is the optimum degree of oxidation where the density of the Co-O bonds is optimal to induce a strong PMA.

In this chapter, we report the study of interfacial DMI in a series of Pt/Co/MOx (M= Al and Gd) samples in which the degree of oxidation of the top Co layer is varied. In order to access to reliable values of the DMI strength, we used the two methods with Kerr measurements to address the DMI, as shown in the last chapter, and we show how the effective DMI strength in these stacks can be related to the magnetic anisotropy energy.

5.2 Methods

5.2.1 Sample preparation

All the samples were grown on Si/SiO_2 substrates by magnetron sputtering at room temperature (seen section 3.1.1).

The samples described in this chapter are composed of a heavy metal, in this case platinum (Pt), over which were deposited an ultrathin ferromagnetic layer, in our case cobalt (Co) followed by an oxide layer (MOx with M=Al,Gd).

After the deposition of Pt and Co, the Al and Gd layers are deposited in the form of a wedge of variable thickness, obtained by shifting the sample holder 8° with respect to the target, and then oxidized by oxygen (O_2) plasma.

We then obtained a sample of the wedge type having an oxidation gradient at the top layer where the degree the oxidation increases going from the thick to the thin (Al and Gd) side. Thanks to this thickness gradient of the MOx layer we have the possibility to control the degree of oxidation that eventually takes place in the Co layer.

For all the samples, a 4nm thick Ta buffer was deposited between the substrate and the first layer of Pt to improve the Pt adhesion.

- Pt/Co/AlOx : Ta/Pt/Co/AlOx/Pt (Fig. 5.2 a) - A capping layer of Pt was deposited on top of these layers to prevent them from further oxidation.

- Pt/Co/GdOx : Ta/Pt/Co/GdOx/Al (Fig. 5.2 b) - An Al layer was deposited on top of the Gd layer, to prevent the sample uncontrolled oxidation.

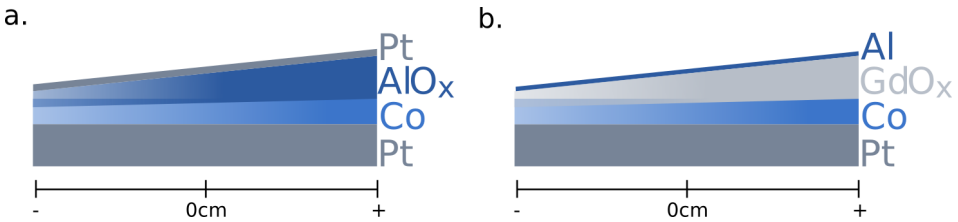

Fig. 5.2: Stacks of **a.** asymmetric trilayer Pt/Co/AlOx **b.** trilayer Pt/Co/GdOx.

Samples were grown on a 8cm long substrate; numbers were marked along the stack to distinguish the different positions with different Al and Gd thickness along the wedge. We have arbitrarily designed the position 0cm around the center of the sample.

5.2.2 Structural Characterization

XRR measurement

To characterize these samples, X-ray reflectivity measurements (section 3.2.1) were carried out to obtain the thicknesses, roughness and density values for each layer.

In the last chapter, we described the procedure that we used to measure the samples (see section 4.2.2). The XRR spectra were carried out with the D8 Discover diffractometer at Institut Néel and the fits were done using the Brucker's LEPTOS software.

Figure 5.3 shows the XRR data measurement for the Pt/Co/AlOx sample in the position 0cm together with the fit. The results of the fit are shown in the Table (Fig. 5.3b).

a.

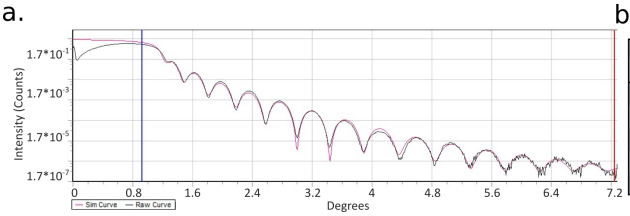

b.

Sample	Thickness	Roughness	Density	Bulk Density
	nm	*nm*	*g/m³*	*g/m³*
Al_2O_3	3.0	1.27	3.56	3.98
Co	0.9	0.33	7.32	8.9
Pt	17.1	0.48	20.49	21.44
Ta	1.7	0.94	16.62	16.67
SiO2		0.47		

Fig. 5.3: **a.** XRR data (black curve) with fit (red curve) using Brucker's LEPTOS software **b.** Table showing the parameters found with the fit in a. for Pt/Co/AlOx sample in 0cm.

The XRR reflectivity data could be fitted by considering only a 0.9nm unoxidized Co layer (see the Table in Fig.5.3b).

On the other hand, for position -2cm (where the Al layer is thinner) the XRR data was more difficult to fit considering only an unoxidized Co layer. Figure 5.4 shows the results of 3 different fits, in which we considered either a 0.7nm thick Co layer only, or a Co (0.6nm) and a CoO (0.2 or 0.3nm) layer. The quality of the fit is very similar, but the high theta values are better reproduced when a small CoO layer is included. Our conclusion is then that in this position of the wedge sample, the Co layer is slightly oxidized: the Co layer thickness reduces to around 0.6-0.7nm, and the oxide layer is around 0.2-0.3nm. This oxide thickness is of the same order of magnitude of the interface roughness, so that its measurement is subject to a large error bar.

Calibrations were also done for Pt/Co/GdOx sample in different wedge positions. Figure 5.5 shows the data, fit and values for wedge position 0cm where the Co layer is not oxidized.

a.

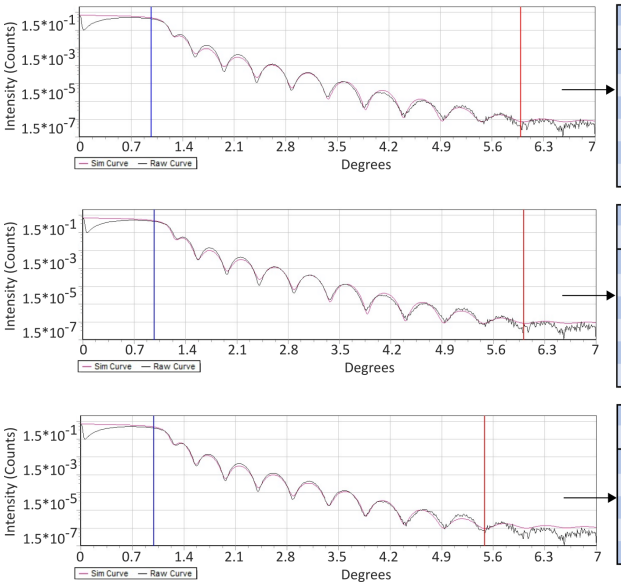

b.

Sample	Thickness	Roughness	Density	Bulk Density
	nm	*nm*	*g/m³*	*g/m³*
Al_2O_3	2.0	1.08	3.78	3.98
CoO	0.2	0.37	5.19	6.44
Co	0.6	0.28	8.69	8.9
Pt	14.2	0.39	20.87	21.44
Ta	2.1	1.45	15.17	16.67
SiO2		0.50		

Sample	Thickness	Roughness	Density	Bulk Density
	nm	*nm*	*g/m³*	*g/m³*
Al_2O_3	2.2	0.9	3.31	3.98
CoO	0.3	0.33	5.64	6.44
Co	0.6	0.23	8.60	8.9
Pt	14.5	0.38	20.56	21.44
Ta	1.8	1.08	16.66	16.67
SiO2		0.53		

Sample	Thickness	Roughness	Density	Bulk Density
	nm	*nm*	*g/m³*	*g/m³*
Al_2O_3	1.7	0.97	3.11	3.98
Co	0.7	0.32	8.63	8.9
Pt	15.0	0.36	20.40	21.44
Ta	1.3	0.93	16.35	16.67
SiO2		0.56		

Fig. 5.4: **a.** XRR data (black curve) with fit (red curve) using Brucker's LEPTOS software **b.** Table showing the values found with the fit in a. for Pt/Co/AlOx sample in -2cm.

Note that the main period of the Kiessig fringes in the two curves (e.g. Fig. 5.3 and 5.4) comes from the Pt layer. As the Pt layer is much thicker in Pt/Co/AlOx, the period is much shorter.

a.

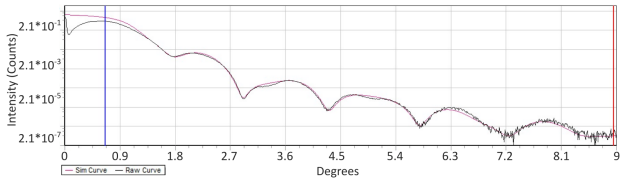

b.

Sample	Thickness	Roughness	Density	Bulk Density
	nm	*nm*	*g/m³*	*g/m³*
Al_2O_3	1.0	0.36	3.24	3.95
Gd_2O_3	0.6	0.36	5.76	7.41
Gd	2.0	0.32	6.38	7.9
Co	0.7	0.31	7.47	8.9
Pt	3.0	0.34	20.96	21.44
Ta	3.2	0.40	15.06	16.67
SiO2		0.27		

Fig. 5.5: **a.** XRR data (black curve) with fit (red curve) using Brucker's LEPTOS software **b.** Table showing the values found with the fit in a. for Pt/Co/GdOx sample in 0cm.

Also note that, in this position, only a small part (0.6nm) of the Gd layer is oxidized, not reaching the Co layer. On the other hand, the measurement in Figure 5.6 shows that in position -3cm most of the Gd layer is oxidized and we observe a thin Co oxide layer on the top of the Co layer.

Analyzing these results in different positions for both samples we then concluded that for thinner (Al and Gd) layer we need to consider the contribution of a thin oxide layer.

The results of the fits were also used as a means the calibrate the deposition time vs. layer thickness; thus we used these calibrations (extrapolating with linear or polynomial fits in some cases) to prepare three samples:

a.

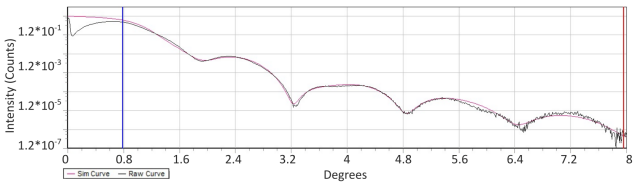

b.

Sample	Thickness	Roughness	Density	Bulk Density
	nm	*nm*	*g/m³*	*g/m³*
Al_2O_3	0.7	0.47	3.48	3.95
Gd_2O_3	1.6	0.37	6.34	7.41
Gd	0.8	0.27	6.56	7.9
CoO	0.2	0.41	6.38	6.44
Co	0.4	0.21	8.49	8.9
Pt	2.7	0.29	21.37	21.44
Ta	2.8	0.40	14.62	16.67
SiO2		0.24		

Fig. 5.6: **a.** XRR data with fit using Brucker's LEPTOS software **b.** table showing the values found with the fit in a. for Pt/Co/GdOx sample in -3cm.

- **Pt(15)/Co/AlOx** - Ta (4nm) Pt(15nm) Co(0.8nm) AlOx (1.5nm - 3nm) Pt(2nm);
- **Pt(4)/Co/AlOx** - Ta (4nm) Pt(4nm) Co(0.8nm) AlOx (1.5nm - 3nm) Pt(2nm);
- **Pt/Co/GdOx** - Ta (4nm) Pt(3nm) Co(0.8nm) GdOx (1.5nm - 3nm) Al(1nm).

5.2.3 Magnetic Characterization

Kerr microscopy measurements

To get access to the variation of magnetic properties of the samples, we measured the hysteresis loops at room temperature by polar Kerr microscopy.

First, a perpendicular field was applied to the surface of the sample to have access to the variation of the perpendicular component of the sample magnetization (M_z) along the sample wedge. This allowed us to characterize in a quick way the magnetic properties in the different positions of the sample. It is important to remind that for our applications, we are only interested in samples with PMA.

The Pt/Co/AlOx and Pt/Co/GdOx samples were measured in different positions along the wedge corresponding to the different oxidation conditions. Different magnetic behaviors were observed depending on the sample position.

Near the edge, on the thick Al and Gd side, that can be considered under-oxidized, in the Al or Gd layers the oxygen atoms have not reached the Co/Al or Co/Gd interface, or they have in an inhomogeneous way, so that the oxygen-induced PMA is not sufficient to overcome the in-plane shape anisotropy. The magnetization lies in the plane of the layers. For the opposite sample side, the oxygen penetrates into the Co layer, which reduces the exchange coupling between the Co. The magnetization of the Co layer lies out-of-plane, but in the case of largest oxidation, the magnetic signal disappears.

From this, our studies were carried out only within the region where the magnetization was out-of-plane.

Figure 5.7a shows the hysteresis cycles for the sample Pt(15)/Co/AlOx in the different positions along the wedge, and in the Fig. 5.7b we can follow the coercive field of this sample in the same conditions.

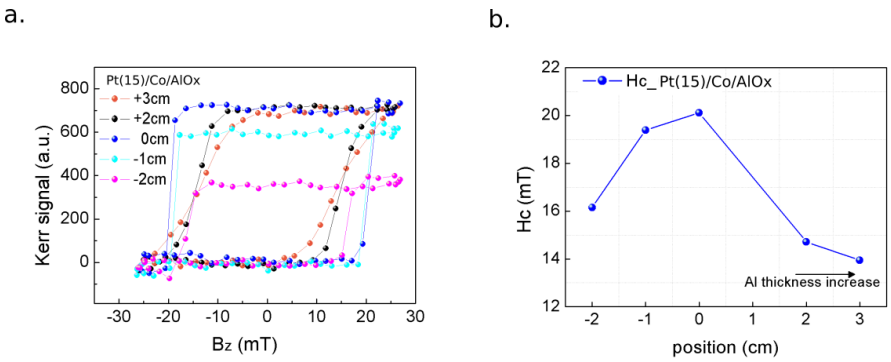

Fig. 5.7: **a.** Hysteresis loops measured by magneto-optical Kerr effect in different positions of the sample Pt(15)/Co/AlOx wedge **b.** curve of coercive field of the same sample vs. position.

We observed that the loops in the center of the sample (0cm and -1cm) are square with 100% remanence showing strong PMA. On either parts of the sample, the cycles become more slanted and the coercivity decreases, indicating a decrease of the anisotropy.

The density of reversed domains increases at the two sides of the sample; on the thick Al side, this is due to the decrease of anisotropy; on the thin side, this is also due to the inhomogeneous CoO/AlOx interface.

For the Pt(4)/Co/AlOx shown in Figure 5.8 which was oxidized in the same way, we observed square hysteresis loops in most of the sample positions, indicating a stronger PMA. In positions +2cm and +2.5cm, we observed the transition from perpendicular to the in-plane easy-axis as the Al layer is little oxidized. The shape of the hysteresis cycles is typical of a system with weak anisotropy in a demagnetized (stripe domain) state.

Also, we measured the hysteresis loops for Pt/Co/GdOx in different positions along the wedge and the coercive field are shown in Figure 5.9.

The results shown for Pt/Co/GdOx are in good agreement with the results shown for the two Pt/Co/AlOx samples. The coercivity decreases at the edges of the sample (lower PMA) and the Kerr signal decrease when going towards thinner (Al or Gd)

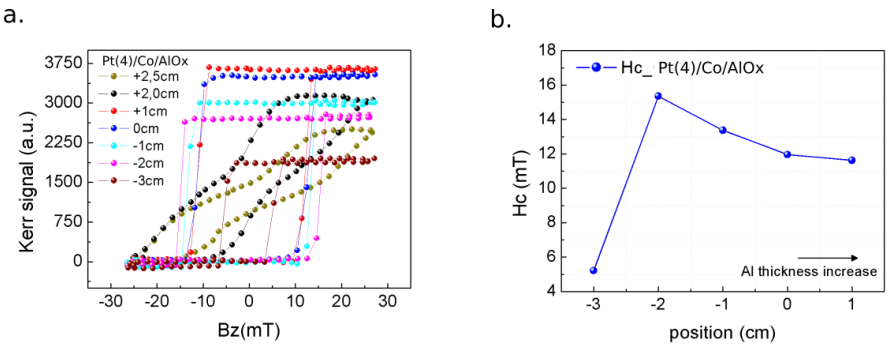

Fig. 5.8: **a.** Hysteresis loops measured by magneto-optical Kerr effect in different positions of the Pt(4)/Co/AlOx wedge **b.** curve of coercive field of the same sample.

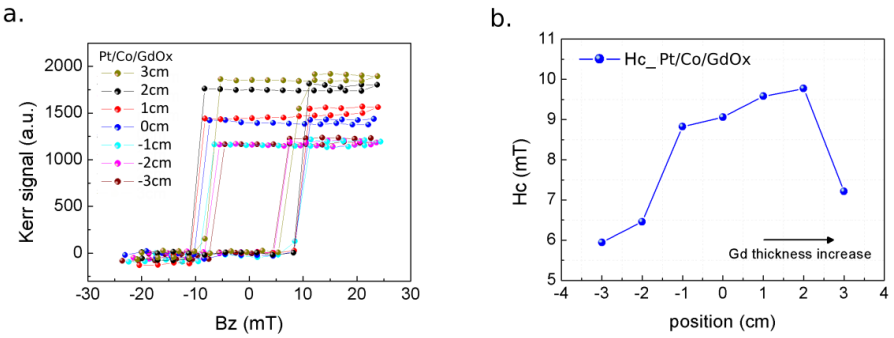

Fig. 5.9: **a.** Hysteresis loops measured by magneto-optical Kerr effect in different positions of the sample Pt/Co/GdOx wedge **b.** curve of coercive field of the same sample.

layers, as the Co layer becomes more oxidized. This is also in agreement with the results found by XRR.

VSM-SQUID measuments

Measurements of saturation magnetization M_s in different positions along the wedge were carried out in these samples by VSM-SQUID.

Since the thickness of the Co layer cannot be determined precisely because of its oxidation, here we report the values of the unit surface magnetization M_st, which can be directly obtained by the VSM-SQUID measurements.

The unit surface magnetization is measured for $\approx 3 \times 3\text{mm}^2$ samples, as a function of magnetic field applied perpendicular to the surface of the sample.

The magnetization was also measured as a function of hard axis (in-plane) magnetic field, to extract the in-plane saturation field and therefore the effective magnetic anisotropy.

Figures 5.10 and 5.11 show the dependence on the $M_s t$ as a function the sample position. For all the samples, we observed that the unit surface magnetization is larger on the thick MOx layer side and decreases going towards thinner (AlOx and GdOx) side. This is in agreement with the results of the hysteresis loops measured by MOKE: since the Co layer becomes oxidized on the thinner side first transforming Co-M-O bonds at the top interface into Co-O bonds, then oxidizing, it is expected that the Co contributes less and less to the total magnetization.

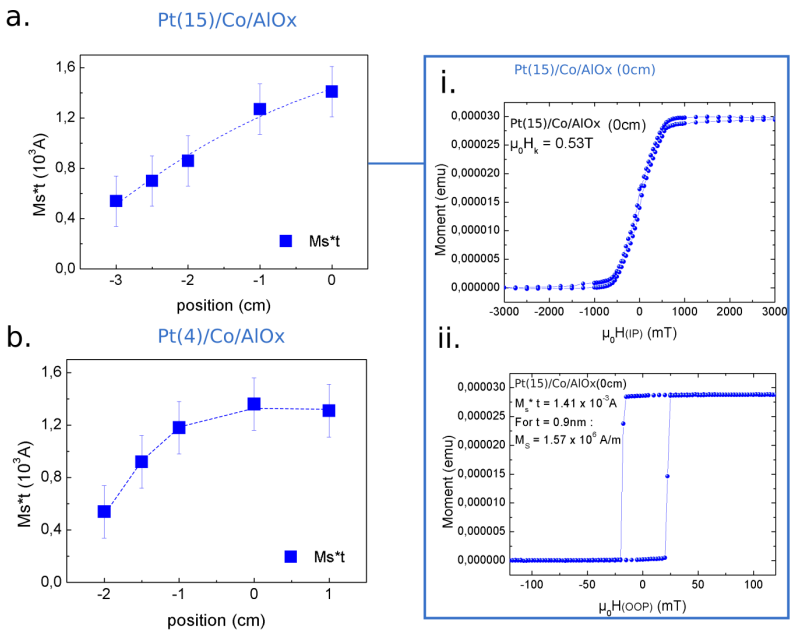

Fig. 5.10: Unit surface magnetization $M_s t$ measured as function different wedge position in **a.** Pt(15)/Co/AlOx **b.** Pt(4)/Co/AlOx. (i) and (ii) shows the hard axis and easy axis hysteresis loops for Pt(15)/Co/AlOx.

The hysteresis loops obtained for Pt(15)/Co/AlOx for both in-plane and perpendicular applied magnetic field are shown in Figure 5.10(i) and (ii). For the in-plane applied field, the magnetization loop for 0cm position, has the typical shape expected for hard axis field. For a perpendicular applied magnetic field (Fig.5.10ii), the corresponding hysteresis loop is square confirming the out-of-plane easy axis.

Knowing M_s in different wedge position of the samples, we can deduce interface magnetic anisotropy K_s that is calculated from $K_s = K_u t$ where $K_u = \frac{1}{2}\mu_0 H_k M_s + \frac{1}{2}\mu_0 M_s^2$.

The main obstacle here is that in order to access to a reliable value of M_s, the precise thickness of the Co layer needs to be known. This is very delicate in our case, especially for the thin Al or Gd sample side. For this we used two approaches: i) we took the extrapolated values of the Co layer thickness found with XRR measurements; ii) we supposed that the magnetization is constant and equal to the bulk Co value and we obtained t_{Co} from the measured $M_s t$. The values obtained using the two

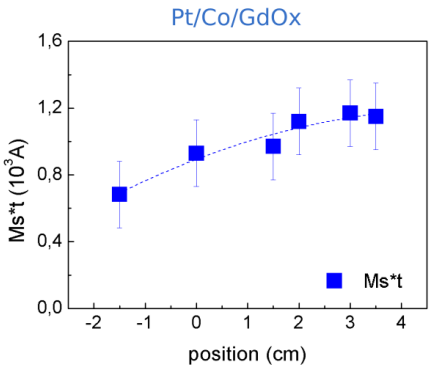

Fig. 5.11: Unit surface magnetization M_st measured for different wedge positions in Pt/Co/GdOx.

methods are shown in Figure 5.12 which shows that the interface PMA depends on the position along the wedge.

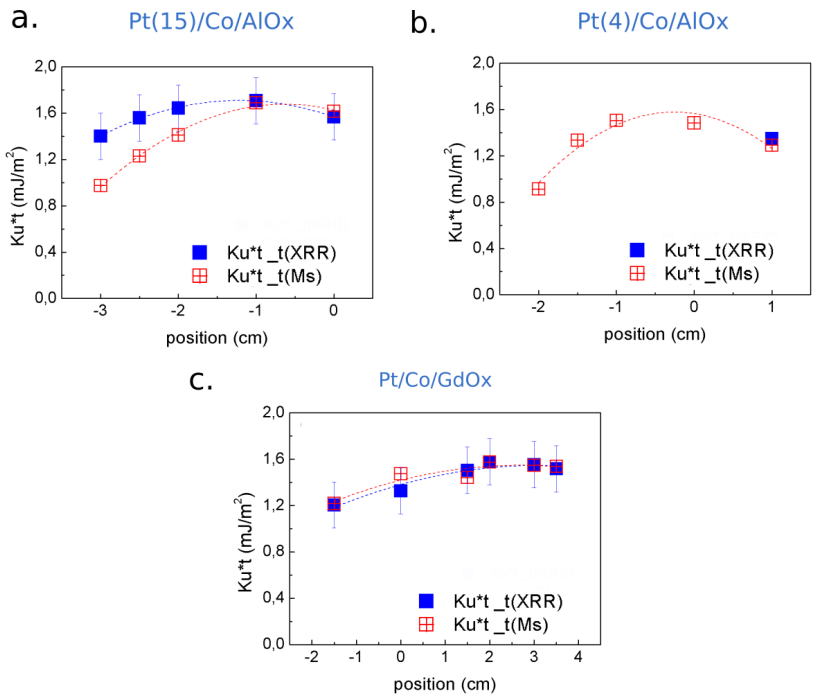

Fig. 5.12: Interface magnetic anisotropy energy K_ut measured as a function of wedge position in **a.** Pt(15)/Co/AlOx **b.** Pt(4)/Co/AlOx **c.** Pt/Co/GdOx; ■: using t_{Co} from XRR measurements; ⊞: using t_{Co} from M_st supposing M_s.

Comparing the M_st (Fig. 5.11 and 5.10) and K_s trends (Fig. 5.12), we can observe that the maximum of K_s is always observed where M_st is maximum or starts decreasing.

5.3 Addressing the DMI

In the previous sections we show that in our samples we always find a region where the hysteresis loops are square and have 100% remanence, indicating the presence of PMA. At the thick Al (Gd) side of the sample the PMA decreases and the magnetization turns in the plane, while at the thin side the hysteresis loops become slanted and the magnetization $M_s t$ decreases (as well as the Kerr contrast) showing the progressive oxidation of the Co layer. For these samples we observe a maximum of the anisotropy (and of the coercive field) which corresponds to the "optimum oxidation" condition, according to Manchon et al [Man+08].

Now, let us study how the interfacial DMI can be related to the anisotropy that we already found.

The *ab initio* calculation by [Bou+16] consider that in Pt/Co/MgO the main contribution to DMI is situated at the Pt/Co interface, but also a significant contribution of DMI is found at the Co/O interface. In the calculations, the DMI has the same sign of the Pt/Co interface, the Co/O layer contribution adding to the total DMI.

In our series of samples with top Al (Gd) layer with variable thickness, the bottom interface (Pt/Co) should have similar characteristics, as the samples were all grown in the same conditions, as shown also by the XRR data. The study of the DMI in the various positions (i.e. different oxidation degree) should therefore give us information on the contribution of the Co/MOx interface to the DMI, since that of the Pt/Co interface is expected to be the same, as long as the Co layer is not too oxidized.

The aim of this work was thus to study the dependence of the effective DMI strength along the wedge position. We have already shown that there are two methods to address the DMI strength based on DW dynamics by wide magneto-optical Kerr microscopy.

As shown before, the first method consists in measuring the DW speed vs in-plane field H_x. From the minimum of the curve we can extract the value of DMI strength from the expression $H_{DMI} = D/(\mu_0 M_s \Delta)$, where $\Delta = \sqrt{A/K_{eff}}$. As we noted in the last chapter, to determine the DMI strength with this method, we need the value of the exchange stiffness (A) which is difficult to measure. In this study, we have used $A = 16$ pJ/m, for which we found the best agreement with the DMI values measured by Brillouin Light Scattering BLS [Pha+16].

Figure 5.13 shows the differential Kerr images corresponding to the expansion of a magnetic domain (down magnetization, white contrast) without in-plane field (middle) and with positive and negative H_x field for Pt(15)/Co/AlOx and Pt/Co/GdOx. While for $H_x = 0$ the DW displacement is isotropic, the displacement becomes anisotropic in the direction of H_x when the in-plane field is applied.

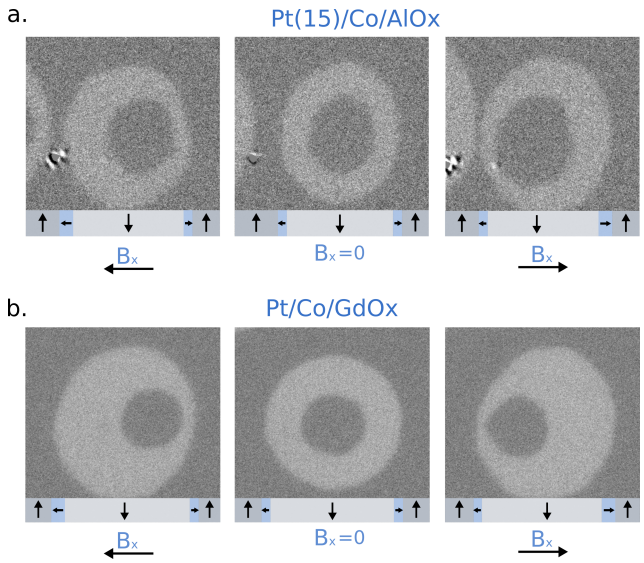

Fig. 5.13: The differential Kerr images representing the expansion of the bubble domain with constant $B_x = -180$mT, 0mT and 180mT for **a.** Pt(15)/Co/AlOx in position -2.5cm driven by $B_z = 300$mT pulses and **b.** Pt/Co/GdOx in position -1.5cm driven by $B_z = 215$mT pulses. In the sketch, the vertical arrows represent the magnetization direction within the domains. The horizontal arrows the magnetization direction at the center of the chiral Néel walls.

The asymmetric expansion, similar for Pt(15)/Co/AlOx and Pt/Co/GdOx is consistent with the presence of left handed domain wall chirality for both samples.

Figure 5.14 shows the speed vs H_x for the three samples. The DMI values extracted from the H_x with minimum speed are shown in Table 5.1 for the different positions of Pt/Co/AlOx and Pt/Co/GdOx samples.

The second method, also applied here, relies on the DW speed as a function of easy-axis field magnitude H_z.

In this case, as we demonstrate in the section 4.3.4, the saturation DW speed can be easily related to the DMI strength via the expression :

$$v_{sat} = \frac{\pi}{2}\gamma\frac{D}{M_s} \tag{5.1}$$

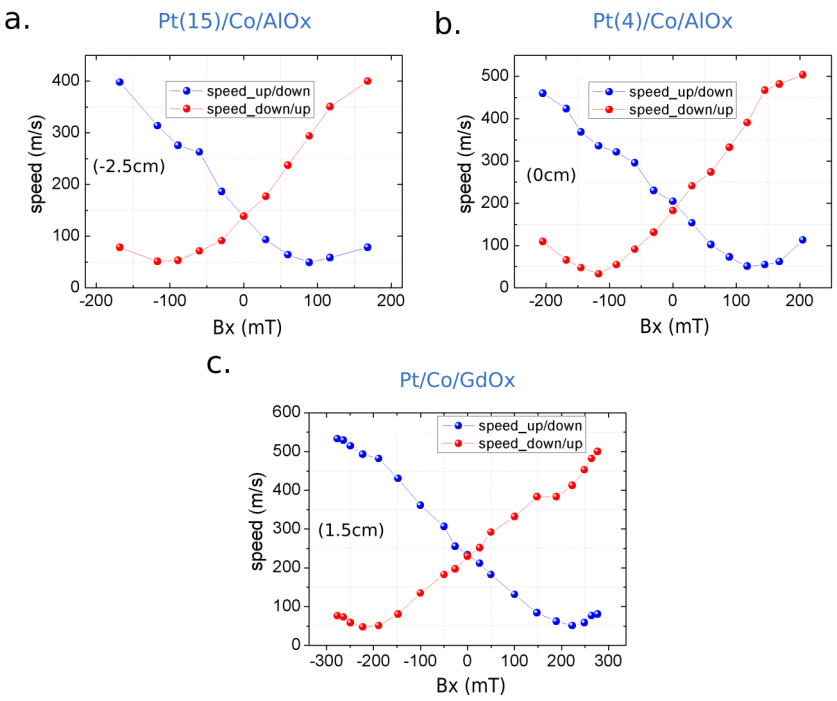

Fig. 5.14: DW speed vs in-plane magnetic field B_x, measured for up/down and down/up DW propagating in $\pm$x direction, driven by 20ns long B_z pulses of 80mT of **a.** and **b.** for the Pt/Co/AlOx samples. **c.** B_z pulses of 120mT for the Pt/Co/GdOx sample.

where the D is DMI strength, M_s the spontaneous magnetization and γ the gyromagnetic ratio.

Analyzing this expression, we observe that the measurements of the saturation of the speed, together with that of the M_s provides a simple and advantageous way to obtain the effective DMI strength in trilayer systems. As we know that the DMI in these layers has an interface origin, we find more appropriate to derive the interfacial DMI strength D_s (in pJ/m) via expression 5.1, thus:

$$D_s = D.t = 2v_{sat}\frac{M_s t}{\pi\gamma} \tag{5.2}$$

where t is the thickness of the ferromagnetic layer, in these cases, the Co layer.

This expression provides a more precise determination of the DMI strength, since $M_s t$ is measured directly by VSM-SQUID instead of M_s which requires a precise calibration of the ultrathin ferromagnetic thickness t which is particularly difficult to obtain for the part of the sample where the Co starts oxidizing.

In order to apply this method to address the DMI strength, we measured the speed vs H_z for all samples (Fig. 5.15) in different wedge positions.

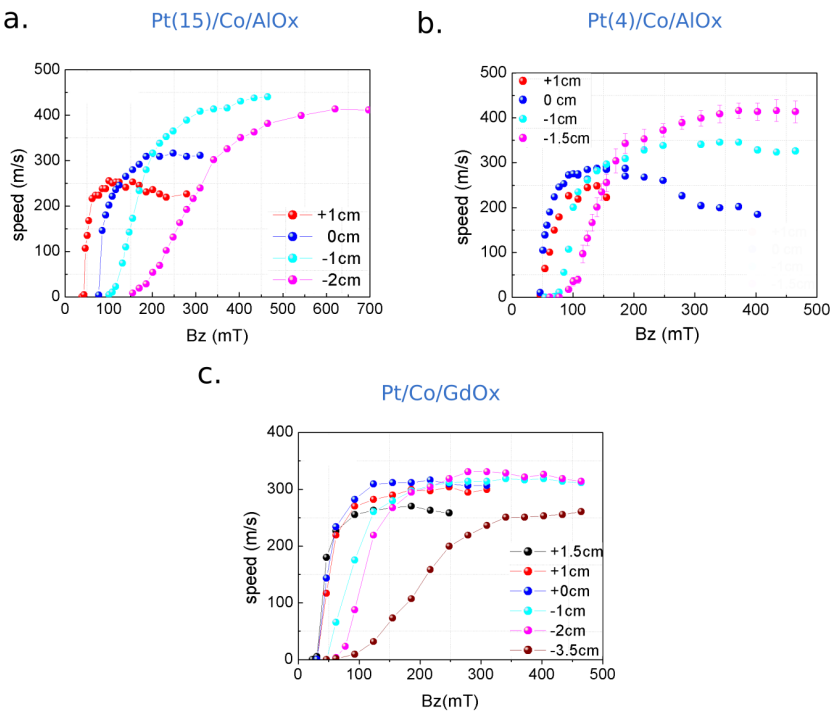

Fig. 5.15: DW speed vs H_z for different wedge position reflecting different oxygen coverage of the Co/MOx interface in **a.** Pt(15)/Co/AlOx **b.** Pt(4)/Co/AlOx **c.** Pt/Co/GdOx.

The curves reported in Fig. 5.15 show that the DW speed vs H_z strongly depends on the position on the sample. From equation 5.2 we know that the saturation velocity varies as $D_s/(M_s t)$. From the results of VSM-SQUID (Figs 5.10 and 5.11 and Table 5.1) we then expect that the velocities will be larger for the thin Al (Gd) side (smaller $M_s t$), which is the case for all the samples. We can also observe that the H_z field needed to reach the saturation speed increases as the sample gets oxidized. This may be due to two effects i) the increase of the DW pinning as the Co/MOx interface becomes more and more rough and ii) to the fact that the Zeeman energy driving the DW movement gets smaller (for equivalent field) as the sample gets more and more oxidized.

From equation 5.2, the variation of the DMI strength in the different positions also influences the velocity, and the knowledge or $M_s t$ and v_{max} allows us to determine the DMI.

The interfacial DMI strength measured for the different sample positions are plotted for all the samples in Figure 5.16.

The values are shown in Table 5.1 for a better comparison. We observe that the DMI strength values for the Pt/Co/GdOx sample, obtained with the two methods, differ in general by around ± 0.2 pJ/m^2. This is in our experience the precision with which we can estimate the interfacial DMI strength. The main causes of error are

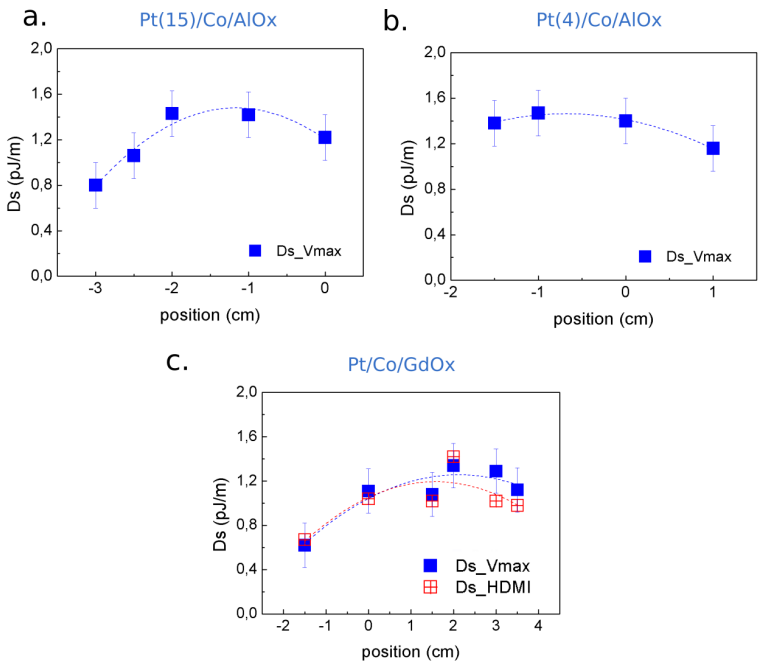

Fig. 5.16: The interfacial DMI strength D_s measured as function of different wedge position for **a.** Pt(15)/Co/AlOx **b.** Pt(4)/Co/AlOx **c.** Pt/Co/GdOx.

the bad knowledge of the exchange stiffness for the first method, and the error in the calculation of the Walker speed in the second method.

Tab. 5.1: Unit surface magnetization M_st, effective anisotropy field μ_0H_k, saturation domain wall speed v_{MAX}, DMI field μ_0H_{DMI}, interface DMI energy density D_s extracted from v_{MAX} and form μ_0H_{DMI} for some selected positions along the wedged for all the samples.

Sample	x	M_st	μ_0H_k	t_1 (XRR)	K_u*t_1	t_2 (M_s)	K_u*t_2	v_{MAX}	μ_0H_{DMI}	D_s^{vMAX}	D_s^{HDMI}
	cm	*10^{-3} A*	*T*	*nm*	*mJ/m²*	*nm*	*mJ/m²*	*m/s*	*mT*	*pJ/m*	*pJ/m*
Pt(15)/Co/AlOx	-3	0.54	1.85	0.55	1.40	0.38	0.97	410		0.8	
	-2.5	0.7	1.75	0.63	1.56	0.49	1.22	420		1.06	
	-2	0.86	1.52	0.71	1.64	0.6	1.41	440		1.36	
	-1	1.27	0.9	0.91	**1.7**	0.9	**1.69**	310		**1.42**	
	0	1.41	0.53	0.97	1.56	1	1.61	240		1.22	
	1	1.47	0.23	0.97	1.36	1.04	1.46				
Pt(4)/Co/AlOx	-2	0.54	1.62			0.38	0.91				
	-1.5	0.92	1.14			0.65	1.33	415		1.38	
	-1	1.18	0.79			0.83	**1.50**	345		**1.47**	
	0	1.36	0.42			0.96	1.48	285		1.4	
	1	1.31	0.21	0.97	1.34	0.92	1.29	245		1.16	
Pt/Co/GdOx	-1.5	0.68	1.62	0.5	1.19	0.48	1.15	255	>260	0.62	0.83
	0	0.93	1.24	0.62	1.31	0.65	1.39	330	260	1.11	0.99
	1.5	1.07	1.05	0.75	1.48	0.75	**1.50**	320	220	1.21	1.09
	2	1.12	0.90	0.83	**1.55**	0.79	**1.49**	315	190	**1.34**	1.19
	3	1.17	0.74	0.87	1.53	0.82	1.46	300	150	1.29	0.97
	3.5	1.15	0.77	0.84	1.49	0.81	1.45	270	170	1.12	0.93

We observed that the optimum coverage of the top Co interface with oxygen not only determines the maximum of the anisotropy but also optimizes the interfacial DMI (Fig. 5.17).

5.4 Results and discussion

The VSM-SQUID measurements, coupled with the XRR measurements, allowed us to confirm that the oxidation degree of the Co layer changes continuously along the wedge. When the Co starts oxidizing, the unit surface magnetization $M_s t$ measured by VSM-SQUID decreases while keeping the spontaneous magnetization more or less constant. This can be deduced by comparing the variation of $M_s t$ and the t_{Co} thickness obtained by XRR.

For the thickest Al and Gd layers, $M_s t$ shows a plateau at a high value or a weak variation, meaning that the oxygen has not penetrated in the Co layer yet. The perpendicular magnetic anisotropy is related to the magnetization variation. At the first stages of the oxidation of the Co/Al(Gd) interface, the PMA increases and reaches a maximum for a Al(Gd) layer thickness for which the $M_s t$ starts decreasing (i.e. when the Co layer starts oxidizing). This behavior is in agreement with the results presented by Manchon *et al.* [Man+08] that found that the optimum PMA is obtained when the Co layer is completely covered with oxygen, optimizing the number of Co-O bonds at the top Co interface. Let us remind that this implies that the PMA in Pt/Co/MOx samples arises from two contributions, one from the Pt/Co interface as known for example for Pt/Co multilayers, and another one arising from the Co/O interface.

The decrease of PMA for thinner Al(Gd) layers, and in particular the strong decrease for the thinnest cap layers, may be due not only to the formation of an oxide layer which decreases the PMA contribution from the top Co interface, but also to a possible degradation of the Pt/Co interface when the oxide layer thickness becomes similar to the interface roughnesses.

The most important result of this study is that the effective DMI strength in the Pt/Co/MOx stacks changes in a non monotonous way, similarly to the magnetic anisotropy. The optimum coverage of the top Co interface with oxygen not only determines the maximum anisotropy but also optimizes the interfacial DMI. Note that the strong decrease of D_s on the thinner part of the wedge might be due, as for the PMA, to the decrease of the DMI strength also at the Pt/Co interface. If we concentrate on the thick MOx part of the stacks, where the Co layer is underoxidized and the Pt/Co interface can be assumed to stay unchanged, this result is in our opinion a strong evidence of the contribution of the Co/O interface to the effective DMI. The increase of the DMI value going from the underoxidized part (thickest Al or Gd layer) to the optimum oxidation region indicates that the DMI at the Co/O interface has the same sign as that of the Pt/Co interface.

All these results are summarized on the Figure 5.17.

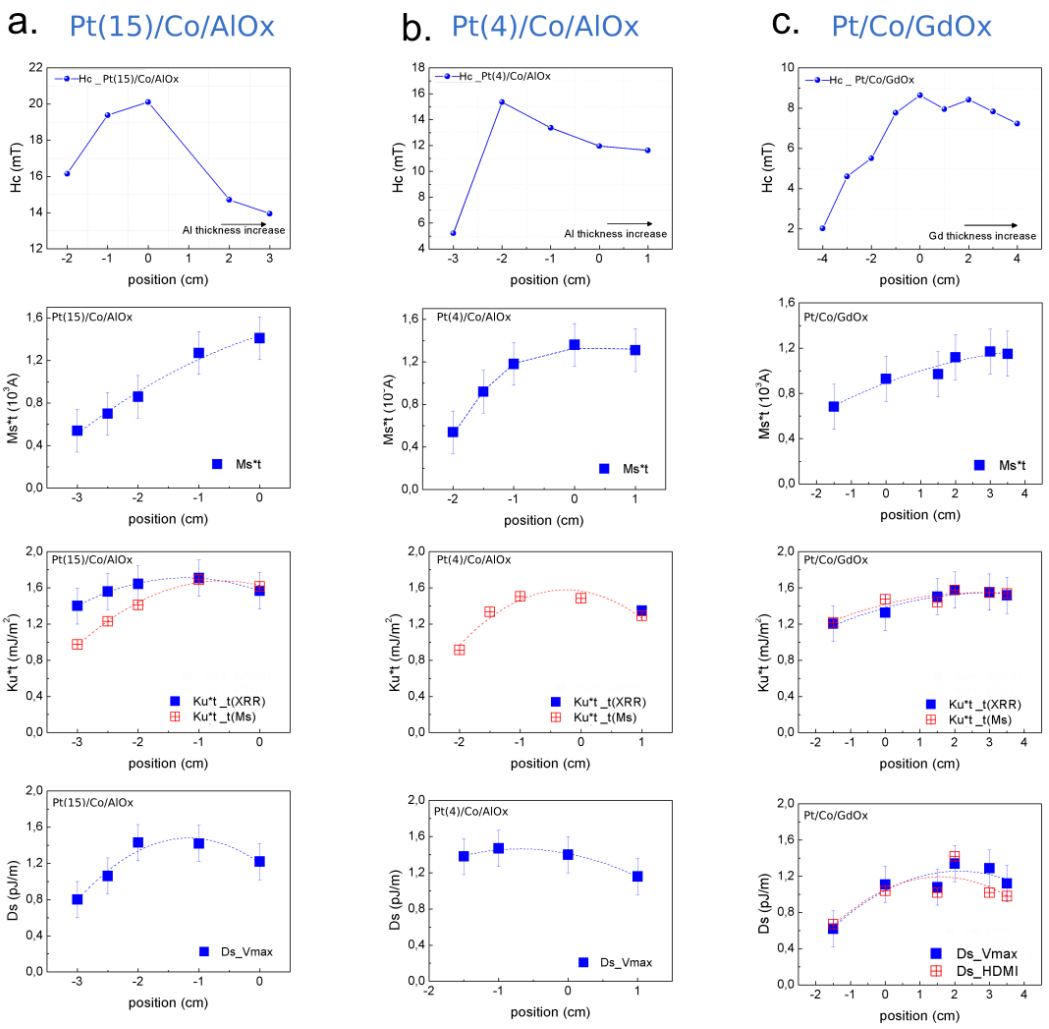

Fig. 5.17: Curve of coercive field H_c, unit surface magnetization M_st, interface magnetic anisotropy K_ut and interfacial DMI strength D_s measured as a function of the wedge position (as a function of the oxidation) for the **a.** Pt(15)/Co/AlOx **b.** Pt(4)/Co/AlOx **c.** Pt/Co/GdOx sample.

Nevertheless, the contribution of the Co/O interface is small with respect to that of the Pt/Co interface. How can we get to this conclusion ? Our data indicate that K_s and DMI change similarly as a function of oxidation. We can then assume that the threshold oxidation above which the sample acquires PMA (due to the contribution of the top Co interface) also corresponds with the appearance of a non negligible DMI at the Co/O interface. This situation is realized in the wedge position with largest Al (Gd) thickness, as beyond this the magnetization of the layer turns in the plane. The interface DMI at the Pt/Co interface is then of the order $1.1 - 1.2$ pJ/m in these samples, with an increase of the order of 0.2 pJ/m for the optimum oxidation degree. This is a small increase compared to the total DMI, but what should be kept in mind is that for most (or all) of the samples studied experimentally in the literature so far, the cap layer induces a strong reduction of the DMI see for example [Aje+17]. Larger

values of the effective DMI were found for Pt/Co/MgO layers [Bou+16], but in that case only one sample oxidation was studied, which made impossible to establish whether the larger DMI was due to the better Pt/Co interface or the more important contribution of the Co/MgO interface to the DMI [Aje+17]. Note however that the values of interfacial DMI for optimum quality epitaxial Pt/Co/Al – with unoxidized Al – where the PMA comes exclusively from the Pt/Co interface, were found (by our group in collaboration with IMDEA, Madrid) to be of the order of 1.3 pJ/m. This value is comparable to that attributed to the Pt/Co interface in our samples, the small reduction of the DMI in our non-epitaxial samples being probably due to the lower quality of the Pt/Co interfaces.

The similar variation of the DMI strength and the magnetic anisotropy invokes similar microscopic mechanisms for the variation of K_s and DMI.

Some recent theoretical works invoke the presence of DMI at the interface between a ferromagnetic layer (Co or Fe) and an electronegative atom (oxygen or carbon). The DFT calculations of Belabbes *et al.* [Bel+16] consider the case of Ir(001)/Fe(1ML)/O and show that the DMI can be tuned by controlling the oxygen coverage. In this extreme case where the FM is only 1ML thick and the FM layer cannot be seen as having two separate interfaces, it is shown that the DMI strength and sign are controlled by the hybridization of the Co-3d and HM-5d electronic bands [Bel+16]. The charge transfer between Co and O can modify the Co-HM distances and modify the 3d -5d hybridization, therefore changing the 3d -DOS at the Fermi level and the DMI. The *ab-initio* calculations in [Bou+16] consider a thicker FM layer in Pt(111)/Co(3ML)/MgO. The layer resolved calculations show that although the main contribution to the DMI is situated at the Pt/Co interface, a significant DMI – corresponding to about one third of the value of that of the Pt/Co interface - of the same sign is also present at the Co/O interface. These theoretical data are in qualitative agreement with our results.

The origin of the DMI at the Co/O interface - where the SOC is expected to be weak - is still an open question, as well as the correlation between the increase of PMA and that of the DMI.

The *ab-initio* calculations of Yang *et al.* [Yan+16] on Pt/Co/MgO trilayers show very interestingly, that while at Co/Pt interface the SOC energy source is located in the interfacial Pt layer, which is typical of the Fert-Levy model, at the MgO/Co interface the DMI is localized in the interfacial Co layer and the SOC energy source also located in the same interfacial Co layer. This indicates that the DMI at the Co/O interface has to be ascribed to a different mechanism. The authors suggest that the DMI at the MgO/Co interface may be governed by the Rashba effect, where the DMI can be expressed as:

$$D = 2K_R A \tag{5.3}$$

where A is the exchange stiffness and K_R is determined by the Rashba coefficient α_R given by $K_R = \frac{2\alpha_R m_e}{\hbar^2}$ [Kim+13].

On the other hand, Barnes *et al.* [Bar+14] in their recent paper propose that the Rashba magnetic field due to the internal electric field present at the interface between a ferromagnetic layer and an oxide, like the Co/oxide interface, can make an important contribution to the perpendicular magnetic anisotropy.

The Rashba-based theory may therefore provide a common ground to explain the simultaneous increase of the DMI and the PMA at the Co/oxide interface in our samples. This hypothesis is currently being explored by C. Lacroix (Institut Néel) and M. Chshiev (SPINTEC) who are developing a theory allowing to treat DMI and PMA in the same framework. The aim of this work is to verify whether the modification of the 3d band filling due to the modification of the electric field at the interface (via the change of oxidation degree) gives a similar trend for the strength of the DMI and the PMA.

5.5 Summary

In this chapter, we have reported the study of the dependence of DMI on the degree of oxidation of the Co/MOx interface in a series of Pt/Co/MOx (M= Al or Gd) trilayers. Results are in good agreement with those of Manchon *et al.* [Man+08] who found that the optimum PMA is obtained when the Co layer is completely covered with oxygen. We showed also that the optimum coverage of the top Co interface with oxygen not only determines the maximum anisotropy but also optimizes the interfacial DMI. Knowing that at the underoxidized part of the wedge, the Pt/Co interface remains unchanged with oxidation, there is a strong evidence that the Co/O interface contributes to the effective DMI. Also is observed that the DMI increases going from the underoxidized to the optimum oxidation region which proves that at the Co/O interface it has the same sign as that of the Pt/Co interface, consistent with what was found by *ab-initio* calculation in Boulle *et al.* [Bou+16]. Our originality here was to show in different groups of samples that the Co/O interface can make an important contribution to PMA as well as to DMI.

The results presented in this chapter have been published in:

Dayane de Souza Chaves, Fernando Ajejas, Viola Krizakova, Jan Vogel, Stefania Pizzini. “Dependence of Dzyaloshinskii-Moriya interaction on the oxygen coverage in Pt/Co/MOx trilayers”. In: arXiv preprint arXiv:1708.08516.

They have been submitted to Physical Review Letters and are in the referee process.

6

Domain wall motion in Gd_xCo_{1-x} thin layers close to the compensation composition

In this chapter we report the preliminary study of domain wall motion in Pt/GdCo/Ta thin film samples, driven both by magnetic field and electrical current. The samples are grown as a wedge with a gradient of composition. We demonstrate that close to the compensation composition at room temperature, the domain walls are driven very efficiently by the spin-orbit torque.

6.1 Introduction

The study of domain wall motion in GdCo alloy samples is motivated by the work described in chapter 4, where we show that in Pt/Co/Gd trilayers with large DMI and reduced magnetization, domain walls can be driven to large velocities with a saturation speed proportional to D/M_s at room temperature. The magnetization in the Pt/Co/Gd sample described before is decreased by a factor two with respect of the Pt/Co/GdOx trilayer, because of the partial interdiffusion of Gd and Co layers. In this interface alloy layer the Gd and Co moment couple antiparallel to each other, giving rise to a decrease of the total magnetization. We have estimated that the magnetic Gd layer at room temperature is around 0.3nm thick. One of the options for decreasing further the total magnetization, is to reduce the total Co thickness, or to anneal the sample in order to increase the interdiffusion. However, this latter option may also give rise to an increase of the interdiffusion at the Pt/Co interface, leading to a reduction of the DMI strength. Moreover, none of these methods allows us to tune sufficiently well the resulting magnetization, which is strongly dependent on the exact composition. Our strategy has been therefore to attempt to prepare Gd_xCo_{1-x} alloy samples with a gradient of composition around the compensation composition (i.e. composition giving rise to $M_s = 0$) at room temperature, so that within the same sample we could get access to a large variation of M_s.

For ferrimagnetic samples at (or near) the compensation temperature or the compensation composition, magnetic fields do not act on the magnetization (or large magnetic fields are necessary to act on the magnetization and move domain walls).

The effect of the amplitude of magnetization on the current-driven domain wall motion is still open to discussion. In the case of the standard spin-transfer torque, it is expected that the torque varies as $1/M_s$. It is also predicted that the spin-orbit torque associated to spin Hall effect (SOT-EHE) acting on chiral Néel domain walls in HM/FM/cap trilayers (HM-heavy metal, FM=ferromagnet) is varying as $1/M_s$ and proportional to D as showed Thiaville *et al.* [Thi+12] in the Figure 2.17 (see Chapter 2). However, so far only a few teams have studied SOT in ferrimagnetic systems, mainly for applications to magnetization switching, and a consensus has not been reached concerning the variation of the SOT efficiency with the net magnetization of the ferrimagnet.

In RE-TM alloys (RE=rare earth, TM=transition metal), since the 4f orbitals, responsible for the magnetism of rare earth atoms, are far below the Fermi level, one might expect that TM atoms, rather than RE atoms, predominantly interact with the spin currents (like the ferromagnetic materials). However, recent experiments argued that the SOT acts on the net magnetization [FL16; Ued+16]. Particularly, a divergence of the effective SOT field near the magnetization compensation point has been reported [FL16; Ros+17; Mis+17; Je+18]. However, no reduction of the threshold switching current density has been observed at the compensation [FL16; Mis+17], unlike the expectation of the minimized current density in the case that the SOT was acting on the net magnetization. This highlights today's poor understanding of SOT-driven magnetization switching and DW motion in ferrimagnetic systems.

No work has so far been published in the literature concerning SOT-driven domain wall dynamics in ferrimagnetic alloys. In the following, we will show our preliminary results on this subject.

Ferrimagnetic alloys

A ferrimagnet can be considered as an antiferromagnet with two inequivalent sublattices, so that the net magnetization can differ from zero. The difference between the ordering in ferromagnetic and ferrimagnetic materials is schematically shown in Figure 6.1. In a ferrimagnet, we can define two different magnetic sublattices. The magnetic moments within each sublattice are ferromagnetically coupled, whereas these two sublattices are coupled antiferromagnetically.

A special class of ferrimagnets are intermetallic compounds consisting of solid phases of two or more metallic elements. This class of materials is used in many applications such as high-performance permanent magnets ($SmCo_5$, $Nd_2Fe_{14}B$) or for magneto-optic recording (TbFeCo). Due to their electronic properties and metallic behavior, these ferrimagnets are interesting for spintronics.

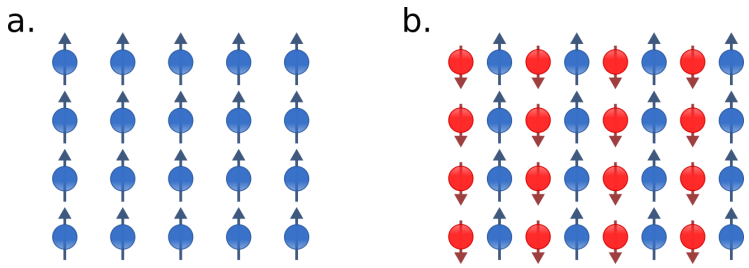

Fig. 6.1: **a.** Magnetic configuration of a ferromagnetic material. **b.** In a ferrimagnetic two (or more) mutually antiparallel different sublattice can be distinguished.

In this chapter, we will concentrate on Gd_xCo_{1-x} alloys. In this compound, the antiparallel coupling between Co – 3d and Gd – 5d moments, together with the ferromagnetic intra-atomic exchange interaction between the Gd – 4f moments and the Gd – 5d moments, leads to an antiparallel alignment between Co – 3d and Gd – 4f moments. The total (net) magnetization of the system is then given by the superposition of the sublattice magnetizations $M_{T\,Gd-Co} = M_{Co} - M_{Gd}$.

In a mean field model, each magnetization sublattice can be modeled using the Brillouin theory. For the A sublattice it reads

$$M_A = N\mu_A B_J\left(\frac{\mu_0 \vec{\mu}_A \vec{H}_A}{K_B T}\right) \tag{6.1}$$

where N is the number of atoms per unit volume, B_J is the Brillouin function, the term $\vec{H_A}$ expresses the so-called mean internal magnetic field which takes into account the interaction between the spins on nearest-neighbor atoms and the magnetic moment μ_A is related to the total angular momentum $\vec{J}$ by relation

$$\vec{\mu} = -g\mu_B \vec{J}, \tag{6.2}$$

where g is the so-called g-factor or Landé factor and μ_B is the Bohr magneton.

In the case of Gd_xCo_{1-x} alloy, this gives :

$$M_{Co} = (1-x)N\mu_{Co}B_{JCo}\left[\frac{\mu_0 \vec{\mu}_{Co}\left(\vec{H}_{app} + \lambda_{CoCo}\vec{M}_{Co} - \lambda\vec{M}_{Gd}\right)}{K_B T}\right] \tag{6.3}$$

$$M_{Gd} = (x)N\mu_{Gd}B_{JGd}\left[\frac{\mu_0\vec{\mu}_{Gd}\left(\vec{H}_{app} + \lambda_{GdGd}\vec{M}_{Gd} - \lambda\vec{M}_{Co}\right)}{K_BT}\right] \tag{6.4}$$

where $(1 - x)$ is the Co content. Typically, the molecular field coefficients are of the order $\lambda_{CoCo} \sim 10^3$, $\lambda \sim 10^2$ and $\lambda_{GdGd} \sim 10^1$. Since the Gd-Gd exchange interaction is very weak and has a minimum influence on the magnetization dependence, it is usually neglected.

Using the parameters for the alloy $Gd_{22}Co_{78}$, A. Hrabec [Hra11] calculated the temperature variation of the Co , Gd and GdCo magnetization, that is shown in Figure 6.2.

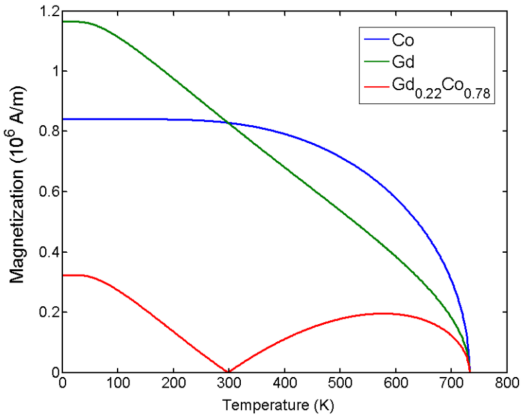

Fig. 6.2: Calculated temperature dependence of the magnetization in the case of x = 0.22. The obtained compensation temperature T_{comp} = 300K. Image from [Hra11].

The different temperature variations of the Co and Gd magnetization result in the presence of a so-called compensation temperature at around T = 300K. When $T < T_{comp}$, the moment of the Gd sublattice dominates, so the Gd magnetic moments dictate the total magnetization orientation with respect to the applied magnetic field. The opposite occurs for $T > T_{comp}$ where the Co magnetization is larger.

Also in his work [Hra11] A. Hrabec presents the compensation temperature dependence as a function of the composition Fig. 6.3. The calculated T_{comp} distribution can be expressed, in a reasonable approximation, by a linear dependence which reads

$$\frac{\Delta T_{comp}}{\Delta(1-x)} = 44 \pm 1\frac{K}{at.\%} \tag{6.5}$$

T_{comp} changes very strongly with composition, as 1% change of the Gd content changes T_{comp} by approximately 44K. This can also be seen in the calculations of

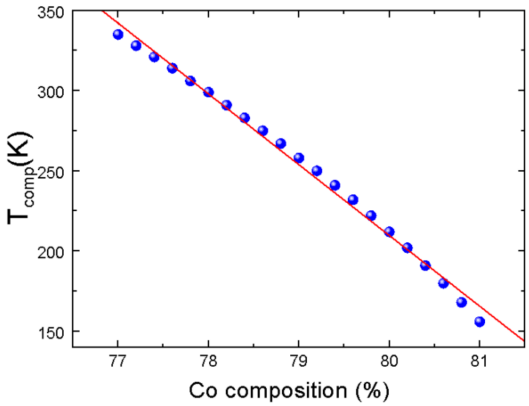

Fig. 6.3: Calculated composition dependence of the compensation temperature T_{comp} as a function of Co content $(1 - x)$. The range of the Co composition is between to 0.77 and 0.81 the dependence was linearized by $\Delta T_{comp} = 44 \pm 1$K/at.% (red line).Image from [Hra11].

Hansen *et al.* [Han+89] that are reported in the Figure 6.4. Note that the variation of T_{comp} vs. composition is much larger in these calculations with respect to those reported in Ref. [Hra11]. This has been attributed to the different parameters used in the mean-field calculations, in particular the value for the intersublattice molecular field coefficient λ. This points to the difficulty to compare models and experiments in the published data.

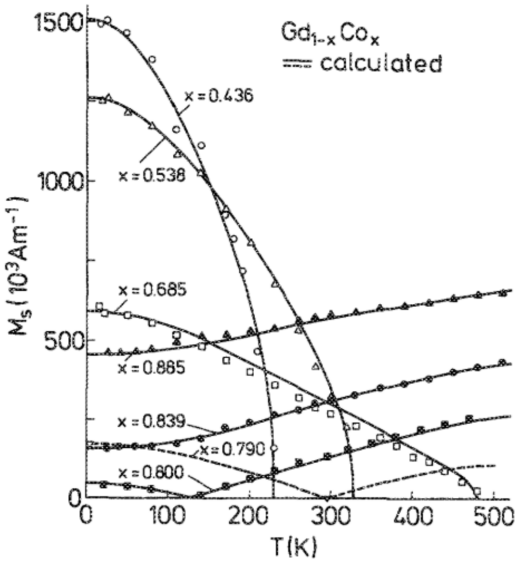

Fig. 6.4: Temperature dependence of the saturation magnetization for $Gd_{1-x}Co_x$ in different concentration of Co. Image from [Han+89].

In 1972 Orehotsky *et al.* [OS72] found that GdCo and GdFe amorphous thin films can show large perpendicular magnetic anisotropy. It was also proven that such thin films containing cylindrical domains with out-of-plane magnetization were suitable for magneto-optical recording.

No macroscopic magnetic anisotropy is expected to be present in an ideal amorphous state. Macroscopic magnetic anisotropy implies the presence of a structural anisotropy at least on a nanometer scale, together with an interaction between magnetic moments and the anisotropic structure via spin-orbit coupling. Thermally evaporated films of amorphous GdCo have been found to have an in-plane anisotropy. On the other hand, Gd-Co films have perpendicular anisotropy when magnetron sputtering technique is used. Several possible origins of the perpendicular magnetic anisotropy can be found in the literature but no consensus has been reached yet. One of the possible microscopic mechanism leading to PMA in these films is the columnar growth giving rise to uniaxial anisotropy.

6.2 Methods

6.2.1 Sample preparation

The GdCo alloys were grown by magnetron sputtering at Institut Néel. The aim was to obtain samples of composition close to $Gd_{22}Co_{78}$, for which the compensation temperature is close to RT. Since controlling the composition with a large precision is very difficult with magnetron sputtering, and since T_{comp} is very sensitive to composition, we have adopted the strategy to grow samples with a gradient of composition. This was obtained using a Co target, on top of which two Gd foils were placed in an off center position (Fig. 6.5). The size of the Gd foils was chosen to be about 20% of the size of the Co target.

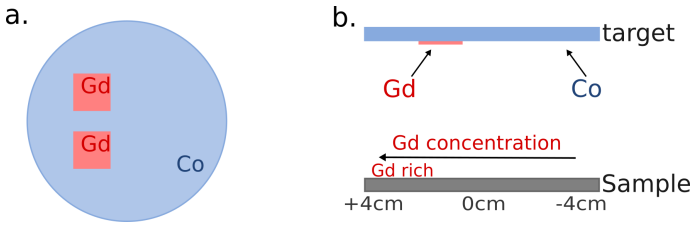

Fig. 6.5: Scheme of the type of deposition used to achieve the gradient composition. **a.** Top view of the Co target with pieces of Gd which give us a composition close to $Gd_{22}Co_{78}$. **b.** Side view showing how the gradient composition works in relation to the target. Our Si substrates are 8 cm long, and the sample positions used in the text are indicated in the figure.

The off-axis position of the Gd foils is such that the composition of the alloy deposited on a substrate located in front of the target changes along the sample. The gradient of composition depends on the distance between target and substrate. For a target-substrate distance of 50mm, it was found that the compensation composition at RT ($Gd_{22}Co_{78}$) fell within the 8cm long Si substrate. The process however revealed to be highly unreproducible: this was probably due to the fast oxidation of the

Gd target under relatively high pressures within the chamber (on average some 10^{-7} bar) and the difficulty to recover a similar Gd surface after etching of the Gd target before each deposition. Several samples were grown using different growth parameters (power of the Ar plasma, target-substrate distance), but in some cases the compensation composition was not found to be inside the samples or the magnetization was found to be in-plane. In the following we will show the results mainly for a Si/SiO2/Ta/Pt/GdCo(**4nm**)/Ta trilayer for which the compensation composition was found to be within the 8cm long sample, and which present PMA for each sample position. We will also show some comparisons with a similar sample having slightly thicker GdCo Si/SiO2/Ta (4nm)/ Pt (8nm)/ GdCo(**4.8nm**)/Ta (3nm) and a sample with thinner GdCo layer Si/SiO2/Ta (4nm)/ Pt (8nm)/ GdCo(**2nm**)/Ta (3nm).

6.2.2 Structural Characterization

XRR measurement

As already described, the XRR spectra were carried out with the D8 Discover diffractometer at Institut Néel and the fits were done using the Brucker's LEPTOS software.

For the calibration of the GdCo layer thicknesses, X-ray reflectivity measurements (see Section 3.2.1) were carried out on Si/SiO2/GdCo/Pt and Si/SiO2/Pt/GdCo/Pt reference samples obtained with different deposition times.

Figure 6.6a. shows the XRR data measurement for the Si/SiO2/GdCo/Pt samples in the position 0cm together with the fit. The results of the fit are shown in the Table (Fig. 6.6b). The GdCo layer thickness was calibrated for deposition times 60″, 20″ and 10″ which allowed us to confirm the linear variation of the layer thickness with deposition time (Fig. 6.6c.). Figure 6.6d. shows the XRR data measurement for the Si/SiO2/Pt/GdCo/Pt sample.

The XRR data were fitted using two layers (Pt and GdCo , called Co in the Table 6.6b). The Co density was used as a starting parameter for the fit.

This calibration was used to prepare the complete samples. In this chapter we will mainly treat the sample having the following composition: Si/ SiO2/ Ta(4nm)/ Pt(4nm)/ GdCo(4nm)/ Ta(3nm). Note that the error in the estimation of the GdCo layer thickness is of at least 0.5nm. Note the large thickness of the GdCo layer, with respect to the ferromagnetic thicknesses of the samples described in the Chapters 4 and 5.

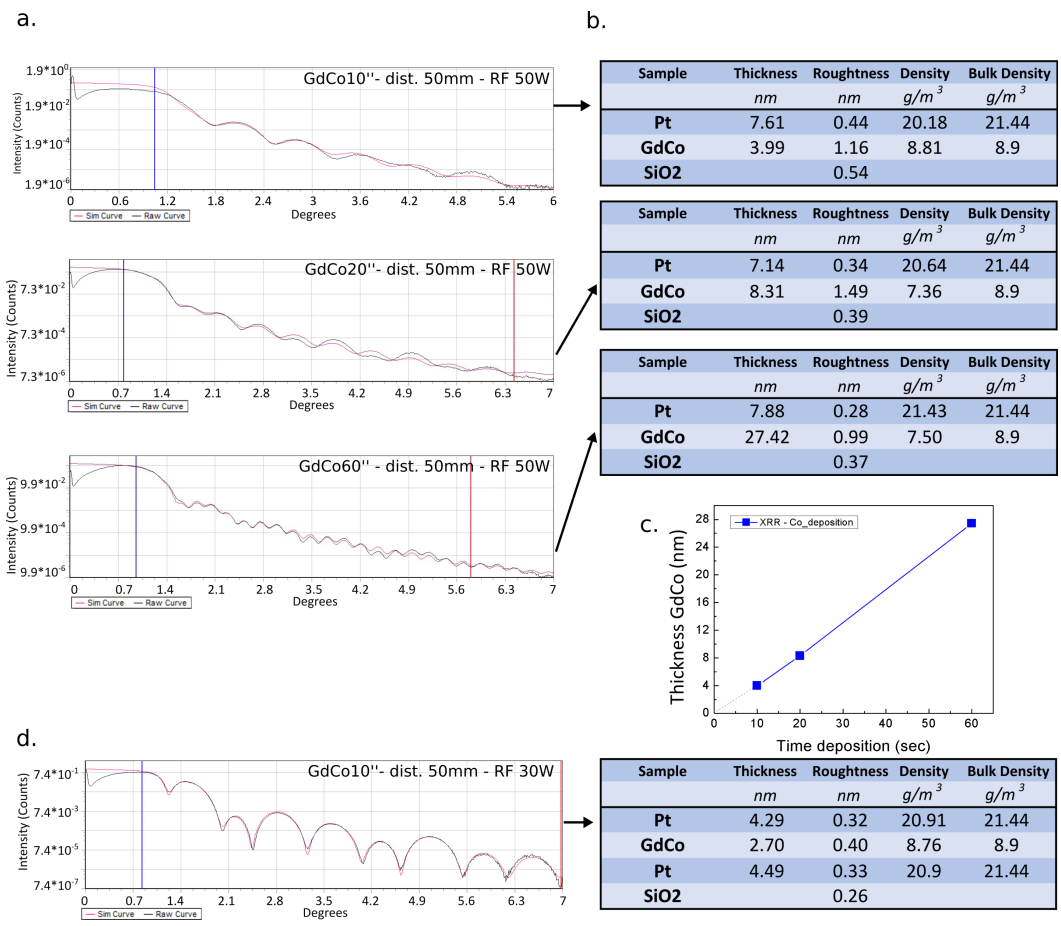

Fig. 6.6: **a.** XRR data (black curve) with fit (red curve) using Brucker's LEPTOS software **b.** Table showing the parameters found with the fit in a. for GdCo/Pt sample in 0cm. **c.** Plot with the linear fit for the Co thickness as a function the deposition time (values take from Table in b.). **d.** XRR data (black curve) with fit (red curve) and table showing the parameters found with the fit for Pt/GdCo/Pt sample in 0cm. Note the large roughness of the bottom GdCo interface due to the rough SiO2 layer. This roughness is strongly decreased in the Pt/GdCo/Pt samples.

Some XRR curves were also measured for the complete sample (Si/SiO2/Ta/Pt/GdCo/(Ta or Al), but the fits of these curves revealed to be problematic. Our interpretation is that the composition of the GdCo thickness is not homogeneous in depth. A segregation of Gd at the layer surface has been already proposed by other authors [Ber+17].

6.2.3 Magnetic Characterization by VSM-SQUID measurements

VSM-SQUID measurements of saturation magnetization M_s at 300K and, in some cases, in-plane saturation field, were carried out in different sample positions that correspond to different concentrations of Gd.

Figure 6.7 shows the unit surface magnetization $M_s t$ as a function of the sample position for the Pt/GdCo(4nm)/Ta sample. We can observe a large variation of the magnetization $M_s t$ with a minimum around +2 cm for which the compensation temperature is around 300K. This means that in this position (that we call the compensation composition at RT) the magnetic moments of the Co and Gd are equal and antiparallel leading to vanishing magnetization at RT.

In positions between −3cm and +2cm the magnetization is dominated by Co at RT, while between +2cm and +3cm M_s is dominated by Gd (see Figure 6.7). The variation of Gd content from one side to the other of the sample is of approx. 3% (from ca. ∼ 78% to ca. ∼ 81% - compare with Hansen curves in Figure 6.4). The magnetization versus temperature curve measured for the Pt/GdCo(4.8nm)/Ta sample is shown in Figure 6.7c. for two sample positions. In 0cm, the compensation temperature is around 220K, corresponding according to Hansen's data ([Han+89]) to around 75% Co content. For -1cm the Co content increases (larger magnetization at RT) and Co ratio should rise to around 81%.

a.

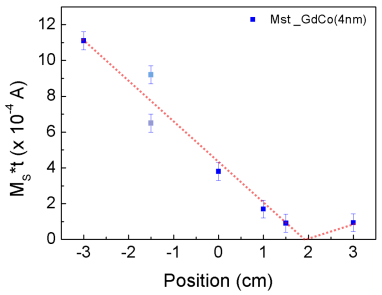

b.

Sample	position	$M_s t$	$\mu_0 H_k$
	cm	*10^{-4} A*	*T*
GdCo(4nm)	+3.0	0.94	
GdCo(4nm)	+1.5	0.91	4
GdCo(4nm)	+1.0	1.7	
GdCo(4nm)	0	3.8	2.19
GdCo(4nm)	-1.5	9.2	0.68
GdCo(4nm)	-3.0	11.1	
GdCo(4.8nm)	0	17.0	0.126
GdCo(4.8nm)	-1.0	4.0	

c.

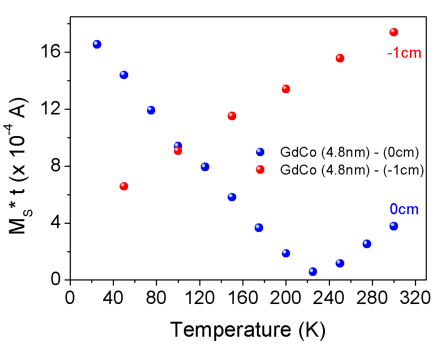

Fig. 6.7: **a.** Unit surface magnetization measured at 300K at different sample positions in the GdCo(4nm) sample. The two measurements for -1.5 cm were taken at different times, after different thermal treatment needed for patterning. **b.** Table of the values found for different positions of GdCo(4nm) for unit surface magnetization $M_s t$ and effective anisotropy field $\mu_0 H_k$. The results of the measurements carried out for some of the GdCo(4.8nm) sample positions are also reported in the Table. *c.* Magnetization vs temperature curve for the GdCo(4.8nm) sample for two different positions.

Note that, for an approximate GdCo thickness of 4nm, the maximum average magnetization M_s (found for −3cm position) is around 20% of that of pure Co. In

position +3cm, $M_s t$ approaches the minimum value measurable with the VSM-SQUID, and here M_s is around 2% of the value of pure Co.

6.3 Addressing domain wall speed and DMI strength as a function of composition

Figure 6.7 shows that the sample magnetization changes rapidly as a function of sample position, as the composition changes by some % from one edge to the other.

As already shown in Chapter 4, we expect the field-driven domain wall dynamics to be largely affected by this variation. However, at the beginning of this study, it was assumed that the DMI at the Pt/GdCo interface would not change largely compared to that of the Pt/Co interfaces studied before. As we will show later, our preliminary results show that that assumption was not correct. In order to probe the presence of chiral Néel walls and verify the sign of the chirality, first we measured the field-driven DW speed vs. in-plane field H_x.

Differential Kerr images are shown in the Fig. 6.8 where the expansion of a magnetic domain is observed. Without in-plane field (middle) ($H_x = 0$) we observe that the DW displacement is isotropic, while when the in-plane field is applied (positive or negative) the displacement becomes anisotropic following the direction of the applied field H_x. These data confirm the presence of chiral Néel walls with negative DMI, like for Pt/Co/(GdOx and Gd) samples.

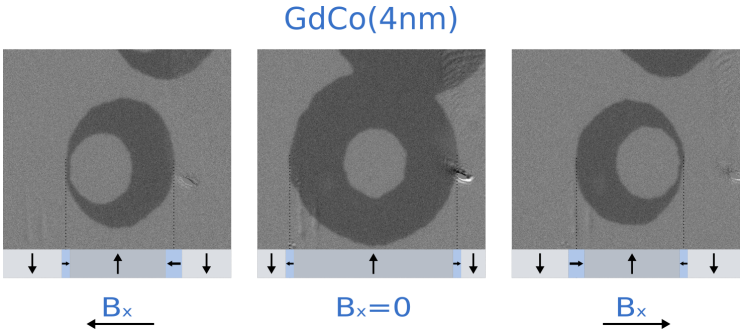

Fig. 6.8: Differential Kerr images showing the expansion of a bubble domain, driven by an out-of-plane field $B_z = 77$mT, in the presence of an in plane magnetic field of −62mT, 0mT and +62mT.

Figure 6.9 shows the variation of the DW speed vs in-plane field H_x driven by an out-of-plane field of 77.5 mT. The DMI field $\mu_0 H_{DMI}$ occurs at the minimum of the curves i.e. at 165mT.

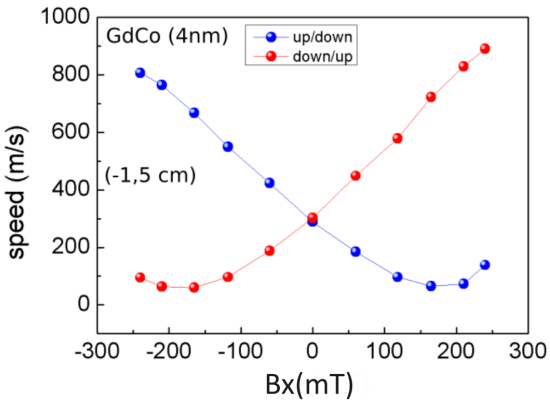

Fig. 6.9: DW speed vs. in-plane magnetic field B_x, measured in the position -1.5cm for up/down and down/up DW propagating in ± direction, driven by 20ns long B_z pulses of 77.5mT in −1.5cm position.

We would now like to illustrate another method to highlight the DMI field, consisting in measuring the current-driven domain wall speed vs in-plane field.

For this purpose, the sample was patterned into 2μm wide and 20μm long strips. Ten parallel strips were connected to a common injection pad covered by Ti/Au contacts. This allowed us to visualize the motion of several domain walls, and this improved the statistics of our measurements. The methods used to pattern the sample are described in section 3.1.2.

The domain wall motion was studied by differential Kerr microscopy. The domain walls were injected into the stripes using magnetic field pulses. The initial state was used as background image. Current pulses (typical length 2ns) were then applied to move the domain walls (see Figure 6.10). The black contrast in the figure represents the domain wall displacement (from top to bottom) of the ten up/down domain walls during the current pulses (black contrast corresponds to up magnetization). The domain wall speeds were obtained by dividing the displacement by the total duration of the current pulse(s).

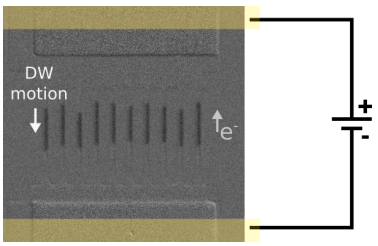

Fig. 6.10: Example Pt/GdCo(4nm)/Ta sample with a 5ns pulses ×10 ; J = 1.5×10^{12}A/m^2.

Figure 6.11 shows the variation the current-driven DW motion (current density 1.57×10^{12}A/m^2) as a function of the amplitude of the in-plane field, applied in the

direction parallel to the strips i.e. perpendicular to the DW direction. Curves are shown both for up/down and down/up DW, created starting either from a saturated state oriented up or down.

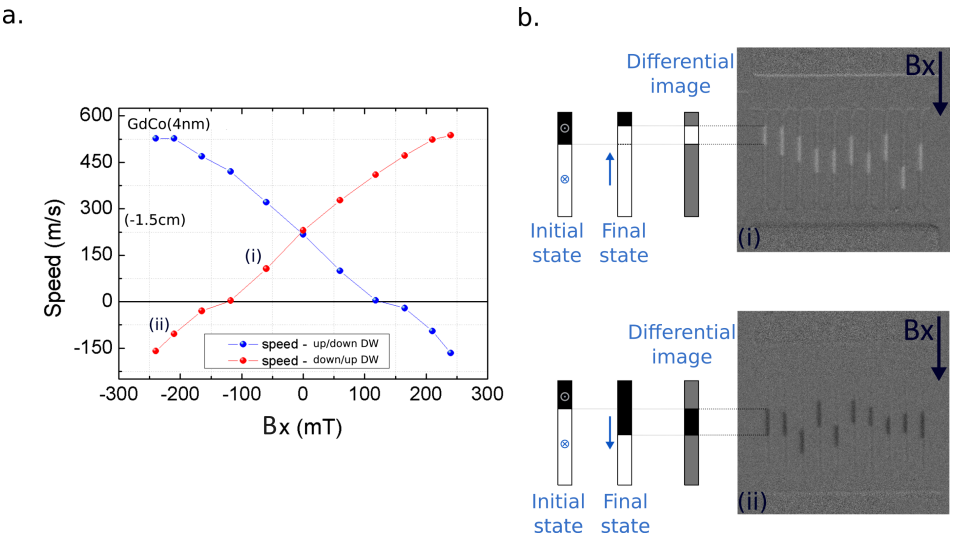

Fig. 6.11: **a.** Current-driven DW speed ($J = 1.57 \times 10^{12} A/m^2$) measured for up/down and down/up DW as a function on H_x field amplitude applied parallel to the strips for the GdCo(4nm) sample in position -1.5cm. **b.** Differential Kerr images indicating the DW motion, black contrast corresponds to up magnetization.

In the absence of in-plane magnetic field, up/down and down/up DWs move against the electron flow, as for the Pt/Co/AlOx samples [Mir+11]. This is expected as the Spin-Hall material (Pt) is the same, and the DMI sign is negative for both samples.

Identically to the case of field-driven dynamics, the H_x field – applied in the direction of the magnetization at the center of the domain walls – stabilizes or destabilizes the chiral Néel wall depending on its direction with respect to the DMI field. If the H_{DMI} and the in-plane field are parallel, the DW speed increases through the increase of the DW width, while the opposite occurs for antiparallel H_x and H_{DMI}. When the H_x field is equal and opposite to the DMI field, the DW acquires Bloch structure and the torque will no longer be efficient. For H_x field larger and opposite to the DMI field, the DW magnetization switches sign. In this case, the torque acting on the DW will change sign and the DW starts moving in the opposite direction, parallel to the electron flow. This is shown by the two images shown in Figure 6.11.

Note that the switching field is around 160mT, very close to the field for which the domain wall speed versus in plane field presents a minimum.

The two measurements (field and current-driven DW speed vs H_x) show us that the DMI field is large i.e. that the Néel internal structure is stable against perturbations. If we recall the expression of the DMI field ($H_{DMI} = D/\mu_0 M_s \Delta$) we see that the large stabilizing field can be related to the small values of the magnetization found for this

sample composition (which is a factor 10 smaller than that of a single Co layer), and not necessarily to the large value of the DMI strength.

For these samples, using the DMI field amplitude to obtain the DMI strength is particularly "risky", as the value of the exchange stiffness in these ferrimagnetic materials has not been characterized and it depends on the composition and on the degree of crystallinity of the material [Kat+78].

For this reason we have privileged the use of the second method shown in Chapter 4 (saturation DW velocity) to obtain information about the DMI strength in this sample.

Figure 6.12 shows the DW speed vs out-of-plane field H_z measured by wide-field Kerr microscopy. We observe that the DW speed is strongly dependent on the sample position, as expected since the magnetization is changing along the sample (Table in Fig. 6.7). DW velocities vary between 250 m/s for position -3cm (largest M_s) to more than 700m/s obtained for large fields in position +1cm. Note that for the curve around the position +1.5 cm (close to the compensation composition at RT from VSM-SQUID measurements) the speed increases very slowly with the field H_z: since the magnetization is negligible very large fields are necessary to obtain the maximum speed. Similar results are found for sample Pt/GdCo(4.8cm)/Ta. Here, velocities up to 1000m/s can be obtained for the highest applied fields.

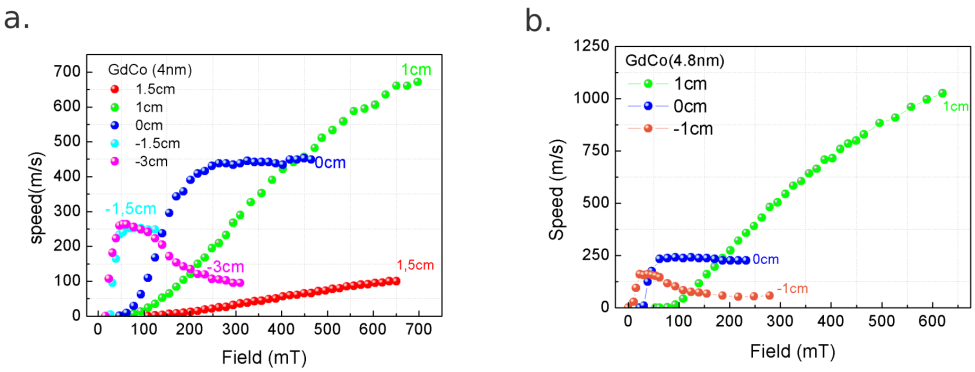

Fig. 6.12: DW speed vs H_z for different positions that correspond to different composition of **a.** Pt/GdCo(4nm)/Ta and **b.** Pt/GdCo(4.8nm)/Ta.

Using the expression $v_{sat} = \gamma(\pi/2)(D_s/M_s t)$ we can extract the interfacial DMI strength D_s from the saturation speeds, for sample positions -3cm, -1.5cm and 0cm (compositions with more Co concentration) for GdCo(4nm) and -1cm and 0cm for GdCo(4.8nm). This cannot be done for the other measured sample positions as the saturation speed is not reached even for fields as high as 700 mT. For GdCo(4nm) in 0cm ($M_s t = 3.8 \times 10^4$A) we obtain $D_s = 0.62$ pJ/m while for position -3cm (larger $M_s t = 11\text{x}10^4$A) we obtain $D_s = 1$ pJ/m. For position +1cm, where the saturation speed is for sure larger than 700 m/s, we can only claim that $D_s > 0.4$ pJ/m. Such

large speeds have already been observed for the Pt/Co/Gd sample in Chapter 4. However, in that sample, the DMI was much larger (D = 1.5 mJ/m for 1 nm Co) compared with the values found here. We therefore ascribe the large DW velocity to the strong reduction of the net magnetization.

In sample GdCo(4.8cm), we obtain D_s = 1 pJ/m in -1cm ($M_s t = 17 \times 10^4$A) and D_s = 0.35 pJ/m for 0cm, where $M_s t = 4 \times 10^4$A. (see Table 6.1). The values of DMI are reported in Table 6.1. In these samples, the DMI values are therefore strongly reduced with respect to samples having pure Gd/Co interfaces, and moreover D_s appears to change strongly with the composition.

The values of the DMI strength are strongly reduced with respect to those found in Pt/Co/MOx (chapters 4 and 5) not only because of the small interfacial DMI values but also because of the larger thickness of the GdCo layer (4nm). These are of the order of $0.25 - 0.1$ mJ/m^2, of the same order of magnitude of the critical DMI value necessary to stabilize chiral Néel walls in Pt/Co(0.6nm)/AlOx. However here, because of the much smaller magnetization, the domain wall demagnetizing field is reduced, and the transition between Bloch and Néel wall can be obtained for lower DMI values.

Routes for understanding the reasons for the DMI decrease will be discussed at the end of this chapter.

Because of this strong reduction of the DMI strength, the field-driven velocities obtained e.g. for position +1cm for the GdCo(4nm) sample is comparable to that of the sample Pt/Co/Gd in Chapter 4. However, because of the much reduced M_s, larger fields are required to obtain this speed.

We would now like to comment on the evaluation of the DMI strength using the H_{DMI} field method. As already explained, this method relies on the knowledge of the exchange stiffness of the material. If we consider the exchange stiffness used for pure Co films (A=16 pJ/m), we largely overestimate the DMI values with respect to those obtained from the saturation DW velocities. In order to obtain an agreement between the two values, the exchange stiffness (verified for GdCo(4nm) in 0cm and GdCo(4.8cm) in -1cm) has to be decreased to around A= 5 pJ/m. Small values of the exchange stiffness, down to 1 pJ/m, were found by Katayama *et al.* [Kat+78] for amorphous GdCo films, using the measurement of stripe domain periods in thick layers by Kerr microscopy. The exchange stiffness is observed to be sensitive to heat treatments, with the stiffness increasing as the annealing time or temperature increase. The values around 5 pJ/m found for our systems are therefore consistent with previous observations.

6.4 Current-driven domain wall speeds in GdCo samples

Before presenting some preliminary results concerning the current-driven domain wall dynamics in the Pt/GdCo/Ta alloy sample, we would like to present the speed-vs-current curves measured for the two samples studied in Chapter 4: Pt/Co(1nm)Gd vs. Pt/Co(1nm)GdOx. The samples were patterned into 2 μm wide, 20 μm long strips by e-beam lithography, as described above.

An example of the differential Kerr images obtained for the Pt/Co/Gd sample current-driven DW motion is shown in Figure 6.13. The black contrast represents the DW motion driven by current pulses of density $J = 1.4 \times 10^{12} A/m^2$. For these currents the DW move in the flow regime, and the same length of the displacement in all the strips shows the large reproducibility of the displacement and the negligible effect of defects.

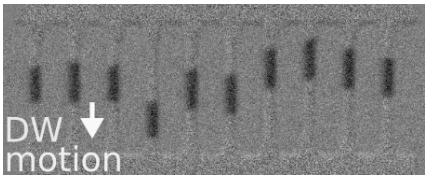

Fig. 6.13: Kerr differential image of Pt/Co/Gd sample driven by current pulses of density $J = 1.4 \times 10^{12} A/m^2$.

Domain walls move against the electron flow, as for the Pt/Co/AlOx samples [Mir+11]. This is expected as the Spin-Hall material is Pt, and the DMI sign is negative for the Pt/Co interface in both samples. The velocity was obtained as the ratio between the DW displacement and the duration of the current pulse. Typically 2-3 ns pulses (rise and fall time $<$ 300ps) were obtained using a fast pulse generator. The applied voltages were limited to 17V (the generator was developed for another application requiring high repetition rates, which limited the performance). This limited the current density that could be injected into the strips to around $2 \times 10^{12} A/m$. Domain wall speeds were measured as a function of current density, and the two curves obtained for Pt/Co/Gd and Pt/Co/GdOx (magnetization reduced by a factor two in Pt/Co/Gd) are shown in Figure 6.14. Note that for the Pt/Co/GdOx sample, the measurement could be carried out only up to $J = 1,5 \times 10^{12} A/m^2$ as the sample was heating too much for larger current density and random nucleation was occurring.

Similarly to the case of field-driven dynamics, the maximum DW speed is larger for the Pt/Co/Gd sample. Since we have shown that the DMI strengths in the two samples are very similar (D around 1.5 mJ/m^2 for 1 nm of Co) we attribute the different behavior to the difference in magnetization of the two samples. This result

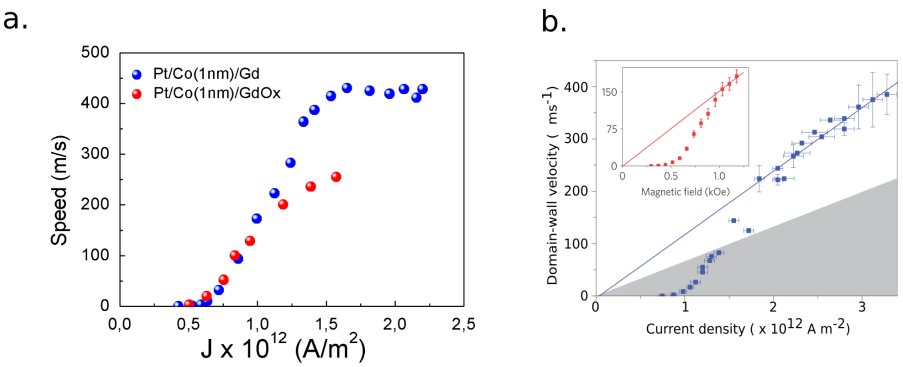

Fig. 6.14: **a.** Speed vs current density for Pt/Co (1nm)/Gd and GdOx **b.** Image from Miron *et al.* [Mir+11] for speed vs current density for Pt/Co (0.6nm)/AlOx.

tends to suggest that the angular momentum of the spin current from SHE in Pt is transferred to the total (net) magnetization, and not to the Co magnetization. Note that within the error bars of the measurement (M_s within 10%, sample thickness within 10%, DMI within 15 – 20%) the ratio of the two velocities($\sim 250/430 = 0.58$) can be considered as scaling with the magnetization ratio ($0.64/1.26 = 0.51$). Note also, that the smaller speeds found for the Pt/Co(1nm)/GdOx sample with respect to the Pt/Co(0.6)/AlOx [Mir+11] (see Figure 6.14) is due to the difference in Co thickness which significantly reduced the DMI strength in our sample. On the other hand, the speeds reached by DW in the Pt/Co/Gd sample are of the same order of magnitude as those of the Pt/Co/AlOx sample, despite the strong reduction of DMI due to the thicker Co layer (1 nm instead of 0.6 nm). This indicates that the loss of speed due to the decrease of DMI is "compensated" by the amplifying effect of the decreased magnetization induced by the Co-Gd intermixing at the top Co interface.

Following these encouraging results we measured the current-driven dynamics in the Pt/GdCo/Ta samples. Measurements were carried out for the sample described above (4 nm thick) and for a similar Pt/Co/GdCo(2nm)/Ta sample (GdCo(2nm)) where the GdCo thickness was reduced. For this sample, the compensation composition was found around position +2.5cm. The magnetization values measured for positions −1.5cm and 0cm are given in the following Table 6.1. The DW speeds are plotted as a function of current density in Figure 6.15.

The first remarkable result is that DWs can be moved with much lower current densities compared with the samples reported above. Velocities as high as 100 m/s can be obtained for $2.5 \times 10^{11} A/m^2$ while in the case of Pt/Co/AlOx of Miron *et al.* [Mir+11] such velocities were obtained only with current densities as high as $1.5 \times 10^{12} A/m^2$. This is a result of the smaller net magnetization.

Tab. 6.1: Thickness of Co layer (t), unit surface magnetization $M_s t$, interface DMI energy density D_s, maximum speed by field-driven DW v_{MAX}^{field}, maximum speed by current-driven DW $v_{MAX}^{current}$ and ratio $D_s/M_s t$ for the sample studied in this work.

Sample	Position	t (XRR)	$M_s t$	D_s	v_{MAX}^{field}	$v_{MAX}^{current}$	$D_s / M_s t$
	cm	*nm*	*10^{-4} A*	*pJ/m*	*m/s*	*m/s*	*10^{-8} J/mA*
GdCo(4nm)	-3	4	11.1	1	250		
	-1.5	4	6.5	0.65	275	280	0.1
	1.5	4	0.9	<0.6	>700	400	
GdCo(2nm)	-1.5	2	3.2	0.45	350	280	0.14
	0	2	1.8		>600	280	
GdCo(4.8nm)	-1	4.8	17	1	160		
	0	4.8	4	0.35	225		
Pt/Co/GdOx	0	1	12.6	1.5	300	250	0.12
Pt/Co/Gd	0	1	6.4	1.5	600	430	0.23

We can then notice that the largest speeds (obtained for $J \sim 10^{12} A/m^2$) are of the same order as those obtained for samples Pt/Co(1nm)/GdOx and Pt/Co(1nm)/Gd as well as those obtained in Miron *et al.* [Mir+11] for Pt/Co(0.6)/AlOx (Figure 6.14): 250 m/s for position −1.5cm (Co rich area with larger magnetization) and 400 m/s for position +1.5cm (where the magnetization is reduced by a factor 4).

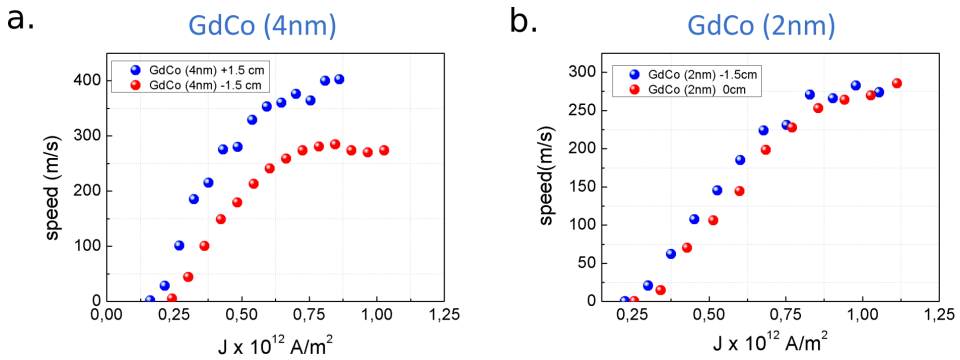

Fig. 6.15: Speed vs current density **a.** for GdCo(4nm) in position -1.5cm and +1.5cm **b.** for GdCo(2nm) in position 0cm and -1.5cm.

In the case of Ta/Pt/GdCo (2nm)/Ta sample, the maximum domain wall speeds are the same and around 250m/s for the two studied sample positions.

As described in Chapter 2, the torque exerted on the domain wall by the spin current generated in Pt by SHE can be associated to an effective perpendicular field $H_{eff} = (\pi/2)\chi M_s \cos\Phi$ and the velocity is expected to increase with the strength of the DMI (via the angle Φ of the DW magnetization) and to be inversely proportional to M_s. In the GdCo(4nm) sample, as we have seen above, the interfacial DMI strength is strongly reduced with respect to the case of samples with a "pure" Pt/Co interface; moreover, the layer thicknesses are much larger, which is also detrimental to the SOT effect. The high DW speeds for large current densities can then be ascribed to the strong reduction of the magnetization, with respect to that of pure

Co (or the Co inter-mixed with Gd in Pt/Co/Gd). In Table 6.1, we have reported the values of the DW speeds (for the largest J, where they appear to saturate) for all the studied samples, together with the ratio D_s/M_st, for the samples for which D_s could be reliably determined. We can notice that speeds around $250 - 280 m/s$ are obtained for similar D_s/M_s values. The largest speeds (of the order of $400 m/s$) are obtained for Pt/Co/Gd ($D_s/M_s = 0.2 \times 10^{-8} J/(mA)$) and for GdCo(4nm) (+1.5cm), for which D_s/M_st cannot be evaluated precisely but is expected to be larger than that of GdCo(4nm) (-1.5cm) because of the strong reduction of M_st.

6.5 Some unexplained effects

The study of these ferrimagnetic alloy films will have to be pursued. Several aspects of our study are still unclear.

6.5.1 Coercivity at the compensation composition

The coercivity is expected to increase and to diverge at the compensation composition where the magnetization tends to zero. In our thin layers of GdCo, the coercivity does not diverge, both for the measurements carried out by VSM-SQUID and the ones measured by Kerr microscopy. One possible explanation is the inhomogeneity of the films. If the film is inhomogeneous, it might be possible that nucleation of reversed domains takes place in a region away from the compensation region. However this appears to be in contradiction with the results of our measurements of DW speed vs. Hz field, where the domain propagation is clearly observed to become more and more difficult as the compensation is approached.

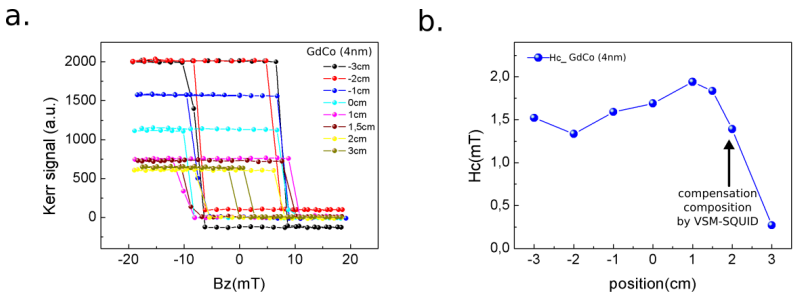

Fig. 6.16: **a.** Hysteresis loops measured by magneto-optical Kerr effect in different positions of the sample GdCo (4nm). **b.** curve of coercive field of the same sample.

6.5.2 Kerr signal across compensation composition

For GdCo alloys, the Kerr signal in the visible and infrared spectrum has been shown to be mainly sensitive to the Co sublattice [Sat83]. For this reason we would expect

that the Kerr contrast would change sign when going across the compensation composition. This has been observed for example in A. Hrabec thesis [Hra11] for 30 nm thick GdCo alloys (see Figure 6.17). The Kerr image has been taken after the application of a 500 mT field. At the compensation composition, at the middle of the image, the change of contrast is very clear. On the left of the image (Co rich side) the contrast is clear corresponding to the magnetization parallel to the field; on the right part the magnetization, dominated by the Gd, is antiparallel to the field and the contrast is dark.

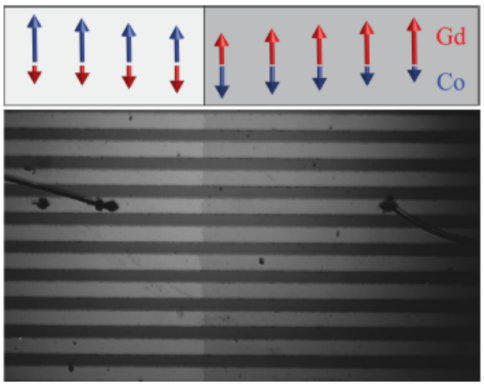

Fig. 6.17: Kerr microscopy images of the GdCo wires and sketch of the corresponding Gd and Co magnetic moments. Image taken after application of a 500 mT positive magnetic field. The compensation interface becomes visible. Image from [Hra11].

This is not the case in our thin samples. Figure 6.16 (the same of the previous session) shows that the hysteresis curves do not change sign when going across the compensation composition. Moreover, the amplitude of the Kerr signal changes with the GdCo alloy composition, which is also unexpected (see Figure 6.17). We attribute these effects to the fact that the Kerr signal is mainly dictated to optical effects, and in a minor fashion to the magnetization of our samples. Nevertheless, we plan to carry out a more detailed study of the Kerr signal as a function of source (all our data were taken with 630 nm red diode, and 430 nm and white sources will also be considered) and of film thickness.

6.6 Summary

The main conclusion of this preliminary study is that both the field and the current-driven domain wall speeds can be largely enhanced in trilayer stacks with DMI, by tuning the net magnetization of the ferro/ferrimagnetic layer. While in the case of field-driven dynamics, the decrease of M_s implies that larger (or very large) fields are needed to obtain saturation velocities (in the limit of compensated ferrimagnet the DWs cannot be longer moved by a magnetic field), DWs can be moved very efficiently for weak current densities when the magnetization is reduced.

The largest DW speeds measured for the Pt/GdCo/Ta samples are of the same order of magnitude as those of the Pt/Co/Gd(GdOx or AlOx) samples. We had anticipated that much larger speeds could be obtained by reducing the net magnetization in this samples. We found instead that the decrease of M_s cannot totally express itself into a super-efficient SOT because of the decrease of the interfacial DMI.

This strong reduction of the DMI strength was unexpected. The understanding of this phenomenon, and how a reduction of only a few % of the alloy composition can change the DMI by a factor almost 2, will be the subject of future studies. We will in particular deepen the understanding of the homogeneity of the layer composition and the possibility to have a gradient of Gd content as a function of thickness. A first test will be to deposit a thin Co layer on top of the Pt layer, in order to keep a strong interfacial DMI value.

Our results, and in particular the $1/M_s$ dependence of the SOT torque efficiency and the decrease of the depinning current densities, gives a contribution in favor of the argument that the spin-orbit torque is exerted on the net magnetization of the ferro/ferrimagnetic layer and not on the magnetization of the Co sublattice.

7 Conclusion and perspectives

The aim of this thesis was to study the dynamics of chiral domain walls in non-centrosymmetric multilayer films with perpendicular magnetic anisotropy grown by magnetron sputtering. In these systems, the domains walls can acquire a Néel internal structure with fixed chirality stabilized by interfacial Dzyaloshinskii-Moriya interaction (DMI). We have shown that these domain walls can be driven to very large speeds by magnetic field or current.

One of our achievements has been to demonstrate two methods to extract the DMI strength from the study of the field-driven dynamics of chiral Néel walls. The first was already used by others authors [Je+13; Hra+14] and consists in studying the anisotropic expansion of domains in the presence of an in-plane magnetic field. Previous studies [Vaň+15; Lav+15] had however shown that the simplified extension of the creep theory developed by [Je+13] cannot always describe the DW behavior in the presence of an in-plane field. This is why our choice had been to apply this method in the flow regime (high applied magnetic fields) where the DW speed is simply related to the domain width and not in the creep regime where the in-plane field acts on the DW energy. In [Vaň+15] we had indeed shown that the H_{DMI} field obtained with this method is the same, whether the magnetic field or the electrical current drives the DW displacement. The drawback of this method remains however that it relies on the knowledge of the exchange stiffness A, which is in general difficult to measure in thin films. In our study, we have used the value A=16 pJ/s which was found by Metaxas *et al.* [Met+07] for Co films of similar thicknesses. We have also verified for some samples that this value leads to DMI strengths similar to those obtained with Brillouin Light Scattering spectroscopy, which does not requires the knowledge of A.

In most of the Pt/Co/MOx samples studied in this work, the flow regime is reached for fields of the order of 100 mT, where the domain wall speeds can reach 100 m/s or more. To be studied by Kerr microscopy, where the typical field of view is a few 100 μm, short pulses typically in the nanosecond range, are needed. Indeed for a speed of e.g. 100m/s the DW moves by 100um in 1us, making the experiment possible in the microsecond range only in the case of very low domain nucleation density. Our original set-up, consisting of microcoils of diameter 200 μm associated to fast current generators (developed with the help of M. Bonfim from University

of Paraná in Brazil) allows us to reach fields up to 700 mT with current pulses as short as 10 ns. With this set-up, the flow regime is easily accessible. Thanks to this set-up, we have been able to propose a second original method to measure the DMI strength. First of all, we decided to explore the domain wall speed in three samples, one symmetric (Pt/Co/Pt) and two asymmetric stacks (Pt/Co/Gd and Pt/Co/GdOx), since it was known from previous works [Piz+14] that Pt/Co interface gives rise to a strong DMI. In both cases, the samples presented perpendicular magnetic anisotropy. In the symmetric sample we observed relatively low speeds (60 m/s for 200 mT) as expected for Bloch domain walls in the precessional flow regime, and as already observed by Metaxas *et al.* [Met+07]. In the asymmetric samples (Pt/Co/Gd and Pt/Co/GdOx) the domain walls reach much larger speeds for high fields (respectively 600 m/s and 300 m/s for 200 mT) consistent with the fact that in these samples the interfacial DMI stabilizes chiral Néel walls and the Walker field is shifted towards larger fields. Surprisingly, the DW speed was observed to saturate at the value expected for the Walker field, in disagreement with 1D models, but in agreement with 2D micromagnetic simulations allowing the formation of Bloch lines within the domain walls. The strong difference observed between the saturation speed in Pt/Co/GdOx and Pt/Co/Gd, where the DMI strength was found to be similar, can be related to the large difference in spontaneous magnetization, in agreement with the analytical expression of the Walker speed : $v_w = \gamma \pi D/2M_s$. Through this formula, the measurement of the saturation velocity can provide a way to access to the DMI strength that requires only the knowledge of the spontaneous magnetization. In this work, we have found that the difference between the interfacial DMI values obtained with the two methods by fixing A=16 pJ/m is always less than 0.2 pJ/m, which fixes the uncertainty of the determination of the DMI. It is also important to notice that the Walker field is often hidden by the creep regime, in the case of strong pinning. Nevertheless, the saturation of the velocity after Hw allows us to obtain the DMI strength.

The study reported in Chapter 4, together with previous works of the Institut Néel team in collaboration with SPINTEC and Laboratoire de Physique de Solide, allowed us to confirm that the DMI strengths in Pt/Co/MOx samples is large, actually the largest found so far in all the explored materials. While the presence of large DMI at the Pt/Co interface has been predicted by *ab initio* calculations and has been confirmed by several studies, the case of the Co/oxide interface was largely unexplored, although some *ab initio* calculations have predicted that this could be at the origin of a DMI contribution.

In Chapter 5, we have proposed to study the dependence of the interfacial DMI in a series of Pt/Co/MOx with (M=Al or Gd) trilayers with a different degree of the oxidation at the Co/MOx interface. We compared the effective DMI strength in different positions of the sample, that correspond to different degrees of oxidation of

the Co top interface and we have reported the relation with the magnetic anisotropy energy. We found that the optimum coverage of the top Co interface with oxygen not only determines the maximum anisotropy but also optimizes the interfacial DMI. Also, we observed that the DMI increases going from the underoxidized to the optimum oxidation region which confirms that at the Co/O interface it has the same sign as at the Pt/Co interface. Following suggestions form the literature, the Rashba-based theory may provide a common ground to explain the simultaneous increase of the DMI and the PMA at the Co/oxide interface in our samples.

Following the results reported in Chapter 4, showing the larger DW velocity in the Pt/Co/Gd sample due to the reduced magnetization, in Chapter 6 we have reported the preliminary study of the domain wall motion in Pt/GdCo/Ta thin films. In GdCo alloys the magnetic properties are strongly dependent on temperature or composition. In our work the Gd_xCo_{1-x} thin films with a gradient of composition were prepared by magnetron sputtering in such a way that the compensation composition at room temperature, is located within the sample. The variation of the composition (by around 3%) changes strongly the magnetization along the sample, so that the study of domain wall dynamics in different positions can address the effect of varying magnetization. We could then show that while in the case of field-driven dynamics, domain walls need very large field to obtain saturation speeds when M_s decreases towards the compensation composition, when driven by electrical current the domains wall move very efficiently and this because the SOT scales as the inverse of the on the net magnetization of the ferro/ferrimagnetic layer.

The interfacial DMI strength in the Pt/GdCo/Ta samples was found to be strongly reduced with respect to that of the Pt/Co/MOx or Pt/Co/Gd samples. The fundamental reasons of this effect still have to be studied. How does the Levi-Fert model apply in the case where some of the 3d spins are substituted by 4f spins strongly exchange coupled to the 3d spin? This could be only addressed by *ab-initio* calculations. From an experimental viewpoint, alloys with increasing amount of Gd going from pure Co to the $Co_{72}Gd_{28}$ alloys studied here could also be studied. This would allow to see whether the decreased DMI is due to the decreased M_s or the decreased number of Pt-Co bonds at the bottom Co interface. This approach might reveal very time consuming. Another route that can be easily pursued is to deposit a very thin layer of Co on top of Pt, before depositing the GdCo layer. A strong increase of the DMI should indicate that indeed the interfacial structure is primarily dictating the interfacial DMI strength.

Recovering a large DMI at the Pt/GdCo interface should allow us to obtain very efficient SOT induced DW motion in these ferrimagnetic alloys. Indeed, the SOT efficiency found in this work is already similar to that found for Pt/Co/AlOx with large DMI and much thinner Co layers. This might reveal to be very interesting for

applications, considering also the strong reduction of the depinning current that we have observed in our studies.

A few groups in the world start indeed working on ferrimagnetic thin layers (especially GdCo and GdCoFe) because of the strong potentials for applications. Kim *et al.* [Kim+17] have found very large field driven DW speeds when passing the angular momentum compensation. Unpublished work by Beach group in MIT also shown very efficient SOT induced domain wall motion in GdCo layers with a maximum at the angular moment compensation. Note that in our work, too few alloy compositions have been studied so far, which makes it impossible to conclude whether the maximum of the velocity is obtained at the angular moment compensation or at the magnetization compensation.

One of the most important results of our work has been to experimentally demonstrate the relation between the domain wall saturation velocity in samples with large DMI, and the DMI strength via the relation $v_{sat} \propto D/M_s$ (Equation 4.5). Note however that this relation has to be applied with caution. Some of the micromagnetic simulations carried out during the Master internship of Viola Krizakova in 2017 in our group are shown in the figure below. The initial parameters (D, M_s, A, Ku, alpha) are the ones of the Pt/Co/GdOx sample described in Chapter 4. The DMI strength and the saturation magnetization have then been varied to study the impact on the DW speeds.

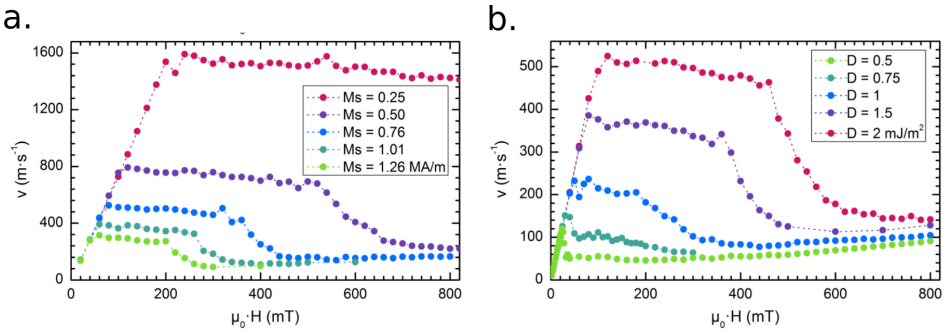

Fig. 7.1: Field-driven DW velocity for **a.** fixed D = 1.5 mJ/m^2, K_{eff} = 1.44 MJ/m^3 and varying saturation magnetization. **b.** M_s = 1.01MA/m, K_{eff} = 1.44 MJ/m^3 and different values of DMI strength (in mJ/m^2)

We can see that the M_s and D value have an impact on the saturation DW speed, but also on the extension of the "velocity plateau" after the Walker field. The length of the plateau is also changing as D/M_s, the largest plateau being present in samples with large DMI and smaller M_s. Particularly noteworthy is the case of samples with large M_s and small D (see for ex. the case of M_s=1.01 MA/m and D = 0.5 mJ/m^2). In this case the Walker velocity is around 130 m/s, the Walker field is 30 mT but the plateau has disappeared, so that the Walker breakdown occurs at very low fields. In samples having these parameters care should be taken to extract the DMI from

the plateau velocity. Indeed if the pinning is strong and the creep regime extends beyond the Walker field, the plateau velocity will be found in the precessional regime. The application of the formula in eq. 4.5 will then give rise to an underestimation of the DMI strength. We have verified that this is not the case for the data presented in Chapter 6 for GdCo layers, where the DMI strength is small indeed, but the reduced M_s recovers a long plateau of velocity. In this sense, in our experience it is always an advantage to carry out both the speed-vs-H_z and the speed-vs-H_x measurements and verify the consistency of the results (if the correct value of the exchange stiffness has been clearly established).

Skyrmions

Another issue that has not been treated in this manuscript is the statics and dynamics of skyrmion bubbles that may be stabilized in the systems with PMA and DMI described before. The stability conditions depend critically on the material parameters: magnetic anisotropy, exchange interaction, DMI and dipolar energy. In trilayer structures like the one discussed above, both the magnetic anisotropy and the DMI are interface effects, and their strength can thus be tuned by changing the magnetic layer thickness. Using Kerr microscopy, colleges in my team have observed that in Pt/Co/AlOx [Sch+17], Pt/Co/MgO [Jug+17] and Pt/Co/TbOx (unpublished work) films with a controlled thickness gradient of the Al or Tb layers, a thickness region exists where a phase with alternating stripes of up and down magnetization is stable at room temperature, and can be transformed into a phase containing isolated skyrmionic bubbles when applying small (0.1-5 mT) out-of-plane magnetic field H_z. The Figure 7.2 shows such magnetic configurations measured by Kerr microscopy for a Pt/Co(1nm)TbOx(2.8-3nm) film. In the absence of H_z field, a stripe domain structure with period changing along the gradient direction can be clearly seen. When a weak field is applied, such stripes transform into bubbles having decreasing radius as the anisotropy decreases (Tb thickness increases). Outside the field of view of the images, the bubbles become too small to be distinguished with Kerr microscopy, whose resolution is of the order of 600 nm. The evolution of the skyrmion size versus temperature is the subject of a project that has been accepted for beamtime at the synchroron Bessy in Germany, where the domain structure will be observated with Photoelectron Emission Spectroscopy associated to XMCD (XMCD-PEEM).

Using XMCD-PEEM microscopy, we observed a similar effect in Pt/Co(1nm)/MgO thin layers, in the frame of a collaboration with O. Boulle from SPINTEC in which I have been strongly involved during my PhD. In this case, we have demonstrated that the size of the bubble can be tuned by adjusting the size of the magnetic strips

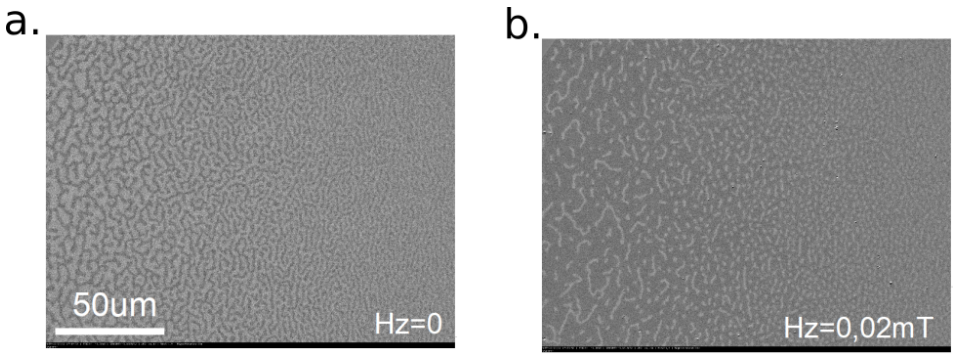

Fig. 7.2: Stripe domains observed at remanence in Pt/Co/TbOx **a.** transform into skyrmionic bubbles for very weak fields **b.** Images are taken with Kerr microscopy.

that confine them, and skyrmionic bubbles of sub-100 nm size can be observed in 300 nm wide strips.

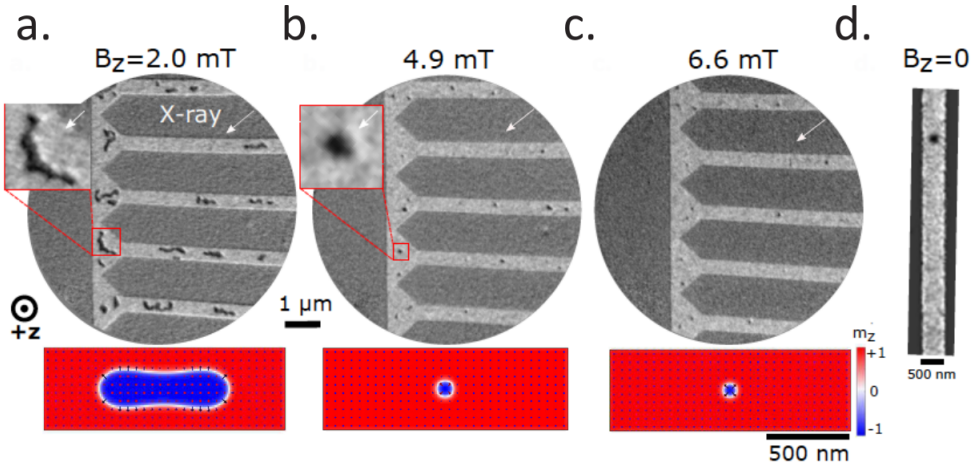

Fig. 7.3: Domains in 500 nm wide stripes in Pt/Co(1nm)/MgO trilayers transform into bubbles in the presence of small out-of-plane fields. These images have been taken using a XMCD-PEEM microscope at the CIRCE beamline of the Alba synchrotron in Barcelona.

One important property of magnetic imaging using XMCD-PEEM is that the magnetic contrast is proportional to the projection of the magnetization along the X-ray propagation direction. This, together with the high spatial resolution of the XMCD-PEEM technique, allowed us to show for the first time using direct magnetic imaging, the left handed chirality of domain walls and skyrmions in Pt/Co/MOx trilayers [Bou+16] (Figure 7.4).

In Pt/Co/AlOx, we observed that the skyrmion bubbles can be displaced by electrical current by SHE-SOT effect. However the skyrmions are strongly pinned by defects and nucleations and annihilations of skyrmion bubbles are observed as well as skyrmion displacements . A similar effect is observed in Pt/Co/MgO that we have studied at synchrotron radiation sources.

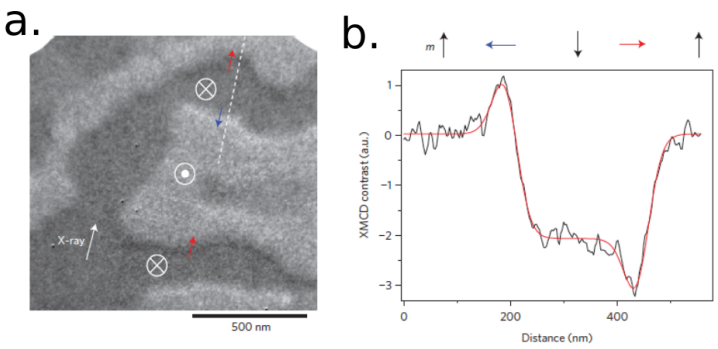

Fig. 7.4: Imaging of the chiral Néel structure of domain walls using XMCD-PEEM magnetic microscopy. **a.** Magnetic image of a multidomain state in the continuous Pt/Co/MgO film. For DWs lying perpendicular to the X-ray beam direction, thin white and black lines can be seen, corresponding to the magnetization being aligned antiparallel and parallel to the photon beam respectively. **b.** Line scan of the magnetic contrast corresponding to the dotted white line in (a). Image from [Bou+16].

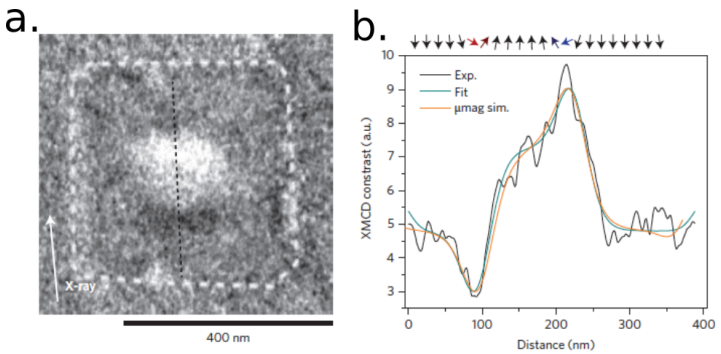

Fig. 7.5: Magnetic skyrmion observed at room temperature and zero applied external magnetic field **a.** XMCD- PEEM image of a 420 nm square dot (indicated by the dotted line) and **b.** line scan along the dotted black line (black line). The line scan has been averaged perpendicularly to the linescan over 30 nm. Image from [Bou+16].

The perspectives of this work will be to engineer materials in which the magnetic skyrmions will move with less pinning. Since for applications to spintronic devices the skyrmion size will have to be reduced with respect to the micron sizes observed in our systems, one of the envisaged routes in the team is to stabilize skyrmions in the GdCo films described in Chapter 6. For these samples the magnetization can be strongly reduced, leading to a reduction of the dipolar energy that stabilizes large skyrmions (skyrmionic bubbles). Together with the reduction of the DMI, small skyrmions can be expected in these systems.

Bibliography

[Aje+17] Fernando Ajejas, Viola Křižáková, Dayane de Souza Chaves, et al. “Tuning domain wall velocity with Dzyaloshinskii-Moriya interaction”. In: *Applied Physics Letters* 111.20 (2017), p. 202402 (cit. on pp. 83, 84).

[Bar+14] Stewart E Barnes, Jun’ichi Ieda, and Sadamichi Maekawa. “Rashba spin-orbit anisotropy and the electric field control of magnetism”. In: *Scientific reports* 4 (2014), p. 4105 (cit. on p. 85).

[BB32] Felix Bloch and Felix Bloch. *Zur theorie des austauschproblems und der remanenzerscheinung der ferromagnetika*. Springer, 1932 (cit. on p. 11).

[Bel+15] Mohamed Belmeguenai, Jean-Paul Adam, Yves Roussigné, et al. “Interfacial Dzyaloshinskii-Moriya interaction in perpendicularly magnetized Pt/Co/AlO x ultrathin films measured by Brillouin light spectroscopy”. In: *Physical Review B* 91.18 (2015), p. 180405 (cit. on p. 43).

[Bel+16] Abderrezak Belabbes, G Bihlmayer, F Bechstedt, S Blügel, and Aurelien Manchon. “Hund’s Rule-Driven Dzyaloshinskii-Moriya Interaction at 3 d- 5 d Interfaces”. In: *Physical review letters* 117.24 (2016), p. 247202 (cit. on pp. 67, 84).

[Ber+17] N Bergeard, A Mougin, M Izquierdo, E Fonda, and F Sirotti. “Correlation between structure, electronic properties, and magnetism in Co x Gd 1-x thin amorphous films”. In: *Physical Review B* 96.6 (2017), p. 064418 (cit. on p. 94).

[Ber74] L Berger. “Prediction of a domain-drag effect in uniaxial, non-compensated, ferromagnetic metals”. In: *Journal of Physics and Chemistry of Solids* 35.8 (1974), pp. 947–956 (cit. on p. 22).

[Bon01] Marlio Bonfim. “Micro bobines à champ pulsé: applications aux champs forts et à la dynamique de renversement de l’aimantation à l’échelle de la nanoseconde par effet Kerr et Dichroïsme Circulaire Magnétique de rayons X”. PhD thesis. Université Joseph-Fourier-Grenoble I, 2001 (cit. on p. 37).

[Bou+16] Olivier Boulle, Jan Vogel, Hongxin Yang, et al. “Room-temperature chiral magnetic skyrmions in ultrathin magnetic nanostructures”. In: *Nature nanotechnology* 11.5 (2016), p. 449 (cit. on pp. 18, 77, 84, 85, 112, 113).

[BRU10] BRUKER. “Good Diffraction Practice Webinar Series - X-ray Reflectometry”. In: *BRUKER* (2010) (cit. on p. 33).

[Bru93] P Bruno. “Physical origins and theoretical models of magnetic anisotropy”. In: *Magnetismus von Festkörpern und grenzflächen* 24 (1993), pp. 1–28 (cit. on pp. 7, 8).

[Cha+00] Pascal Chauve, Thierry Giamarchi, and Pierre Le Doussal. “Creep and depinning in disordered media”. In: *Physical Review B* 62.10 (2000), p. 6241 (cit. on p. 51).

[Col+08] P Colombi, DK Agnihotri, VE Asadchikov, et al. “Reproducibility in X-ray reflectometry: results from the first world-wide round-robin experiment”. In: *Journal of Applied Crystallography* 41.1 (2008), pp. 143–152 (cit. on p. 33).

[DB+91] FJA Den Broeder, W Hoving, and PJH Bloemen. “Magnetic anisotropy of multilayers”. In: *Journal of magnetism and magnetic materials* 93 (1991), pp. 562–570 (cit. on p. 10).

[Dzy57] IE Dzyaloshinskii. “Thermodynamic theory of weak ferromagnetism in antiferromagnetic substances”. In: *Soviet Physics Jetp-Ussr* 5.6 (1957), pp. 1259–1272 (cit. on p. 19).

[Dzy60] IE Dzyaloshinskii. “On the magneto-electrical effect in antiferromagnets”. In: *Soviet Physics Jetp-Ussr* 10.3 (1960), pp. 628–629 (cit. on p. 18).

[Emo+14] Satoru Emori, Eduardo Martinez, Kyung-Jin Lee, et al. “Spin Hall torque magnetometry of Dzyaloshinskii domain walls”. In: *Physical Review B* 90.18 (2014), p. 184427 (cit. on p. 23).

[Far46] Michael Faraday. “Experimental researches in electricity. Nineteenth series”. In: *Philosophical Transactions of the Royal Society of London* 136 (1846), pp. 1–20 (cit. on p. 35).

[Fer+13] Albert Fert, Vincent Cros, and João Sampaio. “Skyrmions on the track”. In: *Nature nanotechnology* 8.3 (2013), pp. 152–156 (cit. on pp. 18, 19).

[FL16] Joseph Finley and Luqiao Liu. “Spin-orbit-torque efficiency in compensated ferrimagnetic cobalt-terbium alloys”. In: *Physical Review Applied* 6.5 (2016), p. 054001 (cit. on p. 88).

[FL80] A Fert and Peter M Levy. “Role of anisotropic exchange interactions in determining the properties of spin-glasses”. In: *Physical Review Letters* 44.23 (1980), p. 1538 (cit. on p. 19).

[Fon96] S Foner. “The vibrating sample magnetometer: Experiences of a volunteer”. In: *Journal of applied physics* 79.8 (1996), pp. 4740–4745 (cit. on p. 40).

[Gar+11] Houmed Garad, Luc Ortega, Aline Y Ramos, et al. “The contribution of x-ray specular reflectometry to the oxygen-induced magnetic properties in Pt/Co/AlO x”. In: *Journal of Applied Physics* 109.7 (2011), p. 07C117 (cit. on p. 34).

[Gui09] Alberto Passos Guimarães. *Principles of nanomagnetism*. Vol. 7. Springer, 2009 (cit. on p. 12).

[Han+89] P Hansen, C Clausen, G Much, M Rosenkranz, and K Witter. "Magnetic and magneto-optical properties of rare-earth transition-metal alloys containing Gd, Tb, Fe, Co". In: *Journal of applied physics* 66.2 (1989), pp. 756–767 (cit. on pp. 91, 95).

[Hei+08] M Heide, G Bihlmayer, and S Blügel. "Dzyaloshinskii-Moriya interaction accounting for the orientation of magnetic domains in ultrathin films: Fe/W (110)". In: *Physical Review B* 78.14 (2008), p. 140403 (cit. on p. 20).

[Hei+11] Stefan Heinze, Kirsten Von Bergmann, Matthias Menzel, et al. "Spontaneous atomic-scale magnetic skyrmion lattice in two dimensions". In: *Nature Physics* 7.9 (2011), p. 713 (cit. on pp. 18, 20).

[Hra+14] A Hrabec, NA Porter, A Wells, et al. "Measuring and tailoring the Dzyaloshinskii-Moriya interaction in perpendicularly magnetized thin films". In: *Physical Review B* 90.2 (2014), p. 020402 (cit. on pp. 51, 65, 107).

[Hra11] Ales Hrabec. "Domain wall dynamics in magnetic nanostructures: Effect of magnetic field and electric current". PhD thesis. Université de Grenoble, 2011 (cit. on pp. 90, 91, 105).

[HS08] Alex Hubert and Rudolf Schäfer. *Magnetic domains: the analysis of magnetic microstructures*. Springer Science & Business Media, 2008 (cit. on pp. 15, 36).

[Je+13] Soong-Geun Je, Duck-Ho Kim, Sang-Cheol Yoo, et al. "Asymmetric magnetic domain-wall motion by the Dzyaloshinskii-Moriya interaction". In: *Physical Review B* 88.21 (2013), p. 214401 (cit. on pp. 51, 52, 65, 107).

[Je+18] Soong-Geun Je, Juan-Carlos Rojas-Sánchez, Thai Ha Pham, et al. “Spin-orbit torque-induced switching in ferrimagnetic alloys: Experiments and modeling”. In: *Applied Physics Letters* 112.6 (2018), p. 062401 (cit. on p. 88).

[Joh+96] MT Johnson, PJH Bloemen, FJA Den Broeder, and JJ De Vries. “Magnetic anisotropy in metallic multilayers”. In: *Reports on Progress in Physics* 59.11 (1996), p. 1409 (cit. on p. 9).

[Jos62] Brian David Josephson. “Possible new effects in superconductive tunnelling”. In: *Physics letters* 1.7 (1962), pp. 251–253 (cit. on p. 41).

[Jug+17] Roméo Juge, Soong-Geun Je, Dayane de Souza Chaves, et al. “Magnetic skyrmions in confined geometries: effect of the magnetic field and the disorder”. In: *Journal of Magnetism and Magnetic Materials* (2017) (cit. on p. 111).

[Kat+78] T Katayama, K Hasegawa, K Kawanishi, and T Tsushima. “Annealing effects on magnetic properties of amorphous GdCo, GdFe, and GdCoMo films”. In: *Journal of Applied Physics* 49.3 (1978), pp. 1759–1761 (cit. on pp. 99, 100).

[Kie31] Heinz Kiessig. “Untersuchungen zur totalreflexion von röntgenstrahlen”. In: *Annalen der Physik* 402.6 (1931), pp. 715–768 (cit. on p. 34).

[Kim+13] Kyoung-Whan Kim, Hyun-Woo Lee, Kyung-Jin Lee, and Mark D Stiles. “Chirality from interfacial spin-orbit coupling effects in magnetic bilayers”. In: *Physical review letters* 111.21 (2013), p. 216601 (cit. on p. 85).

[Kim+17] Kab-Jin Kim, Se Kwon Kim, Yuushou Hirata, et al. “Fast domain wall motion in the vicinity of the angular momentum compensation temperature of ferrimagnets”. In: *Nature materials* 16.12 (2017), p. 1187 (cit. on p. 110).

[Kuc+15] Wolfgang Kuch, Rudolf Schäfer, Peter Fischer, and Franz Ulrich Hillebrecht. *Magnetic microscopy of layered structures*. Springer, 2015 (cit. on p. 35).

[Lav+15] Reinoud Lavrijsen, DMF Hartmann, A Van Den Brink, et al. "Asymmetric magnetic bubble expansion under in-plane field in Pt/Co/Pt: Effect of interface engineering". In: *Physical Review B* 91.10 (2015), p. 104414 (cit. on pp. 52, 107).

[LF+13] V López-Flores, N Bergeard, V Halté, et al. "Role of critical spin fluctuations in ultrafast demagnetization of transition-metal rare-earth alloys". In: *Physical Review B* 87.21 (2013), p. 214412 (cit. on p. 49).

[Man+08] A Manchon, Stefania Pizzini, Jan Vogel, et al. "X-ray analysis of the magnetic influence of oxygen in Pt/ Co/ Al O x trilayers". In: *Journal of Applied Physics* 103.7 (2008), 07A912 (cit. on pp. 67, 68, 77, 82, 85).

[Man+18] Aurelien Manchon, IM Miron, T Jungwirth, et al. "Current-induced spin-orbit torques in ferromagnetic and antiferromagnetic systems". In: *arXiv preprint arXiv:1801.09636* (2018) (cit. on p. 43).

[Mau+14] DK Maurya, Ali Sardarinejad, and Kamal Alameh. "Recent developments in RF magnetron sputtered thin films for pH sensing applications—An overview". In: *Coatings* 4.4 (2014), pp. 756–771 (cit. on p. 28).

[Met+07] PJ Metaxas, JP Jamet, A Mougin, et al. "Creep and flow regimes of magnetic domain-wall motion in ultrathin Pt/Co/Pt films with perpendicular anisotropy". In: *Physical review letters* 99.21 (2007), p. 217208 (cit. on pp. 16, 51, 56, 58, 107, 108).

[Mir+11] Ioan Mihai Miron, Thomas Moore, Helga Szambolics, et al. "Fast current-induced domain-wall motion controlled by the Rashba effect". In: *Nature materials* 10.6 (2011), pp. 419–423 (cit. on pp. 3, 23, 25, 59, 67, 98, 101–103).

[Mis+17] Rahul Mishra, Jiawei Yu, Xuepeng Qiu, et al. “Anomalous current-induced spin torques in ferrimagnets near compensation”. In: *Physical review letters* 118.16 (2017), p. 167201 (cit. on p. 88).

[Mis99] Kurt Mislow. “Molecular chirality”. In: *Top. Stereochem* 22 (1999), pp. 1–82 (cit. on p. 18).

[Mor60] Tôru Moriya. “Anisotropic superexchange interaction and weak ferromagnetism”. In: *Physical Review* 120.1 (1960), p. 91 (cit. on pp. 18, 19).

[Mou+07] Alexandra Mougin, M Cormier, JP Adam, PJ Metaxas, and J Ferré. “Domain wall mobility, stability and Walker breakdown in magnetic nanowires”. In: *EPL (Europhysics Letters)* 78.5 (2007), p. 57007 (cit. on p. 16).

[Nis11] Lavinia Nistor. “Jonctions tunnel magnétiques à aimantation perpendiculaire: anisotropie, magnétorésistance, couplages magnétiques et renversement par couple de transfert de spin”. PhD thesis. Université de Grenoble, 2011 (cit. on p. 9).

[OS72] J Orehotsky and K Schröder. “Magnetic Properties of Amorphous Fe x Gd y Alloy Thin Films”. In: *Journal of Applied Physics* 43.5 (1972), pp. 2413–2418 (cit. on p. 91).

[Par+03] Stuart Parkin, Xin Jiang, Christian Kaiser, et al. “Magnetically engineered spintronic sensors and memory”. In: *Proceedings of the IEEE* 91.5 (2003), pp. 661–680 (cit. on p. 5).

[Par+08] Stuart SP Parkin, Masamitsu Hayashi, and Luc Thomas. “Magnetic domain-wall racetrack memory”. In: *Science* 320.5873 (2008), pp. 190–194 (cit. on pp. 2, 22, 23).

[Par+99] SSP Parkin, KP Roche, MG Samant, et al. “Exchange-biased magnetic tunnel junctions and application to nonvolatile magnetic random access memory”. In: *Journal of Applied Physics* 85.8 (1999), pp. 5828–5833 (cit. on p. 5).

[Par54] Lyman G Parratt. “Surface studies of solids by total reflection of X-rays”. In: *Physical review* 95.2 (1954), p. 359 (cit. on p. 34).

[Pha+16] Thai Ha Pham, J Vogel, J Sampaio, et al. “Very large domain wall velocities in Pt/Co/GdOx and Pt/Co/Gd trilayers with Dzyaloshinskii-Moriya interaction”. In: *EPL (Europhysics Letters)* 113.6 (2016), p. 67001 (cit. on pp. 56, 62, 63, 77).

[Piz+14] Stefania Pizzini, Jan Vogel, Stanislas Rohart, et al. “Chirality-induced asymmetric magnetic nucleation in Pt/Co/AlO x ultrathin microstructures”. In: *Physical review letters* 113.4 (2014), p. 047203 (cit. on pp. 43, 108).

[PY15] Stuart Parkin and See-Hun Yang. “Memory on the racetrack”. In: *Nature nanotechnology* 10.3 (2015), pp. 195–198 (cit. on p. 3).

[Riz+13] ND Rizzo, D Houssameddine, J Janesky, et al. “A fully functional 64 Mb DDR3 ST-MRAM built on 90 nm CMOS technology”. In: *IEEE Transactions on Magnetics* 49.7 (2013), pp. 4441–4446 (cit. on p. 22).

[Ros+17] Niklas Roschewsky, Charles-Henri Lambert, and Sayeef Salahuddin. “Spin-orbit torque switching of ultralarge-thickness ferrimagnetic GdFeCo”. In: *Physical Review B* 96.6 (2017), p. 064406 (cit. on p. 88).

[Ryu+13] Kwang-Su Ryu, Luc Thomas, See-Hun Yang, and Stuart Parkin. “Chiral spin torque at magnetic domain walls”. In: *Nature nanotechnology* 8.7 (2013), pp. 527–533 (cit. on pp. 3, 23).

[SA00] J Stohr and Simone Anders. “X-ray spectro-microscopy of complex materials and surfaces”. In: *IBM Journal of Research and Development* 44.4 (2000), pp. 535–551 (cit. on p. 42).

[Sat83] K Sato. “K. Sato and Y. Togami, J. Magn. Magn. Mater. 35, 181 (1983).” In: *J. Magn. Magn. Mater.* 35 (1983), p. 181 (cit. on p. 104).

[Sch+17] Marine Schott, Anne Bernand-Mantel, Laurent Ranno, et al. “The skyrmion switch: turning magnetic skyrmion bubbles on and off with an electric field”. In: *Nano letters* 17.5 (2017), pp. 3006–3012 (cit. on p. 111).

[Sch+87] G Schütz, W Wagner, Wr Wilhelm, et al. “Absorption of circularly polarized x rays in iron”. In: *Physical Review Letters* 58.7 (1987), p. 737 (cit. on p. 42).

[Sim12] Raymond W Simmonds. “Thermal physics: quantum interference heats up”. In: *Nature* 492.7429 (2012), pp. 358–359 (cit. on p. 41).

[Slo72] JC Slonczewski. “Dynamics of magnetic domain walls”. In: *AIP Conference Proceedings*. Vol. 5. 1. AIP. 1972, pp. 170–174 (cit. on p. 15).

[SM06] Mark D Stiles and Jacques Miltat. “Spin-transfer torque and dynamics”. In: *Spin dynamics in confined magnetic structures III*. Springer, 2006, pp. 225–308 (cit. on p. 25).

[SS16] Ivan Soldatov and Rudolf Schäfer. “Selective sensitivity in Kerr microscopy”. In: *arXiv:1612.02027* (2016) (cit. on p. 36).

[Stö99] J Stöhr. “Exploring the microscopic origin of magnetic anisotropies with X-ray magnetic circular dichroism (XMCD) spectroscopy”. In: *Journal of Magnetism and Magnetic Materials* 200.1 (1999), pp. 470–497 (cit. on pp. 6, 8).

[Swa88] S Swann. “Magnetron sputtering”. In: *Physics in technology* 19.2 (1988), p. 67 (cit. on p. 29).

[Thi+12] André Thiaville, Stanislas Rohart, Émilie Jué, Vincent Cros, and Albert Fert. “Dynamics of Dzyaloshinskii domain walls in ultrathin magnetic films”. In: *EPL (Europhysics Letters)* 100.5 (2012), p. 57002 (cit. on pp. 18, 20, 21, 25, 57, 59, 61, 62, 64, 88).

[Tho+92] BT Thole, Paolo Carra, F Sette, and Gerrit van der Laan. “X-ray circular dichroism as a probe of orbital magnetization”. In: *Physical Review Letters* 68.12 (1992), p. 1943 (cit. on p. 42).

[Ued+16] Kohei Ueda, Maxwell Mann, Chi-Feng Pai, Aik-Jun Tan, and Geoffrey SD Beach. “Spin-orbit torques in Ta/TbxCo100-x ferrimagnetic alloy films with bulk perpendicular magnetic anisotropy”. In: *Applied Physics Letters* 109.23 (2016), p. 232403 (cit. on p. 88).

[Van+14] Arne Vansteenkiste, Jonathan Leliaert, Mykola Dvornik, et al. “The design and verification of MuMax3”. In: *Aip Advances* 4.10 (2014), p. 107133 (cit. on p. 63).

[Vaň+15] M Vaňatka, Juan-Carlos Rojas-Sánchez, Jan Vogel, et al. “Velocity asymmetry of Dzyaloshinskii domain walls in the creep and flow regimes”. In: *Journal of Physics: Condensed Matter* 27.32 (2015), p. 326002 (cit. on pp. 51, 52, 56, 63, 65, 107).

[VK12] GE Volovik and M Krusius. “Chiral quantum textures”. In: *Physics* 5 (2012), p. 130 (cit. on p. 18).

[VT06] Sergio O Valenzuela and M Tinkham. “Direct electronic measurement of the spin Hall effect”. In: *Nature* 442.7099 (2006), p. 176 (cit. on p. 24).

[Was+04] Kiyotaka Wasa, Makoto Kitabatake, and Hideaki Adachi. *Thin film materials technology: sputtering of control compound materials*. Springer Science & Business Media, 2004 (cit. on p. 27).

[Wei07] Pierre Weiss. “L’hypothèse du champ moléculaire et la propriété ferromagnétique”. In: *J. phys. theor. appl.* 6.1 (1907), pp. 661–690 (cit. on p. 10).

[Wei08] P Weinberger. “John Kerr and his effects found in 1877 and 1878”. In: *Philosophical Magazine Letters* 88.12 (2008), pp. 897–907 (cit. on p. 35).

[Wel+95] D Weller, J Stöhr, R Nakajima, et al. “Microscopic origin of magnetic anisotropy in Au/Co/Au probed with x-ray magnetic circular dichroism”. In: *Physical Review Letters* 75.20 (1995), p. 3752 (cit. on p. 7).

[Yan+15] Hongxin Yang, André Thiaville, Stanislas Rohart, Albert Fert, and Mairbek Chshiev. “Anatomy of dzyaloshinskii-moriya interaction at Co/Pt interfaces”. In: *Physical review letters* 115.26 (2015), p. 267210 (cit. on p. 67).

[Yan+16] Hongxin Yang, Olivier Boulle, Vincent Cros, Albert Fert, and Mairbek Chshiev. “Controlling Dzyaloshinskii-Moriya interaction via chirality dependent layer stacking, insulator capping and electric field”. In: *arXiv preprint arXiv:1603.01847* (2016) (cit. on p. 84).

[Yan+17] Hongxin Yang, Gong Chen, Alexandre AC Cotta, et al. “Significant Dzyaloshinskii-Moriya Interaction at Graphene-Ferromagnet Interfaces due to Rashba-effect”. In: *arXiv preprint arXiv:1704.09023* (2017) (cit. on p. 67).

[Yos+16] Yoko Yoshimura, Kab-Jin Kim, Takuya Taniguchi, et al. “Soliton-like magnetic domain wall motion induced by the interfacial Dzyaloshinskii-Moriya interaction”. In: *Nature Physics* 12.2 (2016), pp. 157–161 (cit. on pp. 62–64).

List of Figures

List of Tables

Rèsumè

L'objectif de cette thèse a été d'étudier la dynamique de parois de domaines dans des couches minces magnétiques ayant anisotropie perpendiculaire, dans un empilement non-centrosymétrique. Dans ce type de système la compétition entre l'interaction d'échange de Heisenberg et un terme d'échange antisymétrique appelé interaction Dzyaloshinskii-Moriya interfaciale, favorise des textures magnétiques non colinéaires avec une chiralité définie, comme les parois de Néel chirales et les skyrmions. Dans ce travail nous nous sommes intéressés à la dynamique induite par un champ magnétique ou un courant électrique de parois Néel chirales dans une tricouches constituée d'une fine couche de cobalt déposée sur du platine, et recouverte par un oxyde. Nous avons démontré que la structure statique et la dynamique des parois est fortement impactée par la présence de la DMI. La DMI favorise une structure Néel avec une chiralité bien définie (plutôt que la structure de Bloch trouvé en général dans des systèmes symétriques). En comparant des parois dans Pt/Co/Pt (DMI=0) et Pt/Co/AlOx (DMI forte) nous avons montré que en la présence de DMI les parois de domaines peuvent être déplacées plus efficacement avec un champ magnétique. La stabilisation de la structure interne de la paroi par la DMI déplace le régime precessionnel à de plus hauts champs magnétiques et permet d'obtenir des vitesses importantes. En opposition à ce que prédisent les modèles 1D, nous montrons que en la présence de fort DMI la vitesse de paroi sature après le champ de Walker, et que la vitesse de saturation est proportionnelle au rapport entre la force de la DMI et l'aimantation à saturation (D/Ms). L'augmentation de la vitesse de saturation dans des systèmes avec faible Ms a été démontrée en comparant la dynamique de parois dans Pt/Co/GdOx et Pt/Co/Gd. Ceci implique aussi que en connaissant Ms, la mesure de la vitesse de saturation fournit une méthode originale pour quantifier l'interaction Dzyaloshinskii-Moriya interfaciale, comme nous montrons dans ce travail. Cette méthode a été utilisée pour mesurer la DMI dans des tricouches Pt/Co/AlOx avec oxydation variable de l'interface supérieure du Co. Nous montrons que en plus de la forte DMI de l'interface Pt/Co, l'interaction Co/oxyde contribue avec une DMI du même signe, la force de laquelle dépend du dégrée d'oxydation de l'interface. Nous observons aussi que cette DMI est proportionnelle à l'anisotropie magnétique perpendiculaire, ce qui suggère que les deux effets ont une origine commune. Pour finir, nous avons montré des résultats préliminaires de dynamique de parois induite par champ et courant dans des systèmes ferrimagnétiques GdCo. Si d'une part près de la compensation les parois de domaines

dans des tricouches Pt/GdCo/Ta peuvent être déplacées seulement avec des champs très forts, d'autre part le courant est très efficace et les courants de dépiégeage très faibles. Nous avons attribué cet effet à la dépendance en 1/Ms du couple de spin-orbite qui agit sur l'aimantation.

Abstract

The aim of this thesis has been to study domain wall dynamics in magnetic thin films with perpendicular magnetic anisotropy embedded in a non centrosymmetric stack. In this kind of system the competition between the symmetric Heisenberg exchange and an antisymmetric exchange term, called the interfacial Dzyaloshinskii-Moriya interaction (DMI), favours non collinear magnetic textures with a fixed chirality, like chiral Néel domain walls and skyrmions. In this work we have been interested in the field and current-driven dynamics of chiral Néel walls in trilayer stacks, typically consisting of a thin Co film deposited on Pt and capped with an oxide. We have shown that the statics and dynamics of a domain wall (DW) is strongly affected by the DMI. The DMI favours Néel internal structure (rather than the Bloch structure usually found in symmetric systems) with a fixed chirality. By comparing DWs in Pt/Co/Pt (no DMI) and Pt/Co/AlOx (strong DMI), we have shown that in the presence of DMI, DWs can be moved more efficiently by a magnetic field. The stabilization of the internal DW structure by the DMI allows the precessional regime to be pushed to large magnetic fields and large velocities to be reached. Opposite to what is predicted by 1D models we show that in the presence of DMI, the DW velocity saturates after the Walker field, and that the saturation velocity is proportional to the ratio of the DMI strength and the saturation magnetization (D/Ms). The enhancement of the saturation velocity in systems with reduced Ms is shown by comparing DW dynamics in Pt/Co/GdOx and Pt/Co/Gd stacks. This also means that, knowing Ms , measuring the DW saturation velocity provides an original method to quantify the interfacial Dzyaloshinskii-Moriya interaction, as we show in this work. This method has been used to measure the DMI interaction in Pt/Co/AlOx trilayers in which the top Co interface presents a varying degree of oxidation. We show that besides the strong DMI at the Pt/Co interface, the Co/oxide interface also provides a DMI contribution of the same sign, whose strength depends on the degree of oxidation of the Co/AlOx interface. We also observe that this DMI scales with the perpendicular magnetic anisotropy, which suggest a common origin for the two effects. Finally we have shown preliminary results of field- and current-driven dynamics of DWs in a ferrimagnetic system (GdCo). While close to the compensation composition domain walls in Pt/GdCo/Ta trilayers can be moved to high velocities only by very high magnetic fields, the current driven dynamics is very efficient and depinning currents low. This effect is attributed to the 1/ Ms dependence of the spin-orbit torque acting on the DW magnetization.